Data-driven Control of Nonlinear Dynamics Systems

by

Mehran Rahmani

A Dissertation Presented in Partial Fulfilment
of the Requirements for the Degree
Doctor of Philosophy

Approved June 2023 by the
Graduate Supervisory Committee:

Sangram Redkar, Chair
Thomas Sugar
Susheelkumar C. Subramanian

ARIZONA STATE UNIVERSITY

August 2023

ABSTRACT

This research proposes some new data-driven control methods to control a nonlinear dynamic model. The nonlinear dynamic model linearizes by using the Koopman theory. The Koopman operator is the most important part of designing the Koopman theory. The data mode decomposition (DMD) is used to obtain the Koopman operator. The proposed data-driven control method applies to different nonlinear systems such as microelectromechanical systems (MEMS), Worm robots, and 2 degrees of freedom (2 DoF) robot manipulators to verify the performance of the proposed method. For the MEMS gyroscope, three control methods are applied to the linearized dynamic model by the Koopman theory: linear quadratic regulator (LQR), compound fractional PID sliding mode control, and fractional order PID controller tuned with bat algorithm. For the Worm robot, an LQR controller is proposed to control the linearized dynamic model by the Koopman theory. A new fractional sliding mode control is proposed to control the 2 DoF arm robot. All the proposed controllers applied to the linearized dynamic model by the Kooman theory are compared with some conventional proposed controllers such as PID, sliding mode control, and conventional fractional sliding mode control to verify the performance of the proposed controllers. Simulation results validate their performance in high tracking performance, low tracking error, low frequency, and low maximum overshoot.

DEDICATION

To my beloved mother,

I dedicate this PhD thesis to you with all my heart and soul.

ACKNOWLEDGMENTS

I would like to express my deep gratitude to my advisor, Professor Sangram Redkar, for his unwavering support and guidance throughout my PhD journey. His insights, feedback, and encouragement have been invaluable in shaping my research and helping me to grow as a scholar.

I would also like to thank the members of my thesis committee, Dr. Thomas Sugar and Dr. Susheelkumar Cherangara Subramanian, for their valuable feedback and insights, which have helped to improve the quality of my work.

I am grateful to Arizona State University for providing me with the opportunity to pursue my PhD and for the financial support that has enabled me to focus on my research.

I am also deeply grateful to my family for their unwavering love and support throughout my academic journey. Their encouragement and belief in me have been a constant source of strength.

Thank you all for your support, encouragement, and guidance throughout my PhD journey. Your contributions have been invaluable and have helped me to become the scholar I am today.

I thank Arizona State University and the National Science Foundation for their funding support under Grant No. 1828010.

TABLE OF CONTENTS

Page

LIST OF FIGURES

Figure Page

LIST OF ABBREVIATION

Abbreviation	Definition
DMD	Data Mode Decomposition
MEMS	Microelectromechanical systems
DoF	Degree of Freedom
LQR	Linear Quadratic Regulator
PID	Proportional Integral Derivative
SMC	Sliding Mode Control
FOPID	Fractional Order Proportional Integral Derivative
FOSMC	Fractional Sliding Mode Control
CFOPIDSMC	Compound Fractional Order Order Proportional Integral Derivative Sliding Mode Control
STC	Super Twisting Control
BAFOPID	Bat Fractional Order Proportional Integral Derivative
KFOSMC	Koopman Fractional Sliding Mode Control

1 INTRODUCTION

1.1 Motivation

The Koopman theory is a strong method for data-driven-based control methods. It can linearize the complex nonlinear dynamic model. Several researchers use the Koopman theory in their research to provide better control performance (Goswami & Paley, Bilinearization, reachability, and optimal control of control-affine nonlinear systems: A Koopman spectral approach, 2021) (Shi & Meng, 2022) (Calderón, Schulz, Oehlschlägel, & Werner, (2021, June)) (Husham, Kamwa, Abido, & Suprême, 2022) (Narasingam, Son, & Kwon, 2022). However, the most important part of the Koopman theory application is how to design the Koopman operator.

A useful approach for estimating the modes and eigenvalues of the Koopman operator is the DMD method. Utilizing an embed into infinite dimensional space, the Koopman operator offers a linear description of nonlinear systems. Among the most often used finite dimensional approximations of the Koopman Operator are DMD and Extended DMD (Zanini & Chiuso, 2021; Jiang & Liu, 2022). Koopman operator theory and the associated algorithm DMD were introduced by Ling et al. for the study and control of signalized traffic flow networks. They study DMD's application to various issues in signalized traffic as a model-free method for describing complicated oscillatory dynamics

from observed data (Ling, Zheng, Ratliff, & Coogan, 2020). Wilches-Bernal, Reno, & Hernandez-Alvidrez, (2021) proposes a novel technique for identifying faults and other power quality issues. The major signal indicating a power quality event has occurred is identified by the suggested technique using the real component of the principal eigenvalue computed by the DMD. To discriminate between distinct failures, the study demonstrates how the suggested approach may be utilized to detect events utilizing current and voltage data. The performance of the strategy is examined of the impact of the window size because the suggested method is window-based. To properly control the system, an appropriate controller can be used with the linearized DMD Koopman model such as a linear quadratic regulator controller (LQR) (Mamakoukas, Castano, Tan, & Murphey, (2019, June)) and model predictive controller (MPC) (Ping, Yin, Li, Liu, & Yang, 2021).

1.2 Scope and Overview

This research proposes data-driven control of nonlinear dynamic systems. The data-driven method will provide information on the system that doesn't need to identify the model of the system.

The main contribution of this research is to consider some new control methods based on data-driven methods using the Koopman theory. The novel control methods apply

to different nonlinear dynamic models such as MEMS gyroscope, worm robot, and 2 DoF robot manipulator. The rest of this research is organized as:

Chapter 2 proposes a new compound fractional sliding mode control and super-twisting control of a linear MEMS gyroscope. This chapter considers a new control method to control a linear MEMS gyroscope merely to observe the system's response without including the nonlinearity of the system. A new compound FOSMC and STC is proposed, in which the STC controller will calculate an error value and apply a correction value to the system. Therefore, the proposed compound control method reduces the oscillation, increases tracking performance, and reduces the tracking error.

Chapter 3 introduces the nonlinear dynamic model of the MEMS gyroscope. The DMD method is used to generate eigenfunction and eigenvectors to obtain the Koopman operator. Using the Koopman theory, a FOPID controller is implemented to control the linearized dynamic model. A bat metaheuristic optimization algorithm is used to tune the proposed control method parameters. Finally, the robustness of the proposed control method is verified by random noise application.

Chapter 4 introduces a nonlinear dynamic model of the MEMS gyroscope. The Koopman theory is applied to linearize the nonlinear model of the MEMS gyroscope. The DMD method is used to approximate the Koopman operator. The FOSMC is implemented on the linearized dynamic model to control the MEMS gyroscope. A new compound

control method is applied to improve the control method of the FOSMC such as reducing the control efforts. Simulation results verified the performance of the proposed controller.

Chapter 5 discusses the nonlinear MEMS gyroscope dynamic model. Eigenfunctions were obtained by using the DMD method. Koopman operators are generated by using eigenfunctions obtained from the DMD method. An LQR controller used to control created linear dynamics by Koopman theory. The performance of the proposed method compares with conventional integral sliding mode control, in which the proposed controller has better performance.

Chapter 6 applies an optimal data-driven controller to control a worm robot. The nonlinear dynamics of a worm robot are introduced. The Koopman theory is used to linearize the nonlinear dynamic model of the worm robot. The DMD method is used to generate the Koopman operator. An LQR controller is used to control the linearized dynamic model of the worm robot.

Chapter 7 applies the Koopman theory to linearize the nonlinear dynamics of the 2 DoF robot manipulator. The DMD method is applied to obtain the Koopman operator. Koopman's theory proposes a fractional sliding mode control to control the linearized dynamics model. The conventional PID and FOSMC are implemented to verify the performance of the proposed control method.

2 NEW COMPOUND FRACTIONAL SLIDING MODE CONTROL AND SUPER-TWISTING CONTROL OF A MEMS GYROSCOPE

2.1 Literature review

MEMS gyroscopes are usually used to measure angular velocity, which can be utilized in many applications such as biosystems and control stabilization. However, the MEMS gyroscope performance degrades due to the frequency of oscillation mismatch between two vibrating axes created by external disturbances and time-varying parameters (Yan, Hou, Fang, & Fei, 2017). Therefore, the best performance for the MEMS gyroscope can be obtained by designing an appropriate control method.

Fractional calculus has been widely used for many years (Rahmani, Komijani, Ghanbari, & Ettefagh, 2018). It provides more accurate results for different systems, such as in Robotics and control systems engineering. The fractional-order theory has been applied in various structures because of its ease of modeling dynamics and nonlinear control. FOSMC is a powerful tool in control systems engineering. It is robust against external disturbances and has high tracking performance (Rahmani, Komijani, Ghanbari, & Ettefagh, 2018). Authors (Gao & Liao, 2013)considered the FOSMC to control a hyper chaotic structure (Yang & Liu, 2013). The authors presented integral sliding mode control to enhance the robustness of FOSMC (Gao & Liao, 2013). Balochian (2013) used variable

structure control for an individual polytopic system with a fractional-order operator. A specific feedback law is considered by proposing a sliding surface with a fractional-order operator. Rabah et al. provided a novel technique of FOSMC to guarantee the asymptotic stability of fractional systems (Rabah, Ladaci, & Lashab, 2017). (Shah & Mehta, 2017) described Thiran's delay estimation scheme to compensate the controller for fractional actuator delay, considering the real-time networked medium and packet loss situation. Sun & Ma, (2017), to achieve high convergence precision, applied a fractional integral sliding mode control for tracking control of the linear motor. Experimental results validated that the proposed control law has high tracking performance compared to conventional sliding mode control. Wang, Gu, Xu, & Cao, (2016) proposed a new fractional-order nonsingular terminal sliding mode control. Due to the fractional-order nonsingular terminal sliding mode control and fast terminal sliding mode controller, the proposed controller guarantees fast convergence and high tracking performance. Aghababa, (2014) presented a new fractional hierarchical terminal sliding mode surface, in which its finite-time convergence to the origin is demonstrated. A robust sliding mode switching control method is proposed to guarantee the fractional Lyapunov stability theory and sliding mode control technique in reference. Wang, Mustafa, & Tian, (2018) implemented a novel sliding mode controller for an active vehicle suspension system to suppress external noise that acts on that system. Based on previous research, FOSMC can be used as a robust control method in different

systems (Kaur & Narayan, 2018) (Khan & Tyagi, 2017) (Ardjal, Mansouri, & Bettayeb, 2018), but its main drawback is creating a chattering phenomenon.

STC is a technique that can be used in control systems. It overcomes disturbances of super-twisting control (Guruganesh, Bandyopadhyay, Arya, & Singh, 2018). Jeong, Kim, & Han, (2018) designed a robust super-twisting sliding mode control that guarantees a high tracking trajectory of a robotic system. To satisfy the properties of a conventional sliding mode control, a super-twisting sliding mode surface is designed for obtaining the transient and steady-state time performances of the position of the robotic manipulator. Chuei, Cao, & Man, (2017) described a super-twisting observer-based repetitive control, which overcomes aperiodic disturbances. Zargham & Mazinan, (2018) applied a super-twisting sliding mode control to control the wind turbine system. However, conventional sliding mode control cannot guarantee closed-loop performance against external perturbations; due to this drawback, an STC technique is used for rapid response and high accuracy in chattering reduction. Zhao, Gu, Zhang, & Ding, (2017) proposed a nonsingular terminal sliding mode control based on the STC method to eliminate the chattering phenomenon and avoid the singularity problem. Lu & Xia, (2014) addressed a new adaptive super-twisting algorithm for controlling rigid spacecraft. The applied controller is anti-singularity and anti-chattering when encountered with external disturbances. Evangelista, Puleston, Valenciaga, & Fridman, (2012) used modified STC, which

improves the system's robustness in external perturbations acting on a wind turbine shaft. Becerra, Hayet, & Sagüés, (2014) proposed an STC which guarantees continuous control inputs and enhances robustness properties. Salgado, Kamal, Bandyopadhyay, Chairez, & Fridman, (2016) introduced a discrete-time super-twisting algorithm to solve the problems of control and state estimation. As a result of considered studies, STC can be a vital tool in control systems. It has some advantages, such as improving the robustness of control systems, removing controller singularity, and eliminating the chattering phenomenon.

The contribution of this method are as follows:

1- Propose a new fractional sliding mode surface for use in the FOSMC to suppress the external perturbations.

2- A new compound FOSMC and STC is proposed, in which the STC controller will calculate an error value and apply a correction value to the system. Therefore, the proposed compound control method reduces the oscillation, increases tracking performance, and reduces the tracking error.

2.2 Linear dynamic of MEMS gyroscope

A z-axis MEMS gyroscope is shown in Figure 2.1. The conventional MEMS vibratory gyroscope consists of a proof mass (m) suspended by springs, where *x* and *y* are the coordinates of the proof mass with respect to the gyro frame in a cartesian coordinate

system, sensing mechanisms, and an electrostatic actuation for forcing an oscillatory motion and velocity of the proof mass and sensing the position. $\Omega_{x,y,z}$ are the angular rate components along each axis of the gyro frame.

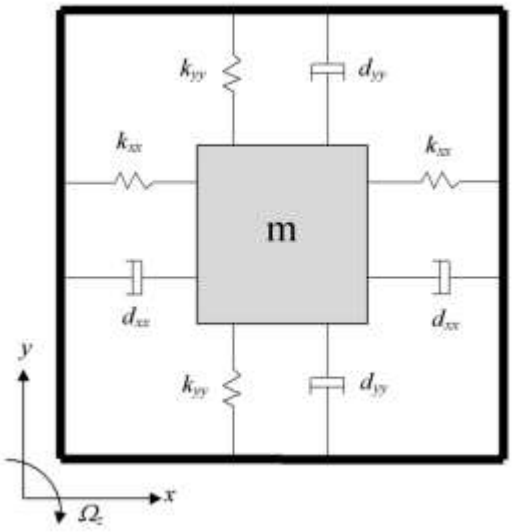

Figure 2.1: Structure of MEMS gyroscope.

The frame where the proof mass is mounted moves with a constant velocity, and the gyroscope rotates at a slowly changing angular velocity of Ω_z. The centrifugal forces $m\Omega_z^2 x$ and, $m\Omega_z^2 y$ are assumed to be negligible because of small displacements. The Coriolis force is generated perpendicular to the drive and rotational axes (Rahmani M. , 2018).

The dynamics equations of the gyroscope are given by

$$m\ddot{x} + d_{xx}^{*}\dot{x} + d_{xy}^{*}\dot{y} + k_{xx}^{*}x + k_{xy}^{*}y = u_{x}^{*} + 2m\Omega_{z}^{*}\dot{y} \quad (2.1)$$

$$m\ddot{y} + d_{xy}^{*}\dot{y} + d_{yy}^{*}\dot{y} + k_{xy}^{*}x + k_{yy}^{*}y = u_{y}^{*} - 2m\Omega_{z}^{*}\dot{x} \quad (2.2)$$

The origin for the x and y coordinates is at the center of the proof mass without force employed. Fabrication imperfections will affect the asymmetric spring and damping terms, k_{xy}^{*} and d_{xy}^{*} Respectively. The stiffness and damping terms are given by $k_{xx}^{*}, k_{yy}^{*}, d_{xx}^{*}$ and d_{yy}^{*} .

The stiffness and damping terms may vary slightly from nominal values (Rahmani M. , 2018; Yan, Hou, Fang, & Fei, 2017). However, the magnitude of the proof mass *m* can be obtained precisely.

The u_{x}^{*} and u_{y}^{*} are the control forces in the *x* and *y*-direction. Dividing gyroscope dynamics (1) and (2) by the reference mass results in the following vector forms:

$$\ddot{q}^{*} + \frac{D^{*}}{m}\dot{q}^{*} + \frac{K_{a}}{m}q^{*} = \frac{u^{*}}{m} - 2\Omega^{*}\dot{q}^{*} \quad (2.3)$$

Where

$$q^{*} = \begin{bmatrix} x^{*} \\ y^{*} \end{bmatrix}, \quad u = \begin{bmatrix} u_{x}^{*} \\ u_{y}^{*} \end{bmatrix}, \quad \Omega * = \begin{bmatrix} 0 & -\Omega_{z}^{*} \\ \Omega_{z}^{*} & 0 \end{bmatrix}$$

$$D^{*} = \begin{bmatrix} d_{xx}^{*} & d_{xy}^{*} \\ d_{xy}^{*} & d_{yy}^{*} \end{bmatrix}, \quad K_{a} = \begin{bmatrix} k_{xx}^{*} & k_{xy}^{*} \\ k_{xy}^{*} & k_{yy}^{*} \end{bmatrix}$$

The final form of the non-dimensional equation of motion is as follows:

$$\frac{\ddot{q}^*}{q_0} + \frac{D^*}{m\omega_0}\frac{\dot{q}^*}{q_0} + \frac{K_a}{m\omega_0^2}\frac{q^*}{q_0} = \frac{u^*}{m\omega_0^2 q_0} - 2\frac{\Omega^*}{\omega_0}\frac{\dot{q}^*}{q_0} \tag{2.4}$$

We determine a set of new parameters as follows:

$$q = \frac{q^*}{q_0}, \quad d_{xy} = \frac{d_{xy}^*}{m\omega_0}, \quad \Omega_z = \frac{\Omega_z^*}{\omega_0} \tag{2.5}$$

$$u = \frac{u_x^*}{m\omega_0^2 q_0}, \quad u_y = \frac{u_y^*}{m\omega_0^2 q_0} \tag{2.6}$$

$$\omega_x = \sqrt{\frac{k_{xx}}{m\omega_0^2}}, \quad \omega_y = \sqrt{\frac{k_{yy}}{m\omega_0^2}}, \quad \omega_{xy} = \frac{k_{xy}}{m\omega_0^2} \tag{2.7}$$

$$\ddot{q} + D\dot{q} + K_b q = u - 2\Omega\dot{q} \tag{2.8}$$

Where

$$q = \begin{bmatrix} x \\ y \end{bmatrix}, \quad u = \begin{bmatrix} u_x \\ u_y \end{bmatrix}, \quad \Omega = \begin{bmatrix} 0 & -\Omega_z \\ \Omega_z & 0 \end{bmatrix}$$

$$D = \begin{bmatrix} d_{xx} & d_{xy} \\ d_{xy} & d_{yy} \end{bmatrix}, \quad K_b = \begin{bmatrix} \omega_x^2 & \omega_{xy} \\ \omega_{xy} & \omega_y^2 \end{bmatrix}$$

Equation (2.8) can be rearranged as:

$$\ddot{q} = -(D + 2\Omega)\dot{q} - K_b q + u + E \tag{2.9}$$

where E is an external disturbance. Since the disturbance is considered unknown, the model from equation (2.9) used to generate the control signal must be modified by setting E=0:

$$\ddot{q} = -M\dot{q} - Nq + u \tag{2.10}$$

where M=(D+2Ω) and N=K_b.

2.3 New fractional sliding mode control

Selecting a fractional sliding mode surface is the central part of FOSMC design. The fractional derivative and integral order in the sliding mode surface provides the flexibility of having the fractional type of error in controller design. The best performance will be obtained if a fractional sliding mode surface is chosen correctly. The fractional sliding mode surface can be selected as follows:

$$s(t) = \dot{e}(t) + \alpha D^{\mu-1}e(t) + \beta D^{\mu-2}e(t) + \gamma \int_0^t e(\tau)^{\frac{r}{m}} d\tau \tag{2.11}$$

where *r*, *m*, α, β, and γ are positive constants, and *D* is a fractional-order operator (*D=d/dt*, and μ>2). The fractional-order operator type is Grunwald-Letnikov. The tracking error can be shown as:

$$e(t) = q - q_d \tag{2.12}$$

The derivative of the fractional sliding mode surface is

$$\dot{s}(t) = \ddot{e}(t) + \alpha D^{\mu} e(t) + \beta D^{\mu-1} e(t) + \gamma e(t)^{\frac{r}{m}} \tag{2.13}$$

$$= \ddot{q} - \ddot{q}_d + \alpha D^{\mu} e(t) + \beta D^{\mu-1} e(t) + \gamma e(t)^{\frac{r}{m}}$$

$$= -M\dot{q} - Nq + u - \ddot{q}_d + \alpha D^{\mu} e(t) + \beta D^{\mu-1} e(t)$$

$$+ \gamma e(t)^{\frac{r}{m}}$$

Equivalent control u_{eq} can be obtained by setting $\dot{s}(t) = 0$.

$$u_{eq}(t) = M\dot{q} + Nq + \ddot{q}_d - \alpha D^{\mu} e(t) - \beta D^{\mu-1} e(t) - \gamma e(t)^{\frac{r}{m}} \tag{2.14}$$

The FOSMC can be shown as:

$$u_{FOSMC}(t) = u_{eq}(t) + u_s(t) \tag{2.15}$$

$$= M\dot{q} + Nq + \ddot{q}_d - \alpha D^{\mu} e(t) - \beta D^{\mu-1} e(t) - \gamma e(t)^{\frac{r}{m}}$$

$$- K_s s$$

The equivalent control cannot compensate for external perturbation and unmodelled dynamic uncertainties. A reaching control law can be designed to remove those problems as $u_s(t)$, which can be defined as:

$$u_s(t) = -K_s sign(s) \tag{2.16}$$

where K_s is a positive constant.

Consider the following Lyapunov function candidate (V), continuous and nonnegative (Rahmani, Ghanbari, & Ettefagh, 2016; Devanshu, Singh, & Kumar, 2020; Rahmani, Ghanbari, & Ettefagh, 2018).

$$V = \frac{1}{2} s^T s \tag{2.17}$$

The time derivative of *V* yields:

$$\dot{V} = s^T \dot{s} = s^T(-M\dot{q} - Nq + u(t) - \ddot{q}_d + \alpha D^{\mu} e(t) + \beta D^{\mu-1} e(t) + \gamma e(t)^{\frac{r}{m}}) \tag{2.18}$$

Substituting equation (2.15) into equation (2.18), generates

$$\dot{V} = s^T \dot{s} = s^T(-M\dot{q} - Nq + M\dot{q} + Nq + \ddot{q}_d - \alpha D^{\mu} e(t) - \beta D^{\mu-1} e(t) - \gamma e(t)^{\frac{r}{m}} \tag{2.19}$$

Simplifying equation (2.19) results in

$$\dot{V} = s^T(-K_s sign(s)) \tag{2.20}$$

Therefore, equation (2.20) can be expressed as

$$\dot{V} = -K_s s^T sign(s) \tag{2.21}$$

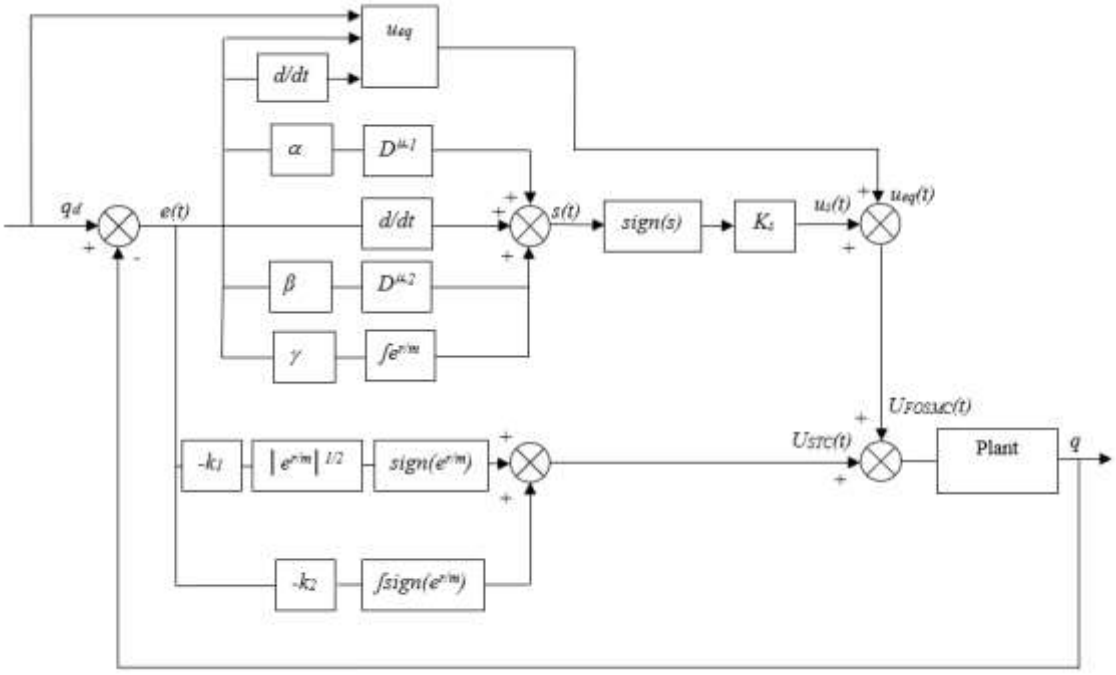

Figure 2.2: Block diagram of the novel control system.

Equation (2.21) shows that $\dot{V} < 0$, which expresses that the proposed control law is stable.

2.4 New compound fractional sliding mode control and super-twisting control

FOSMC is one of the techniques that can enhance the robustness of the control system and improve tracking performance. As discussed before, its main drawback is

creating a chattering phenomenon. However, STC can be used in conjunction with FOSMC to minimize the chattering of the system, improve trajectory tracking, and remove singularity problems. By combining both FOSMC and STC, a better control method will be obtained, combining both controllers' benefits. The Block diagram of the proposed controller is illustrated in Figure 2.2. The compound control law can be defined as:

$$u(t) = u_{FOSMC}(t) + u_{STC}(t) \tag{2.22}$$

where $u_{STC}(t)$ is

$$u_{STC}(t) = -k_1 \left| e^{\frac{r}{m}} \right|^{\frac{1}{2}} sign(e^{\frac{r}{m}}) - k_2 \int_0^t sign(e^{\frac{r}{m}}) d\tau \tag{2.23}$$

where k_1, k_2, r, and m are positive constants.

The stability proving of the proposed control law can be arranged by substituting Equation (2.22) into equation (2.18) as:

$$\dot{V} = s^T \dot{s} = s^T(-M\dot{q} - Nq + u_{FOSMC}(t) + u_{STC}(t) + E - \ddot{q}_d \tag{2.24}$$
$$+ \alpha D^{\mu} e(t) + \beta D^{\mu-1} e(t) + \gamma e(t)^{\frac{r}{m}})$$

$$\dot{V} = s^T \dot{s} = s^T(-M\dot{q} - Nq + M\dot{q} + Nq - E + \ddot{q}_d - \alpha D^{\mu} e(t) \tag{2.25}$$
$$- \beta D^{\mu-1} e(t)$$

$$+E - \ddot{q}_d + \alpha D^{\mu} e(t) + \beta D^{\mu-1} e(t + \gamma e(t)^{\frac{r}{m}})$$

Simplifying equation (2.25) generates

$$\dot{V} = s^T(-K_s sign(s) - k_1 \left| e^{\frac{r}{m}} \right|^{\frac{1}{2}} sign(e^{\frac{r}{m}}) - k_2 \int_0^t sign(e^{\frac{r}{m}}) d\tau) \tag{2.26}$$

The stability of FOSMC was proved in section 2. 3. Therefore, the main controller is stable. Also, the error was reduced by using the compound controller. This shows that the proposed controller will improve the system's stability. Therefore, equation (2.26) can be written as:

$$\dot{V} = -K_s s^T sign(s) \tag{2.27}$$

where K_s is positive, which leads to $\dot{V} < 0$.

2.5 Simulation results

The most important part of the controller design procedure is the selection of proposed controller parameters (α, β, (, Ks, μ, r, m, k1, and k2). If parameters are chosen inappropriately, the proposed control method cannot guarantee the desired performance, such as trajectory tracking, robustness, stability, and chattering elimination. The controller parameters are chosen based on the designer's experiences and the trial-error process. Simulation results have shown that the parameters are selected appropriately. Parameters of the fractional-order sliding mode surface are selected as *α=diag(40,40), β=diag(50,50)*,

γ=*diag(60,60),* K_s=*diag(10,10),* μ=*2.5*, *r=1.5* and *m=1.25*. The STC parameters are chosen as k_1=*diag(20,20)* and k_2=*diag(20,20)* .The desired motion trajectory is determined by q_{d1}=*sin (4.17t)* and q_{d2}=*1.2sin(5.11t)*. The initial values of the system are selected as:

$$q_1(0) = 0.5,\ q_2(0) = 0.5,\ \dot{q}_1(0) = 0\ and\ \dot{q}_2(0) = 0$$

The parameters of the MEMS gyroscope are selected as:

$$m = 1.8 \times 10^{-7} kg \qquad k_{xy} = 12.779 N/m$$

$$k_{xx} = 63.955 N/m \qquad d_{xx} = 1.8 \times 10^{-6} Ns/m$$

$$k_{yy} 95.92 N/m \qquad d_{yy} 1.8 \times 10^{-6} Ns/m$$

$$d_{xy} = 3.6 \times 10^{-7} Ns/m$$

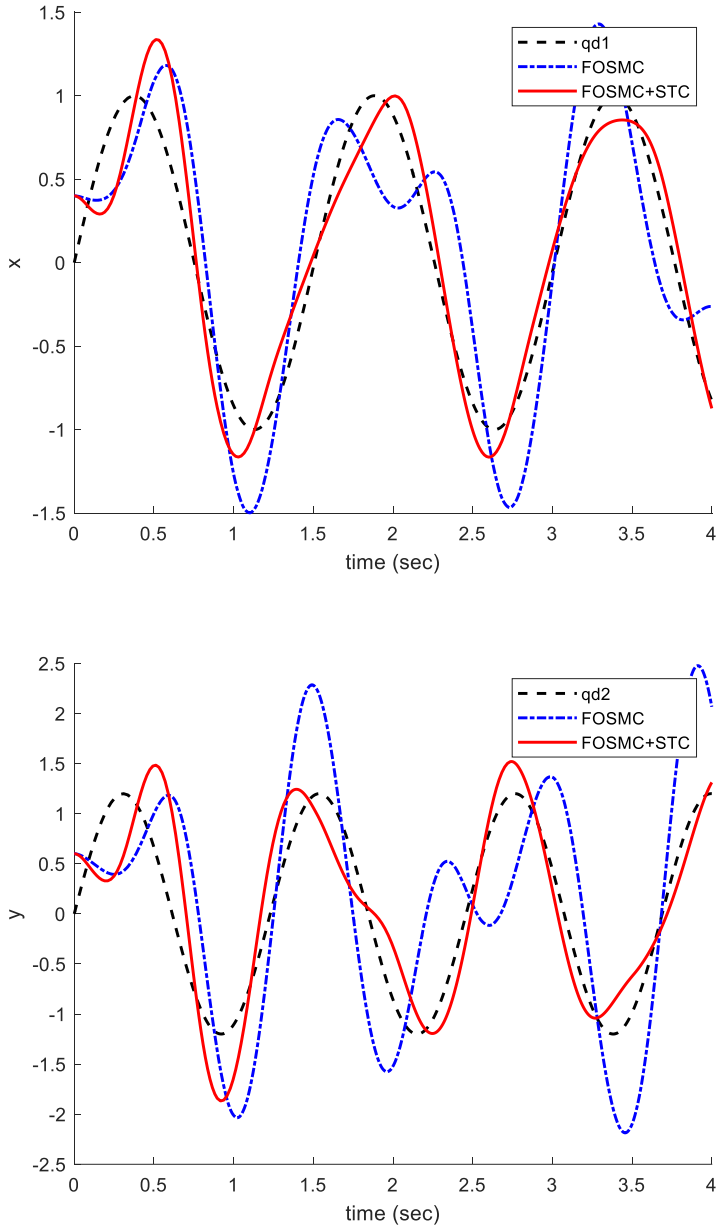

Figure 2.3: Position tracking of x-axis and y-axis.

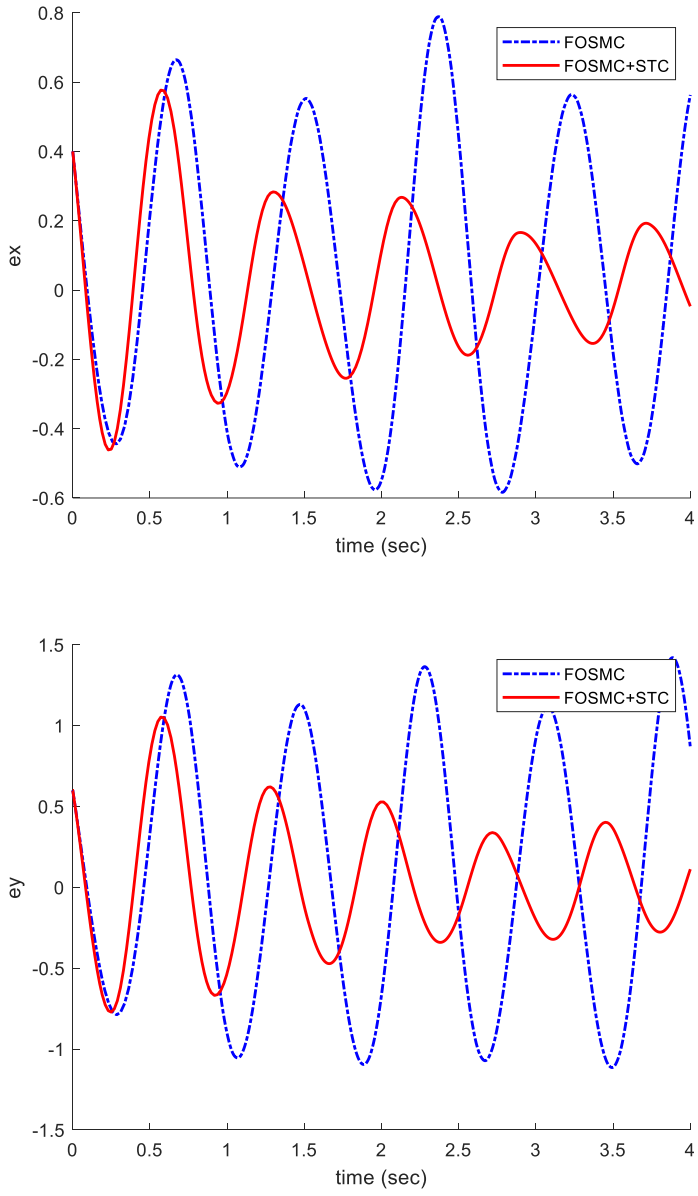

Figure 2.4: Position tracking error of x-axis and y-axis.

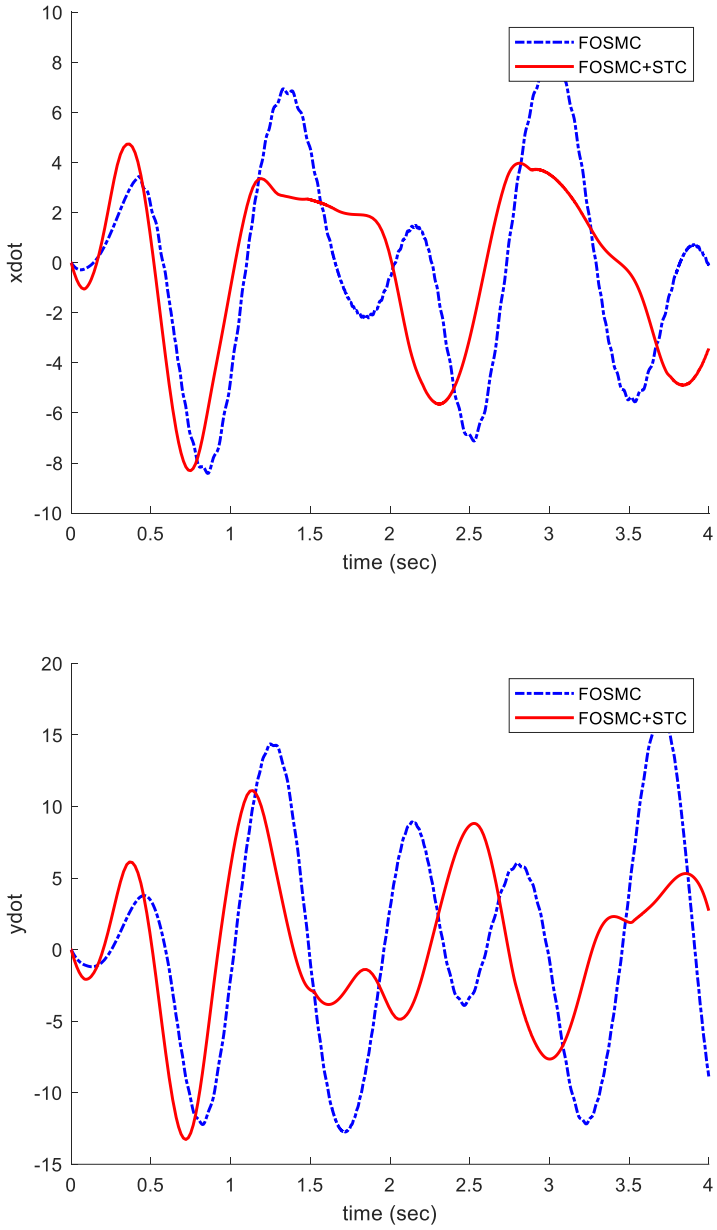

Figure 2.5: Velocity of x-axis and y-axis.

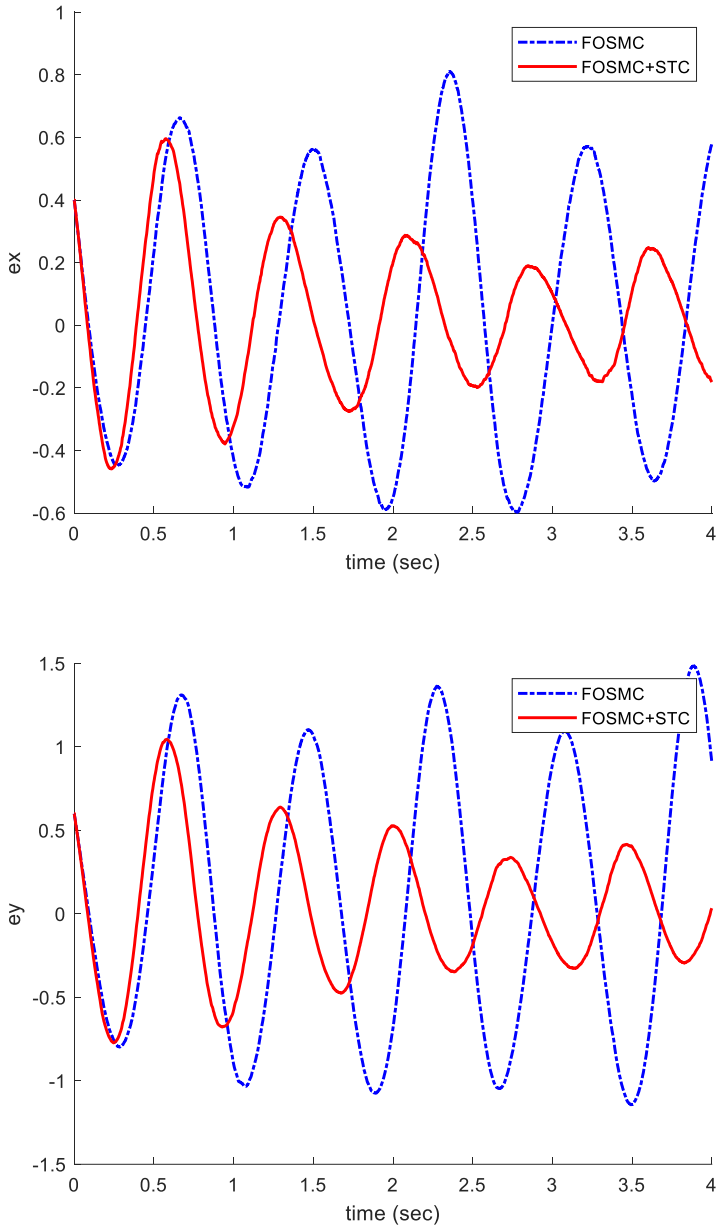

Figure 2.6: Tracking error under random noise.

Typically, the natural frequency of each axis of a MEMS gyroscope is in the kHz range. Thus, ω_0 is selected as *1kHz*. It is suitable to choose $1\mu m$ as the reference length q_0 when the displacement range of the MEMS gyroscope in each axis is sub-micrometer level. The unknown angular velocity is assumed Ω_z*=100 rad/s*. Therefore, the non-dimensional values of the MEMS gyroscope parameters are chosen as:

$$\omega_x^2 = 355.3,\ \omega_y^2 = 532.9,\ \omega_{xy} = 70.99,\ d_{xx} = 0.01,\ d_{yy} = 0.01,\ d_{xy} = 0.002,\ \Omega_z = 0.1$$

Figure 2.3 shows position tracking of the x-axis and y-axis under FOSMC and FOSMC+STC. It can be seen clearly that tracking performance under the proposed controllers is consistent with the desired tracking of the MEMS gyroscope. Figure 2.4 illustrates the tracking error of the x-axis and y-axis under FOSMC and the proposed control. FOSMC creates a chattering phenomenon, which by using STC, is reduced. In addition, FOSMC+STC has a lower maximum overshoot and undershoot than FOSMC. Figure 2.5 shows the velocity of the x-axis and y-axis under FOSMC and the proposed control law. The robustness of the proposed control method was verified by applying the random noise as 0.5*randn(1,1). Figure 2.6 shows that the proposed control method is robust against external disturbances.

2.6 Conclusion

This method proposed a novel FOSMC+STC law to control a MEMS gyroscope. First, a new FOSMC is applied to control the x-axis and y-axis of a MEMS gyroscope. It has high tracking performance, but its main drawback was creating a chattering phenomenon. To solve this problem, an STC is proposed in parallel with FOSMC, which continuously calculates an error value and applies a correction value. Simulated results demonstrate that the developed STC significantly reduces the chattering phenomenon. In addition, using STC, maximum overshoot and undershoot are reduced, and trajectory tracking performance improves. Simulation results thus validated the effectiveness of the proposed control strategy.

3 DATA DRIVEN KOOPMAN FRACTIONAL ORDER PID CONTROL OF A MEMS GYROSCOPE USING BAT ALGORITHM

3.1 Literature review

The MEMS gyroscope is an interesting device that can measure angular velocity by motion in the x and y directions. This tool has been used in the automotive industry due to its low costs and small size (Solouk, Shojaeefard, & Dahmardeh, 2019; Classen, Frey, Kuhlmann, Ernst, & Bosch, 2007). The control of the MEMS gyroscope is a difficult task because it constantly encounters external disturbances, and designing a suitable control method is required for this system (Zhang & Lin, 2010).

An interesting area of study is data-driven control systems, which uses data to control dynamic systems (Gao, Liu, Wang, & Wang, 2022; Xian, Gu, & Pan, 2022; Liu, Cheng, Xiao, & Hao, 2022). Several techniques are used to create data-driven structures such as deep neural networks (Sun, Dominguez-Caballero, Ward, Ayvar-Soberanis, & Curtis, 2022) and machine learning algorithms (Chen & You, 2021). One effective method for linearizing the nonlinear dynamic model is the linear parameter varying (LPV) method. Hadian, Ramezani, & Zhang, (2022) proposed a controller to reduce computation and conservatism for constrained nonlinear MIMO systems. Also, the simulation results verified the effectiveness of the proposed method in terms of disturbance rejection and high

tracking performance. In addition, a model predictive controller (MPC) is proposed for nonlinear systems subjected to perturbations (Hadian, Ramezani, & Zhang, Robust Model Predictive Controller Using Recurrent Neural Networks for Input–Output Linear Parameter Varying Systems, 2021). The LPV method is used to linearize the nonlinear dynamic model. Then, the MPC controller is applied to the linearized model. The proposed method is robust against disturbances. In data driven-control systems, Koopman's theory is a strong approach. By projecting the system dynamics onto the Koopman eigenspace, Goswami and Paley (Goswami & Paley, Bilinearization, reachability, and optimal control of control-affine nonlinear systems: A Koopman spectral approach., 2021) explore the issues of bilinearization and optimum control of a control-affine nonlinear system. Under certain assumptions, the suggested technique converts the dynamics into a bilinear system by using the Koopman canonical transform, especially the Koopman eigenfunctions of the drift vector field. Numerous examples of control-affine nonlinear systems are used to numerically demonstrate bilinearization and the best control strategy while assuming a quadratic cost function for the states and control input. The difficulties of making models that are subject to model-based control design methodologies make it challenging to operate soft robots precisely. Koopman operator theory provides a framework for creating explicit dynamical models of soft robotics and controlling them with practiced model-based techniques (Bruder, Fu, Gillespie, Remy, & Vasudevan, 2020). How to derive the

Koopman operator is the most crucial aspect of the Koopman theory, especially for complex systems with a nonlinear dynamic systems.

A useful approach for estimating the modes and eigenvalues of the Koopman operator is the DMD method. Utilizing an embedding into infinite dimensional space, the Koopman operator offers a linear description of nonlinear systems. Among the most often used finite dimensional approximations of the Koopman Operator are DMD and Extended DMD (Zanini & Chiuso, 2021; Jiang & Liu, 2022). Koopman operator theory and the associated algorithm DMD were introduced by Ling et al. for the study and control of signalized traffic flow networks. They study DMD's application to various issues in signalized traffic as a model-free method for describing complicated oscillatory dynamics from observed data (Ling, Zheng, Ratliff, & Coogan, 2020). Wilches-Bernal, Reno, & Hernandez-Alvidrez, (2021) proposes a novel technique for identifying faults and other power quality issues. The major signal indicating a power quality event has occurred is identified by the suggested technique using the real component of the principal eigenvalue computed by the DMD. To discriminate between distinct failures, the study demonstrates how the suggested approach may be utilized to detect events utilizing current and voltage data. The performance of the strategy is examined in relation to the impact of the window size because the suggested method is window-based. To properly control the system, an appropriate controller can be used with the linearized DMD Koopman model such as a

linear quadratic regulator controller (LQR) (Mamakoukas, Castano, Tan, & Murphey, (2019, June)) and model predictive controller (MPC) (Ping, Yin, Li, Liu, & Yang, 2021).

PID controller is a strong control method to control linear dynamic systems. It has been widely used in real-world systems due to its low cost and ease of implementation (Rahmani, Ghanbari, & Ettefagh, Robust adaptive control of a bio-inspired robot manipulator using bat algorithm, 2016; Rahmani, Komijani, Ghanbari, & Ettefagh, 2018). By regulating the PID gains, it constantly evaluates errors and provides the best value. It is used to control different systems such as MEMS gyroscopes (Fei & Chu, Dynamic global PID sliding mode control for MEMS gyroscope using adaptive neural controller, (2016, August)), vehicle (Marino, Scalzi, & Netto, 2011), and quadcopter (Yoon & Doh, 2022). However, the main drawbacks of the PID control method are that it’s not robust control against external disturbances. Although some useful methods can be used to tune the PID controller parameters such as Axiomatic-Design-Theory-Based (Li, Chen, & Zhang, 2010), the fractional control is also a suitable controller to improve the robustness and stability of the PID controller. The FOPID controller has been used in different research. Large uncertainty in dynamic and hydrodynamic properties as well as the signal transmission channel's time delay are the key challenges with autonomous underwater vehicles (AUV) motion control. For an AUV yaw control system, Liu, Zhang, Pan, & Zhang (2022) suggest a reliable FOPID controller architecture. Erol (2021) proposed a

strong method for the pitch control system of large wind turbines with a FOPID controller that is delay-dependent. The simulation findings demonstrate that outcomes for the delay margin are improved by using the proposed method. One of the main parts of FOPID controller design is how to tune the controller's gains to achieve the best performance. The bat optimization algorithm is a suitable method to tune the proposed controller's parameters.

The bat algorithm is inspired by the echolocation behavior of microbats, with varying pulse rates of emission and loudness (Yang X. S., A new metaheuristic bat-inspired algorithm, 2010). Finding solutions using algorithms based on population and local search is a benefit of employing the bat algorithm. We get both local rigorous exploitation and global variety from this combination, which is crucial for metaheuristic algorithms. The advantages of the bat algorithm in comparison with particle swarm optimization and genetic algorithms are discussed in (Perwaiz, Younas, & Anwar, 2020). Based on the Equivalent Transfer Function model and a reduced decoupler, (Lakshmanaprabu, Elhoseny, & Shankar, 2019) describes a technique for developing independent FOPID controllers for two interacting conical tank-level processes. An optimization bat algorithm is used to increase the power system stability by tuning FOPID controller parameters (Chaib, Choucha, & Arif, 2017).

This method proposes a new data-driven control algorithm to control the MEMS gyroscope. The contribution of this work is as follows:

1- The nonlinear dynamic model of the MEMS gyroscope is presented.

2- DMD method is used to generate eigenfunction and eigenvectors to obtain the Koopman operator.

3- Using the Koopman theory, a FOPID controller is implemented to control the linearized dynamic model.

4- A bat metaheuristic optimization algorithm is used to tune the proposed control method parameters.

5- The robustness of the proposed control method is verified by random noise application.

3.2 Nonlinear dynamic model of MEMS gyroscope

An essential instrument for angular velocity measurement using x and y motion is the MEMS gyroscope (Fang, Fu, Ding, & Fei, 2022; Lu & Fei, (2016, June); Guo, Xu, & Zhang, 2020). This device has been used in the automotive industry.

A common MEMS gyroscope design includes sensor mechanisms, a proof mass suspended by springs, and an electrostatic actuation system for generating an oscillatory motion and determining the position and speed of the proof mass (Rahmani, Rahman, &

Nosonovsky, A new hybrid robust control of MEMS gyroscope, 2020). The proof mass is mounted on a frame that moves with a consistent linear velocity, while the gyroscope rotates at a gradually varying angular velocity, Ω_z. The centrifugal forces $m\Omega_z^2 x$ and $m\Omega_z^2 y$ are expected to be insignificant due to the modest displacements x and y. The development of the Coriolis forces, $2m\Omega_z^* \dot{y}$ and $2m\Omega_z^* \dot{x}$, is parallel to the driving and rotating axes (Yan, Hou, Fang, & Fei, 2017). The dynamics of the gyroscope are determined by the following equations.

$$m\ddot{x} + d_{xx}^* \dot{x} + d_{xy}^* \dot{y} + k_{xx}^* x + k_{xy}^* y + \beta x^3 = u_x^* + 2m\Omega_z^* \dot{y} \quad (3.1)$$

$$m\ddot{y} + d_{xy}^* \dot{y} + d_{yy}^* \dot{y} + k_{xy}^* x + k_{yy}^* y + \beta y^3 = u_y^* - 2m\Omega_z^* \dot{x} \quad (3.2)$$

The origin of the coordinates in equations (3.1) and (3.2) is placed in the center of the proof mass since there is no external force applied to the system. The constants k_{xy}^* and d_{xy}^*, respectively, stand in for the asymmetric spring and damping coefficients. Despite the possibility of small unknown deviations from their nominal values, the control forces in the x- and y-direction, u_x^* and u_y^*, are usually accepted. There are also typical descriptions of the damping rates, d_{xx}^* and d_{yy}^*, and the spring constants of springs interacting in the x- and y-directions, $k_{xx}^*$and k_{yy}^*. Therefore, both electro-mechanical and mechanical

nonlinearity, which is a positive constant, will introduce the terms βx^3 and βy^3. The following vector representation might be used to express equations (3.1) and (3.2):

$$\frac{\ddot{q}^*}{q_0} + \frac{D^*}{m\omega_0}\frac{\dot{q}^*}{q_0} + \frac{K_a}{m\omega_0^2}\frac{q^*}{q_0} + \beta\frac{{q^*}^3}{q_0} = \frac{u^*}{m\omega_0^2 q_0} - 2\frac{\Omega^*}{\omega_0}\frac{\dot{q}^*}{q_0} \tag{3.3}$$

where

$q^* = \begin{bmatrix} x^* \\ y^* \end{bmatrix}, u = \begin{bmatrix} u_x^* \\ u_y^* \end{bmatrix}, \Omega^* = \begin{bmatrix} 0 & -\Omega_z^* \\ \Omega_z^* & 0 \end{bmatrix}, D^* = \begin{bmatrix} d_{xx}^* & d_{xy}^* \\ d_{xy}^* & d_{yy}^* \end{bmatrix}, K_a = \begin{bmatrix} k_{xx}^* & k_{xy}^* \\ k_{xy}^* & k_{yy}^* \end{bmatrix}$, and nondimensional parameters as follows:

$$q = \frac{q^*}{q_0} \qquad d_{xy} = \frac{d_{xy}^*}{m\omega_0} \qquad \Omega_z = \frac{\Omega_z^*}{\omega_0} \tag{3.4}$$

$$u_x = \frac{u_x^*}{m\omega_0^2 q_0} \qquad u_y = \frac{u_y^*}{m\omega_0^2 q_0} \tag{3.5}$$

$$\omega_x = \sqrt{\frac{k_{xx}}{m\omega_0^2}} \qquad \omega_y = \sqrt{\frac{k_{yy}}{m\omega_0^2}} \qquad \omega_{xy} = \frac{k_{xy}}{m\omega_0^2} \tag{3.6}$$

where each axis' natural frequency is ω_0 and the reference length is q_0.

The following are the dynamic equations for the MEMS gyroscope.

$$\ddot{q} = -(D + 2\Omega)\dot{q} - K_b q - \beta q^3 + u + E \tag{3.7}$$

An external disturbance, *E*, might be modeled as:

$$\ddot{q} = -Y\dot{q} - Pq - \beta q^3 + u + E \tag{3.8}$$

where Y and P determine certain parameter variation uncertainties $P = K_b$, , and $Y = (D + 2\Omega)$. Therefore, equation (8.3) might be expressed as:

$$\ddot{q} = -(Y + \Delta Y)\dot{q} - (P + \Delta P)q - \beta q^3 + u + E \tag{3.9}$$

where

$$q = \begin{bmatrix} x \\ y \end{bmatrix}, u = \begin{bmatrix} u_x \\ u_y \end{bmatrix}, \Omega = \begin{bmatrix} 0 & -\Omega_z \\ \Omega_z & 0 \end{bmatrix}, D = \begin{bmatrix} d_{xx} & d_{xy} \\ d_{xy} & d_{yy} \end{bmatrix}, K_b = \begin{bmatrix} \omega_x^2 & \omega_{xy} \\ \omega_{xy} & \omega_y^2 \end{bmatrix}$$

There are several ways to show the equation (3.9):

$$\ddot{q} = -Y\dot{q} - Pq - \beta q^3 + u(t) + D(t) \tag{3.10}$$

D(t) describes as:

$$D(t) = -\Delta Y\dot{q} - \Delta Pq + E \tag{3.11}$$

The expression for equation (3.10) in the x and y directions is

$$\begin{bmatrix} \ddot{x} \\ \ddot{y} \end{bmatrix} = -\left(\begin{bmatrix} \boldsymbol{d_{xx}} & \boldsymbol{d_{xy}} \\ \boldsymbol{d_{xy}} & \boldsymbol{d_{yy}} \end{bmatrix} + \begin{bmatrix} \mathbf{0} & \boldsymbol{-2\Omega_z} \\ \boldsymbol{2\Omega_z} & \mathbf{0} \end{bmatrix}\right)\begin{bmatrix} \dot{x} \\ \dot{y} \end{bmatrix} - \tag{3.12}$$

$$\begin{bmatrix} \boldsymbol{\omega_x^2} & \boldsymbol{\omega_{xy}} \\ \boldsymbol{\omega_{xy}} & \boldsymbol{\omega_y^2} \end{bmatrix}\begin{bmatrix} \boldsymbol{x} \\ \boldsymbol{y} \end{bmatrix} - \begin{bmatrix} \boldsymbol{\beta} & \mathbf{0} \\ \mathbf{0} & \boldsymbol{\beta} \end{bmatrix}\begin{bmatrix} \boldsymbol{x^3} \\ \boldsymbol{y^3} \end{bmatrix} + \begin{bmatrix} \mathbf{1} & \mathbf{0} \\ \mathbf{0} & \mathbf{1} \end{bmatrix}\begin{bmatrix} \boldsymbol{u_x} \\ \boldsymbol{u_y} \end{bmatrix} + \quad + \begin{bmatrix} \boldsymbol{D(t)_x} \\ \boldsymbol{D(t)_y} \end{bmatrix}$$

Equation (3.12) will be transformed into first-order dynamic equations by selecting the following parameters:

$$\begin{cases} \boldsymbol{x = z_1} \\ \boldsymbol{\dot{x} = z_2} \\ \boldsymbol{y = z_3} \\ \boldsymbol{\dot{y} = z_4} \end{cases}$$

Then, there is

$$\begin{cases} \boldsymbol{\dot{z}_1 = z_2} \\ \boldsymbol{\dot{z}_2 = -\omega_x^2 z_1 - \beta z_1^3 - d_{xx} z_2 - \omega_{xy} z_3 + (2\Omega_z - d_{xy}) z_4 + u_{z_1} + D_{z_1}} \\ \boldsymbol{\dot{z}_3 = z_4} \\ \boldsymbol{\dot{z}_4 = -\omega_{xy} z_1 - (d_{xy} + 2\Omega_z) z_2 - \omega_y^2 z_3 - \beta z_3^3 - d_{yy} z_4 + u_{z_3} + D_{z_3}} \end{cases} \quad (3.13)$$

Equation (3.13) shows

$$\boldsymbol{\dot{z} = A(z) + Bu} \quad (3.14)$$

The equation (3.14) can be given in its classical form as follows:

$$\boldsymbol{\frac{d}{dt} z(t) = f(z)} \quad (3.15)$$

3.3 Koopman theory

According to the Koopman operator theory, the crucial step to correctly a nonlinear dynamical system is to transform the nonlinear system's original form into an infinite dimensional state space so that the resulting system is linear (Ping, Yin, Li, Liu, & Yang, 2021).

The dynamic in discrete time defines as (Kaiser, Kutz, & Brunton, 2021):

$$\boldsymbol{z_{k+1} = F(z_k)} \quad (3.16)$$

where F is characterized by

$$\boldsymbol{F}\big(\boldsymbol{z}(\boldsymbol{t_0})\big) = \boldsymbol{z}(\boldsymbol{t_0}) + \int_{\boldsymbol{t_0}}^{\boldsymbol{t_0+t}} \boldsymbol{f}\big(\boldsymbol{z}(\boldsymbol{\tau})\big)\boldsymbol{d\tau} \tag{3.17}$$

When a finite-dimensional nonlinear system's dynamics are transferred to an infinite-dimensional function space using the Koopman operator theoretic method, the original system's dynamics become linear. *g* is a real-valued scalar measurement function and an observable, part of an infinite-dimensional Hilbert space. The Koopman operator generates based on this observable as

$$\boldsymbol{Kg} = \boldsymbol{g} \circ \boldsymbol{F} \tag{3.18}$$

Smooth dynamics can be implemented using a continuous system.

$$\frac{\boldsymbol{d}}{\boldsymbol{dt}}\boldsymbol{g}(\boldsymbol{z}) = \boldsymbol{Kg}(\boldsymbol{z}) = \boldsymbol{\nabla g}(\boldsymbol{z}).\boldsymbol{f}(\boldsymbol{z}) \tag{3.19}$$

where the Koopman operator is K. Due to the infinite dimensions of the Koopman operator, which is significant but problematic for operation and representation. Instead of describing the development of all measurement functions in a Hilbert space, applied Koopman analysis approximates the evolution of a subspace covered by a small number of measurement functions. One can get a representation of the Koopman operator in a finite-dimensional matrix by limiting the operator to an invariant subspace. A Koopman invariant subspace is covered by any combination of the eigenfunctions of the Koopman operator

(Kaiser, Kutz, & Brunton, 2021). When eigenvalue λ is satisfied by eigenfunction $\boldsymbol{\varphi}(\boldsymbol{z})$ of the Koopman model.

$$\boldsymbol{\lambda\varphi}(\boldsymbol{z}) = \boldsymbol{\varphi}\big(\boldsymbol{F}(\boldsymbol{z})\big) \tag{3.20}$$

In continuous time, a Koopman eigenfunction $\boldsymbol{\varphi}(\boldsymbol{z})$ is satisfied.

$$\frac{\boldsymbol{d}}{\boldsymbol{dt}}\boldsymbol{\varphi}(\boldsymbol{z}) = \boldsymbol{\lambda\varphi}(\boldsymbol{z}) \tag{3.21}$$

A finite-dimensional approximation is required from the application side to approximate the Koopman operator. The DMD method is one of the approaches that can estimate the Koopman operator (Kaiser, Kutz, & Brunton, 2021).

3.4 DMD method

A strong numerical method DMD utilizes to approximate the Koopman operator.

$$\boldsymbol{Z'} \approx \boldsymbol{AZ} \tag{3.22}$$

where $\boldsymbol{Z'}$ is time-shifted of matrix Z as:

$$\boldsymbol{Z} = [\boldsymbol{z_1} \quad \boldsymbol{z_2} \quad \ldots\ldots]$$

The A can be found according to the equation (3.22):

$$\boldsymbol{A} = \boldsymbol{Z'Z^{+}} \tag{3.23}$$

where + represents the Moore-Penrose pseudoinverse. We may use Singular Value Decomposition (SVD) on the snapshots to determine the dominating properties of the

pseudoinverse of *Z* because a typical calculation involving *A* would need a significant amount of computation due to its huge *n* (Snyder & Song, 2021).

$$\boldsymbol{Z} \approx \boldsymbol{U}\boldsymbol{\Sigma}\boldsymbol{V}^{*} \tag{3.24}$$

where $\boldsymbol{U} \in \boldsymbol{R}^{\boldsymbol{n}\times\boldsymbol{r}}$, $\boldsymbol{\Sigma} \in \boldsymbol{R}^{\boldsymbol{r}\times\boldsymbol{r}}$, $\boldsymbol{V} \in \boldsymbol{R}^{\boldsymbol{n}\times\boldsymbol{r}}$, and $*$ demonstrates the conjugate transpose. SVD's reduced rank for approximating *Z* is *r*. The eigenvectors can be defined as:

$$\Phi = \boldsymbol{Z}'\boldsymbol{V}\boldsymbol{\Sigma}^{-\boldsymbol{1}}\mathrm{W} \tag{3.25}$$

where W is eigenvector of full-rank system dynamic systems.

$$\Phi = \boldsymbol{Z}'\boldsymbol{V}\boldsymbol{\Sigma}^{-\boldsymbol{1}}\mathrm{W} \tag{3.26}$$

Let λ be eigenfunction, then we will have:

$$\boldsymbol{K}\boldsymbol{W} = \boldsymbol{\lambda}\boldsymbol{W} \tag{3.27}$$

where *K* is the Koopman operator.

The linearized dynamic model can be demonstrated as:

$$\frac{\boldsymbol{d}}{\boldsymbol{dt}}\boldsymbol{y} = \boldsymbol{K}\boldsymbol{y} + \boldsymbol{B}\boldsymbol{u} \tag{3.28}$$

3.5 FOPID control

PID controller is a suitable control method that has been used in many industrial applications (Malarvili & Mageshwari, 2022; Guo, Lu, Lin, & Hwang, 2022; Yan, et al.,

2022). It constantly evaluates the error by using its parameters K_p, K_i, and K_d and delivers the correct value. The PID controller can be defined as:

$$\boldsymbol{u_{PID} = K_p e(t) + K_i \int_0^t e(\tau) d\tau + K_d \frac{de(t)}{dt}} \tag{3.29}$$

where $\boldsymbol{e(t) = y - y_d}$, which $\boldsymbol{y_d}$ is desired trajectory.

The main problem of the PID controller is that it's not robust against external disturbances. Also, the stability of the PID controller is another issue that should be taken into consideration during the controller design.

The fractional control method was introduced to improve the controller's performance. It can improve the stability and robustness of common PID controllers. The FOPID controller can be defined as:

$$\boldsymbol{u_{FOPID} = K_p e(t) + K_i D^{-\mu} e(t) + K_d D^{\mu} e(t)} \tag{3.30}$$

where D is the fractional operator defined as $\boldsymbol{D = \frac{d}{dt}}$ and μ is the fractional order. The fractional type that we use in this research is Grunwald-Letnikov (Abdelouahab & Hamri, 2016). The Grunwald-Letnikov fractional derivative of the function $e(t)$ with respect to t is given

$$\boldsymbol{D_t^{\mu} e(t) = lim_{h \to 0} h^{-\mu} \sum_{k=0}^{n} (-1)^k \binom{\mu}{k} f(e(t) - kh)} \tag{3.31}$$

where

$$\binom{\mu}{k} = \frac{\mu(\mu-1)(\mu-2)\dots(\mu-k+1)}{k!} = \frac{\Gamma(\mu+1)}{k!\,\Gamma(\mu-k+1)}$$

A detailed explanation can be observed in (Abdelouahab & Hamri, 2016). The control structure shows in Figure 3.1 .

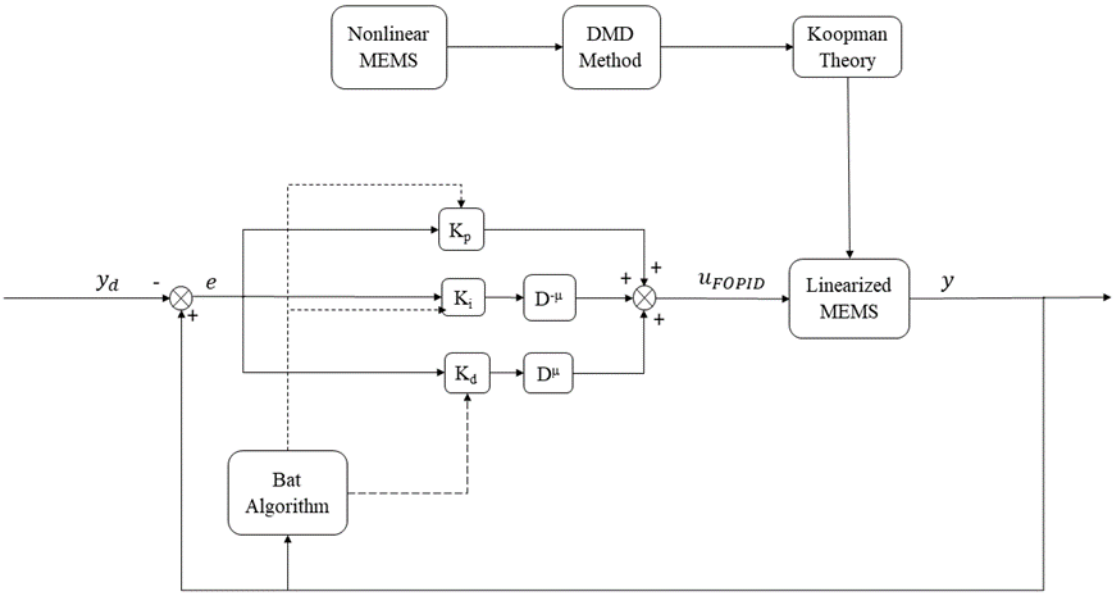

Figure 3.1: The proposed control structure.

One of the main parts of FOPID controller design is how to tune the controller's parameters. The metaheuristic algorithms are rich sources to tune the FOPID controller parameters.

3.6 Bat algorithm to tune the proposed controller parameters

The optimization technique known as the bat bio-inspired algorithm was influenced by how common bats use echolocation to find food. It is introduced in (Yang X. S., A new metaheuristic bat-inspired algorithm, 2010) (Yang X. S., Bat algorithm for multi-objective optimisation., 2012) and used to resolve several optimization issues. The echolocation strategy of bats is used in the algorithm. These bats create an extremely loud sound pulse, then they listen for the echo that is returned from the nearby objects. Depending on the species, their signal bandwidth ranges change through harmonics. The i^{th} bat moves randomly at location x_i with velocity v_i and a set frequency f_{min}. To discover food, the bat changes its wavelength and volume. To improve the echolocation capabilities, the objective function needs to be optimized. It is possible to develop an optimization algorithm from the way a bat searches for the best answer. The algorithms for bat-inspired echolocation can be created by enhancing certain of the microbats' echolocation characteristics. The features of bat echolocation are used to address an optimization issue brought about by the following hypotheses (Sathya & Ansari, 2015).

1- An echolocation is a tool used by all bats to detect distance.

2- To locate prey, bats fly at random speeds of v_i at positions x_i with a fixed frequency and wavelength of f_{min} and a variable wavelength and frequency of A_0.

3- Depending on how close the prey is, they can control their wavelength/frequency and pulse emission rate, $r_i \in$ [0-1].

4- Their loudness decreases from high A_0 to low A_{min} levels as they get closer to the prey.

In real implementations, frequency occurs between [f_{min}, f_{max}] and is chosen to be similar to the size of the domain of interest. For a virtual bat to solve an optimization issue, rules must be developed to specify their locations and velocities in the d-dimensional search space. The following definitions apply to the new location $\boldsymbol{x_i^+}$ and velocity $\boldsymbol{v_i^+}$ at time step t (Mitić & Miljković, 2015).

$$\boldsymbol{f_i = f_{min} + (f_{max} - f_{min})\xi} \tag{3.32}$$

$$\boldsymbol{v_i^t = v_i^{t-1} + \left(x_i^{t-1} - x^*\right) f_i} \tag{3.33}$$

$$\boldsymbol{x_i^t = x_i^{t-1} + v_i^t} \tag{3.34}$$

The current best solution across all N bats is represented by x^*, where $\xi \in$ [0-1] is the random vector generated at random from a uniform distribution. When a new solution is needed for local search, it is determined using the most recent bat loudness A_i and the most variance that can be tolerated max(var) at a time stop, as shown below.

$$\boldsymbol{x_{new} = x_{old} + \varepsilon A_i \max\,(var)} \tag{3.35}$$

The volume drops and the pulse emission rate rises as a bat locate its prey. The bat is heading toward the best option, as shown by

$$\boldsymbol{A_i^{t+1} = \alpha A_i^t, \quad r_i^{t+1} = r_r^{\circ}[1 - e^{-\gamma t}]} \tag{3.36}$$

Where α and γ are constant. Initial boundness is $A_i \in$[0.1-0.9], initial emission rate is $r_0 \in$[0-1], and $\alpha = \gamma$=0.9. The bat algorithm is used for tuning the [K_p, K_i, K_d] parameters of the proposed controller for a MEMS gyroscope. This problem's objective function is described as follows (Rahmani, Ghanbari, & Ettefagh, Robust adaptive control of a bio-inspired robot manipulator using bat algorithm, 2016):

$$\boldsymbol{J = \int_0^{\infty} (w_1 |e(t)| + w_2 u^2(t)) dt + w_3 t_u} \tag{3.37}$$

3.7 Simulation results

A MEMS gyroscope is controlled using the proposed Koopman-BAFOPID controller. Additionally, several comparative methods are used to show how effective the proposed Bat algorithm is in adjusting the Koopman-FOPID parameters. The nonlinear dynamic equations of a MEMS gyroscope generated in this research. All simulations steps

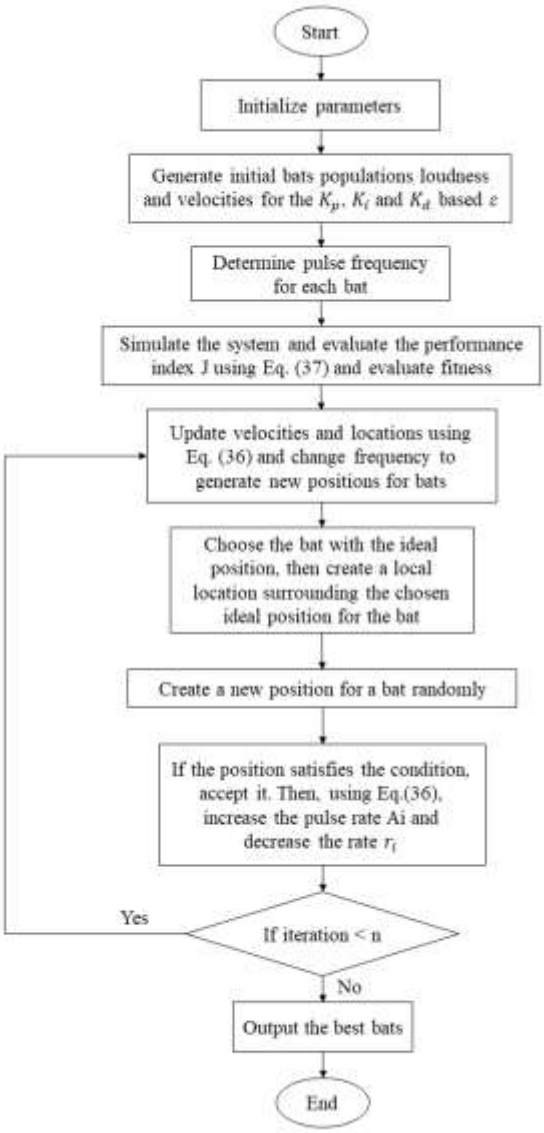

Figure 3.2: Flow chart for a bat algorithm for tuning of Koopman-FOPID parameters.

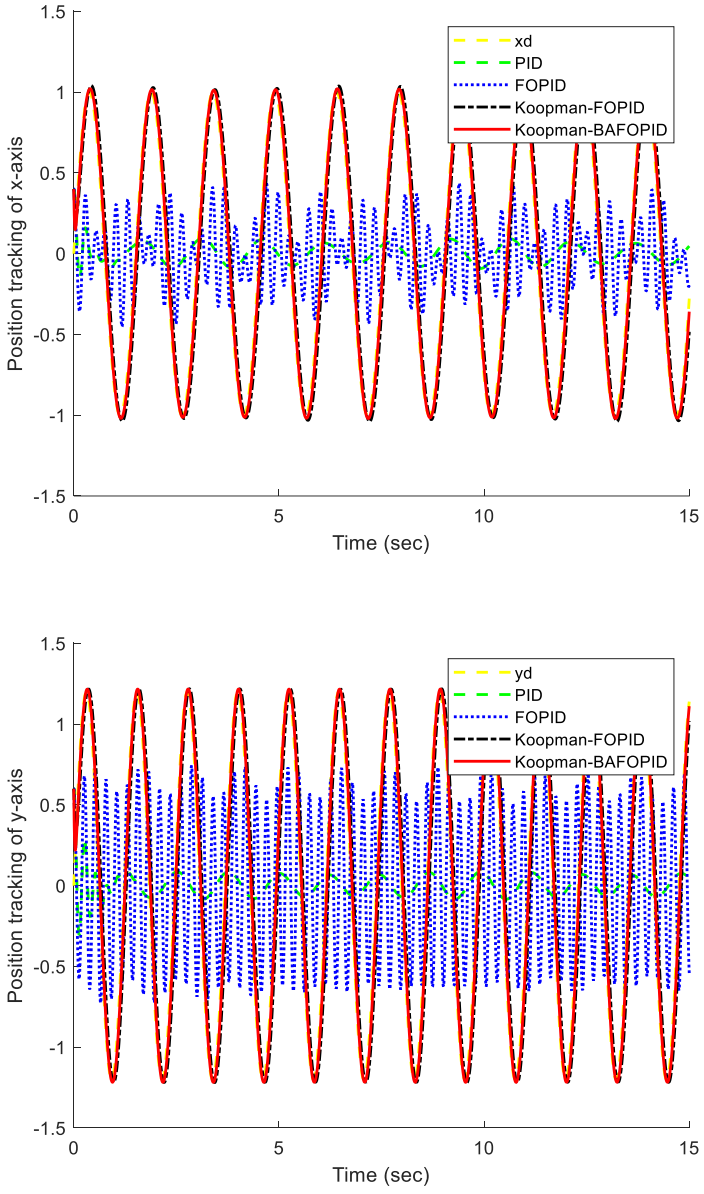

Figure 3.3: Position tracking of x and y under the proposed controllers.

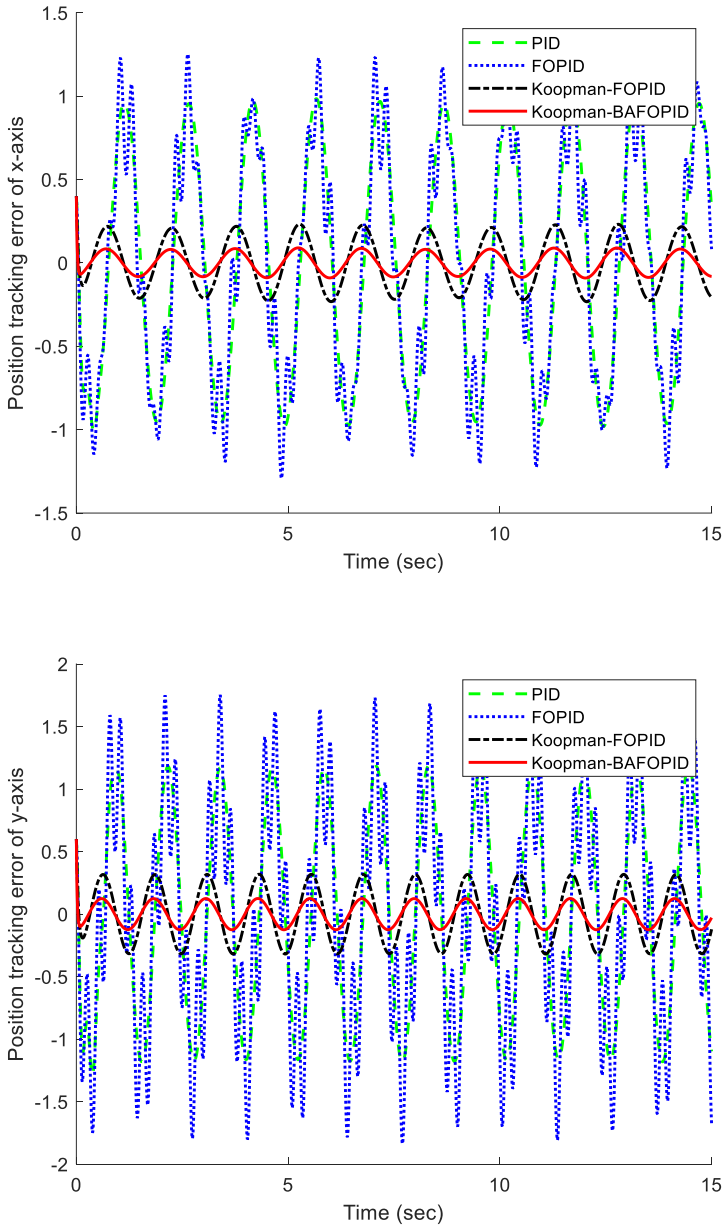

Figure 3.4: Position tracking error of x and y directions under the proposed controllers.

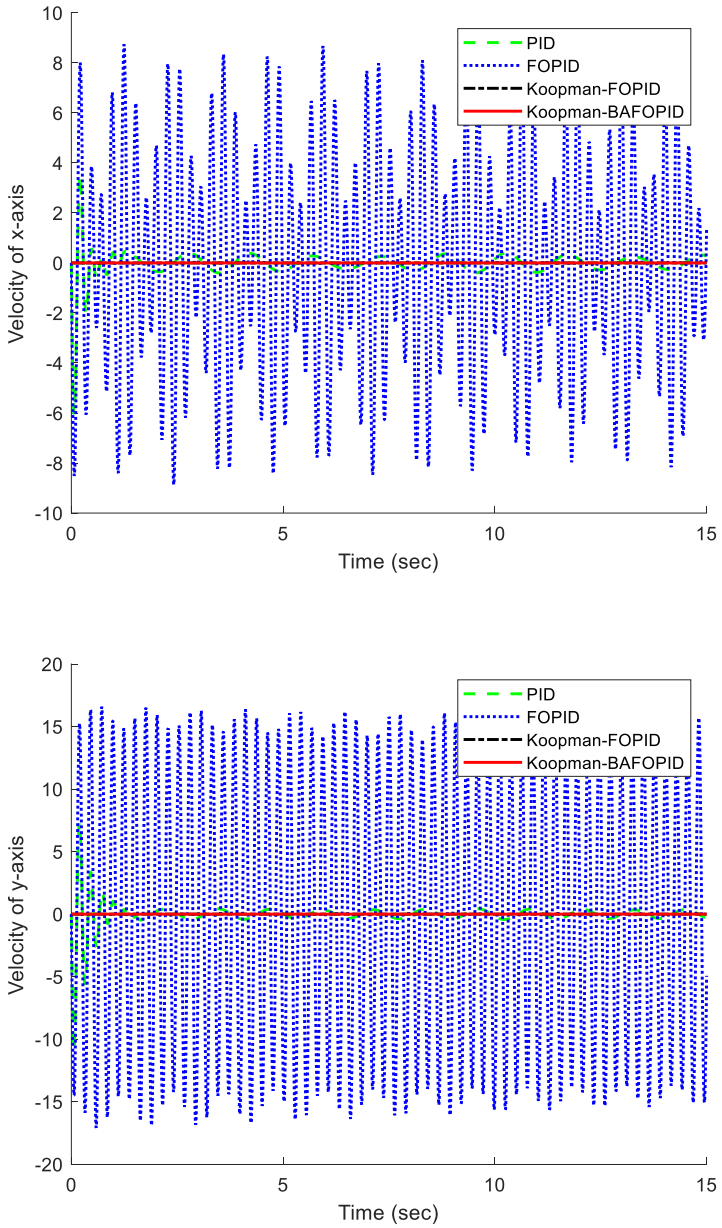

Figure 3.5: Velocity of x and y directions under the proposed controllers.

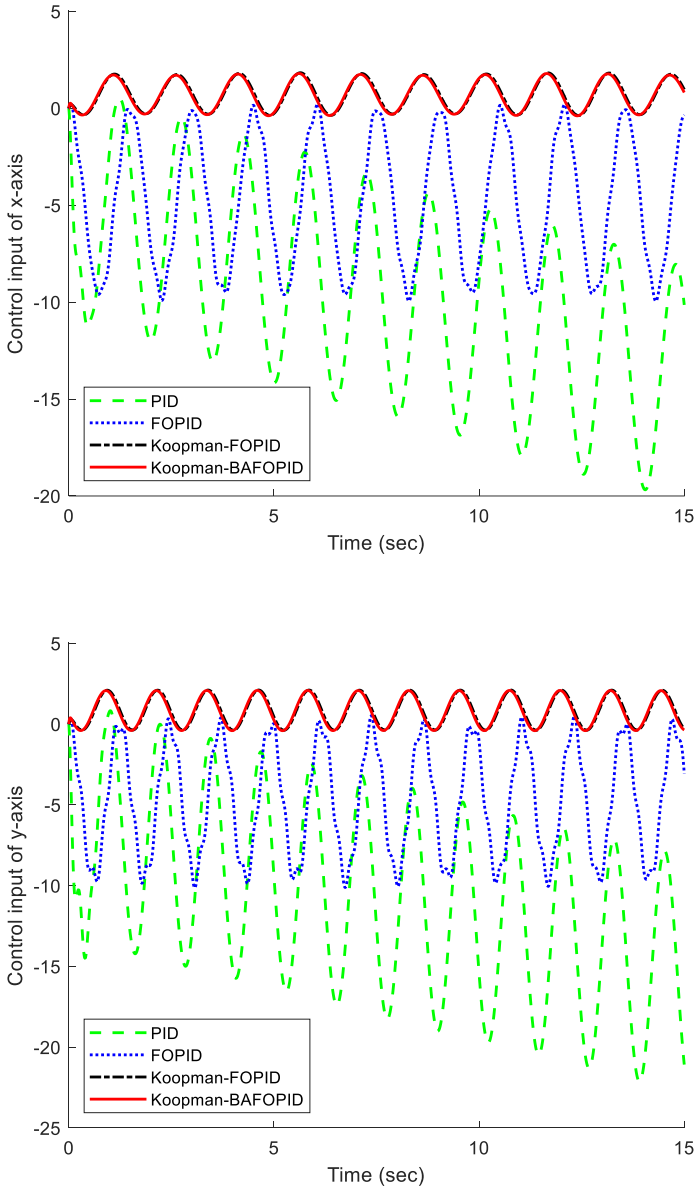

Figure 3.6: Control efforts of x and y directions under the proposed controllers.

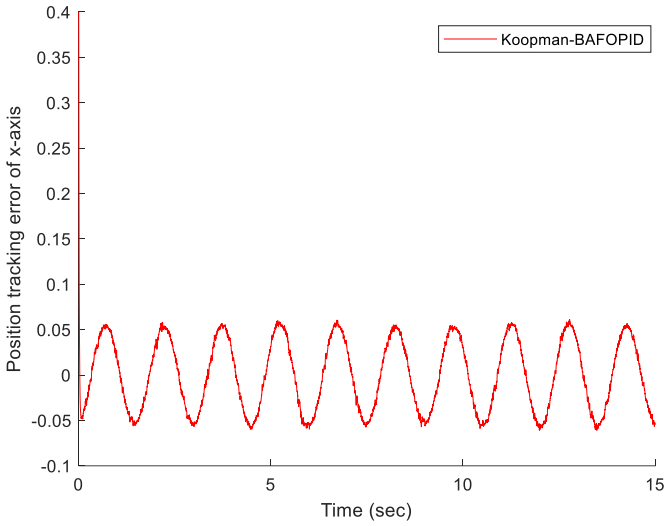
Koopman-BAFOPID
Position tracking error of x-axis
Time (sec)
0.4
0.35
0.3
0.25
0.2
0.15
0.1
0.05
0
-0.05
-0.1
0
5
10
15

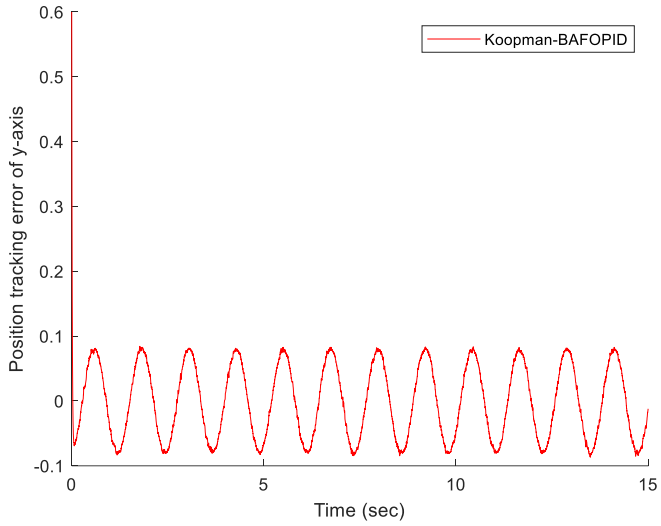

Figure 3.7: Robustness of x and y directions under the proposed controllers.

are simulated using Matlab software. Figure 3.2 shows the flow chart of the bat algorithm step in tuning the Koopman-FOPID controller. The parameters of the proposed controller in this study are as follows: total population = 5; iteration = 20; loudness = 0.5; wavelength = 0.5; frequency f_{min} = 10, f_{max} = 20. The objective function variables are set to w_1=0.99, w_2=0.01, and w_3=2. The tuned parameters of the bat algorithm are K_p=diag{17.9901}, K_i={22.3411}, and K_d={27.2585}. Figure 3.3 shows the trajectory tracking of the x and y directions under PID, FOPID, Koopman-FOPID, and Koopman-BAFOPID controllers. It demonstrates that the proposed Koopman-BAFOPID controller has high tracking performance in comparison with the three other controllers. Figure 3.4 shows the position tracking error of x and y directions under PID, FOPID, Koopman-

FOPID, and Koopman-BAFOPID controllers. It illustrates that the proposed Koopman-BAFOPID controller has low tracking error in comparison with the PID, FOPID, Koopman-FOPID, and Koopman-BAFOPID controllers. Figure 3.5 show the velocity of x and y direction under PID, FOPID, Koopman-FOPID, and Koopman-BAFOPID controllers. A conventional PID controller is applied to nonlinear MEMS gyroscope to control the x and y direction. The main problem with that controller is that it's not stable. Then, a FOPID controller is used to remove the stability problem of conventional PID controllers. Figure 3.6 shows the control inputs under PID, FOPID, Koopman-FOPID, and Koopman-BAFOPID controllers. It demonstrates that the PID controller is not stable by increasing the control efforts when time is increased, but the FOPID controller fixed this problem. Therefore, the using FOPID controller provides better stability along with using the Koopman theory on nonlinear MEMS gyroscopes. The robustness of the proposed control method is verified by random noise *0.5*randn(1,1)* application. Figure 3.7 shows that the proposed control method is robust against external disturbances.

3.8 Conclusion

This paper proposed a new Koopman-BAFOPID control of a nonlinear MEMS gyroscope. The PID controller stability was improved by proposing the FOPID controller. The Koopman theory is used to drive a linear dynamic model of MEMS gyroscope. The

DMD method is used to estimate the Koopman operators numerically. Then, the selected FOPID controller was applied to the linearized MEMS gyroscope dynamic model to control the x and y direction suitably. A bat algorithm was implemented on the Koopman-FOPID controller in order to tune the proposed controller parameters. The simulation results verified that the proposed Koopman-BAFOPID controller has better performance in comparison with PID, FOPID, and Koopman-FOPID controllers in terms of high tracking performance, low tracking error, low control efforts, and high stability.

4 NEW FRACTIONAL ROBUST DATA-DRIVEN CONTROL OF NONLINEAR MEMS GYROSCOPE

4.1 Literature review

One of the useful tools to measure angular velocity is the MEMS gyroscope. By measuring the x and y direction movement of the MEMS gyroscope, angular velocity will be obtained. This device is used in many industries such as the automotive industry and medicine. The most important part of using the MEMS gyroscope is how to control this device appropriately. Several control methods are used to control the MEMS gyroscope such as proportional integral derivative (PID) controller (Rahmani, Komijani, Ghanbari, &

Ettefagh, 2018), sliding mode control (SMC) (Fang, Fu, Ding, & Fei, 2022), and some other controllers (Zhang, Shao, Zhao, Li, & Xu, 2018) (Rahmani & Rahman, A novel compound fast fractional integral sliding mode control and adaptive PI control of a MEMS gyroscope, 2019). However, the mentioned controllers were applied on a linear MEMS gyroscope. There are a few researchers who worked on the nonlinear dynamic model of MEMS gyroscope and controlled it in comparison to linear MEMS gyroscope (Su, et al., 2020).

Linearization of the nonlinear dynamic model will give better information on the behavior of the systems. This will provide some detail to better analyze the system. Koopman's theory is one of the strong approaches to linearizing the nonlinear dynamic model (Chen, Dang, & Han, 2022; Schulze, Doncevic, & Mitsos, 2022; Zhang, Pan, Scattolini, Yu, & Xu, 2022; Lusch, Kutz, & Brunton, 2018). Koopman operators have infinite dimensions and capture nonlinear dynamics in a lifted global linear way. A class of linear predictors is produced by the finite data-driven approximation of Koopman operators, which helps create linear control of nonlinear dynamical systems with minimal computing complexity (Zhang, Pan, Scattolini, Yu, & Xu, 2022). The main part of applying Koopman's theory to nonlinear dynamic equations is how to approximate the Koopman operator. The DMD method is one of the most prevalent methods in estimating the Koopman operator (Qian & Chou, 2021; Kou, Le Clainche, & Ferrer, 2022; Sinha,

Nandanoori, & Yeung, 2020). Nathan Kutz, Proctor, & Brunton, (2018) investigate using Koopman theory to solve data-driven spatiotemporal systems and nonlinear partial differential equations. They show that an appropriate approximation to the nonlinear dynamics depends on the observables selected for building the Koopman operator. The DMD technique may be used to compute a finite-dimensional approximation of the Koopman operator, together with its eigenfunctions, eigenvalues, and Koopman modes, if such observables can be discovered.

Several control methods are used to control the linearized dynamic model by Koopman theory such as linear quadratic regulator (LQR) (Mamakoukas, Castano, Tan, & Murphey, (2019, June); Gibson, Yee, & Calvisi, 2021) and model predictive controller (MPC) (Arbabi, Korda, & Mezić, (2018, December); Calderón, Schulz, Oehlschlägel, & Werner, (2021, June)). The LQR and MPC controllers have suitable performances, but the main drawbacks of those controllers are not robust against external disturbances. The FOSMC is a strong robust control method that can suppress external perturbations. The reason that makes this controller a strong control approach is that the fractional order used in the sliding mode surface provides the ability to select the fraction power of error. This issue provides excellent flexibility to select the best sliding mode surface. Therefore, the dynamic states of the linearized dynamics model can suitably slide close to the normal

behavior of the system. It causes to provides better control performance in terms of high tracking performance, low tracking error, and robustness.

Most of the previous works related to MEMS gyroscopes were about the control of linear dynamics of MEMS gyroscopes by FOSMC. However, the FOSMC was used in combination with the other controller to benefit from the advantages of other controllers like reducing the chattering phenomenon (Huimin, Liang, Yunxiang, Hailong, & Cheng, (2019, June); Rahmani, Rahman, & Ghommam, Compound Fractional Integral Terminal Sliding Mode Control and Fractional PD Control of a MEMS Gyroscope, 2020) and improving tracking performance (Rahmani & Rahman, A new adaptive fractional sliding mode control of a MEMS gyroscope, 2019). Based on high-gain and disturbance observers, a dynamic backstepping sliding mode controller with a fractional order sliding surface and a fuzzy boundary layer is created to regulate the operation of a MEMS gyroscope (Fazeli Asl & Moosapour, 2021). A combination of sliding mode and a reliable nonlinear backstepping controller is applied to suppress the system uncertainties. The sliding surface in this model is chosen to be of fractional order to improve the degree of freedom of the controller. In addition to the initial sliding surface, a new dynamic sliding surface is utilized to considerably minimize the chattering phenomena in the control signal. Fuzzy control theory is also used to regulate the boundary layer. Wang & Fei (2021) proposed the use of a trajectory tracking control system with a neural network estimator to sustain the

vibrations of the gyroscope-proof mass. A recurrent Chebyshev fuzzy neural network with a self-evolving mechanism and a fractional controller based on the terminal sliding mode are both included in the suggested control system. A self-evolving recurrent Chebyshev fuzzy neural network is presented to reduce the need for nonlinear functional certainty, and the fractional-order terminal sliding-mode control may guarantee the tracking error is exponentially stable.

The contributions of this research are as follows:

1- A nonlinear dynamic model of the MEMS gyroscope is introduced.

2- The Koopman theory is applied to linearize the nonlinear model of the MEMS gyroscope.

3- The DMD method is used to approximate the Koopman operator.

4- The FOSMC is implemented on the linearized dynamic model to control the MEMS gyroscope.

5- A new compound control method is applied to improve the control method of the FOSMC such as reducing the control efforts.

6- Simulation results verified the performance of the proposed controller.

4.2 Fractional sliding mode control

The FOSMC is a robust control method that can suppress external perturbations. This control method is a flexible method that can provide fraction derivative power of error (Gao, Zhang, Ouyang, & Mei, 2020; Fei & Feng, Fractional-order finite-time super-twisting sliding mode control of micro gyroscope based on double-loop fuzzy neural network, 2020; Mujumdar, Tamhane, & Kurode, 2015). This issue will provide the opportunity for choosing the suitable sliding mode surface that is the most important part of designing FOSMC. The fractional sliding mode surface defines as:

$$\boldsymbol{s(t)} = \boldsymbol{\dot{e}(t)} + \boldsymbol{\alpha D^{\mu} e(t)} \tag{4.1}$$

where $\boldsymbol{e(t)} = \boldsymbol{q_d} - \boldsymbol{q}$ and D is the fractional operator defined as $\boldsymbol{D} = \frac{\boldsymbol{d}}{\boldsymbol{dt}}$ and μ is the fractional order.

The FOSMC contains two control sections: equivalent control law and reaching control law. The equivalent control can be obtained by $\boldsymbol{\dot{s}(t)} = \boldsymbol{0}$. Taking the derivative from equation (4.1) produces

$$\boldsymbol{\dot{s}(t)} = \boldsymbol{\ddot{e}(t)} + \boldsymbol{\alpha\mu D^{\mu+1} e(t)} = \boldsymbol{\ddot{q}_d} - \boldsymbol{\ddot{q}} + \boldsymbol{\alpha\mu D^{\mu+1} e(t)} \tag{4.2}$$

Equation (3.10) is substituted into equation (4.2) to produce

$$\boldsymbol{\dot{s}(t)} = \boldsymbol{\ddot{q}_d} + \boldsymbol{Y\dot{q}} + \boldsymbol{Pq} + \boldsymbol{\beta q^3} - \boldsymbol{u(t)} - \boldsymbol{D(t)} + \boldsymbol{\alpha\mu D^{\mu+1} e(t)} \tag{4.3}$$

The $u_{eq}(t)$ can be described by $\boldsymbol{\dot{s}(t)} = \boldsymbol{0}$ as

$$\boldsymbol{u_{eq}(t) = \ddot{q}_d + Y\dot{q} + Pq + \beta q^3 - D(t) + \alpha\mu D^{\mu+1} e(t)} \quad (4.4)$$

The reaching control law introduces as

$$\boldsymbol{u_r(t) = K_r s(t)} \quad (4.5)$$

where K_r is a positive constant. Therefore, the control input is defined as

$$\boldsymbol{u_{FOSMC}(t) = u_{eq}(t) + u_r(t)} \quad (4.6)$$

A powerful technique for demonstrating the stability of the FOSMC is the Lyapunov theory. It is characterized as:

$$\boldsymbol{V(t) = \frac{1}{2} s(t) s^T(t)} \quad (4.7)$$

Taking the derivative from equation (4.7) describes

$$\boldsymbol{\dot{V}(t) = s^T(t)\dot{s}(t)} \quad (4.8)$$

The outcome of putting equation (4.3) into equation (4.8)

$$\boldsymbol{\dot{V}(t) = s^T(t)(\ddot{q}_d + Y\dot{q} + Pq + \beta q^3 - u(t) - D(t) + \alpha\mu D^{\mu+1} e(t))} \quad (4.9)$$

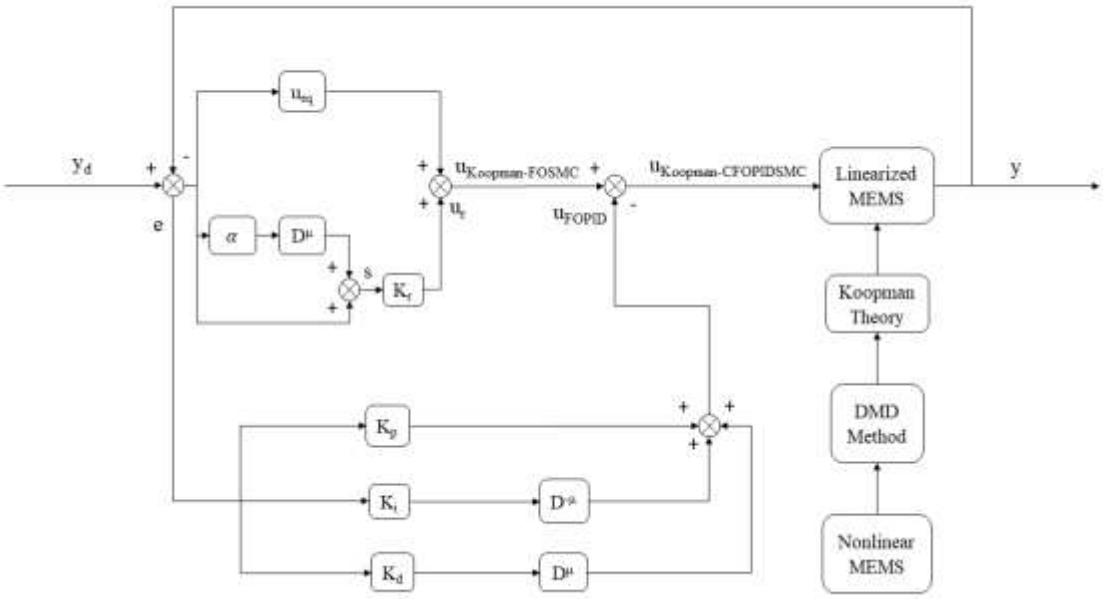

Figure 4. 1: The proposed controller block diagram.

Substituting equation (4.6) into equation (4.9) produces

$$\dot{\boldsymbol{V}}(\boldsymbol{t}) = \boldsymbol{s^T}(\boldsymbol{t})(\ddot{\boldsymbol{q}}_{\boldsymbol{d}} + \boldsymbol{Y}\dot{\boldsymbol{q}} + \boldsymbol{Pq} + \boldsymbol{\beta q^3} - \boldsymbol{u_{eq}}(\boldsymbol{t}) - \boldsymbol{u_r}(\boldsymbol{t}) - \boldsymbol{D}(\boldsymbol{t}) \quad (4.10)$$

$$+\boldsymbol{\alpha\mu D^{\mu+1}e}(\boldsymbol{t}))$$

Equation (4.4) used in equation (4.10) results in

$$\dot{\boldsymbol{V}}(\boldsymbol{t}) = \boldsymbol{s^T}(\boldsymbol{t})(\ddot{\boldsymbol{q}}_{\boldsymbol{d}} + \boldsymbol{Y}\dot{\boldsymbol{q}} + \boldsymbol{Pq} + \boldsymbol{\beta q^3} - \ddot{\boldsymbol{q}}_{\boldsymbol{d}} - \boldsymbol{Y}\dot{\boldsymbol{q}} - \boldsymbol{Pq} - \quad (4.11)$$

$$\boldsymbol{\beta q^3} + \boldsymbol{D}(\boldsymbol{t}) - \boldsymbol{\alpha\mu D^{\mu+1}e}(\boldsymbol{t}) - \boldsymbol{u_r}(\boldsymbol{t}) - \boldsymbol{D}(\boldsymbol{t}) + \boldsymbol{\alpha\mu D^{\mu+1}e}(\boldsymbol{t}))$$

Simplifying equation (4.11) produces

$$\dot{\boldsymbol{V}}(\boldsymbol{t}) = \boldsymbol{s}^{\boldsymbol{T}}(\boldsymbol{t})(-\boldsymbol{u}_{\boldsymbol{r}}(\boldsymbol{t})) \tag{4.12}$$

Substituting equation (4.5) into equation (4.12) describes

$$\dot{\boldsymbol{V}}(\boldsymbol{t}) = \boldsymbol{s}^{\boldsymbol{T}}(\boldsymbol{t})(-\boldsymbol{K}_{\boldsymbol{r}}\boldsymbol{s}(\boldsymbol{t})) \tag{4.13}$$

Equation (4.13) shows that the $\dot{\boldsymbol{V}}(\boldsymbol{t}) < \boldsymbol{0}$. Therefore, the proposed controller is stable.

In this study, we employ the Grunwald-Letnikov fractional type (Abdelouahab & Hamri, 2016). The Grunwald-Letnikov fractional derivative of the function *e(t)* with respect to *t* is given

$$\boldsymbol{D}_{\boldsymbol{t}}^{\boldsymbol{\mu}}\boldsymbol{e}(\boldsymbol{t}) = \boldsymbol{lim}_{\boldsymbol{h}\to\boldsymbol{0}}\boldsymbol{h}^{-\boldsymbol{\mu}}\sum_{\boldsymbol{k}=\boldsymbol{0}}^{\boldsymbol{n}}(-\boldsymbol{1})^{\boldsymbol{k}}\binom{\boldsymbol{\mu}}{\boldsymbol{k}}\boldsymbol{f}(\boldsymbol{e}(\boldsymbol{t}) - \boldsymbol{kh}) \tag{4.14}$$

where

$$\binom{\boldsymbol{\mu}}{\boldsymbol{k}} = \frac{\boldsymbol{\mu}(\boldsymbol{\mu}-\boldsymbol{1})(\boldsymbol{\mu}-\boldsymbol{2})\ldots(\boldsymbol{\mu}-\boldsymbol{k}+\boldsymbol{1})}{\boldsymbol{k}!} = \frac{\boldsymbol{\Gamma}(\boldsymbol{\mu}+\boldsymbol{1})}{\boldsymbol{k}!\,\boldsymbol{\Gamma}(\boldsymbol{\mu}-\boldsymbol{k}+\boldsymbol{1})}$$

A detailed explanation of the Grunwald-Letnikov method can be found in (Abdelouahab & Hamri, 2016). The proposed control method block diagram is shown in Figure 4. 1.

4.3 Koopman fractional sliding mode control

The fractional sliding mode surface can be defined as:

$$\boldsymbol{s(t) = e(t) + \alpha D^{\mu} e(t)} \tag{4.15}$$

where $\boldsymbol{e(t) = y_d - y}$. Taking the derivative from equation (4.15) produce

$$\boldsymbol{\dot{s}(t) = \dot{e}(t) + \alpha \mu D^{\mu+1} e(t) = \dot{y}_d - \dot{y} + \alpha \mu D^{\mu+1} e(t)} \tag{4.16}$$

Substituting equation (3.28) into equation (4.16) provides

$$\boldsymbol{\dot{s}(t) = \dot{y}_d - Ky - Bu + \alpha \mu D^{\mu+1} e(t)} \tag{4.17}$$

The equivalent control can be demonstrated by $\boldsymbol{\dot{s} = 0}$ as:

$$\boldsymbol{u_{eq}(t) = B^{-1}(\dot{y}_d - Ky + \alpha \mu D^{\mu+1} e(t))} \tag{4.18}$$

The reaching control law defines as:

$$\boldsymbol{u_r(t) = K_r s(t)} \tag{4.19}$$

The Koopman-FOSMC can be demonstrated as

$$\boldsymbol{u_{Koopman-FOSMC}(t) = u_{eq}(t) + u_r(t)} \tag{4.20}$$

The stability of the Koopman-FOSMC controller can be proved by using the Lyapunov theory as:

$$\boldsymbol{V(t) = \frac{1}{2} s(t) s^T(t)} \tag{4.21}$$

Taking the derivative from equation (4.21) results

$$\boldsymbol{\dot{V}(t) = s^T(t) \dot{s}(t)} \tag{4.22}$$

Substituting equation (4.17) into equation (4.22) provides

$$\dot{\boldsymbol{V}}(\boldsymbol{t}) = \boldsymbol{s}^{\boldsymbol{T}}(\boldsymbol{t})(\dot{\boldsymbol{y}}_{\boldsymbol{d}} - \boldsymbol{K}\boldsymbol{y} - \boldsymbol{B}\boldsymbol{u} + \boldsymbol{\alpha}\boldsymbol{\mu}\boldsymbol{D}^{\boldsymbol{\mu}+\mathbf{1}}\boldsymbol{e}(\boldsymbol{t})) \quad (4.23)$$

Equation (4.20) is substituted into equation (4.23) to produce

$$\dot{\boldsymbol{V}}(\boldsymbol{t}) = \boldsymbol{s}^{\boldsymbol{T}}(\boldsymbol{t})(\dot{\boldsymbol{y}}_{\boldsymbol{d}} - \boldsymbol{K}\boldsymbol{y} - \boldsymbol{B}\boldsymbol{u}_{\boldsymbol{eq}}(\boldsymbol{t}) - \boldsymbol{B}\boldsymbol{u}_{\boldsymbol{r}}(\boldsymbol{t}) + \boldsymbol{\alpha}\boldsymbol{\mu}\boldsymbol{D}^{\boldsymbol{\mu}+\mathbf{1}}\boldsymbol{e}(\boldsymbol{t})) \quad (4.24)$$

Substituting equation (4.18) into equation (4.24) provides

$$\dot{\boldsymbol{V}}(\boldsymbol{t}) = \boldsymbol{s}^{\boldsymbol{T}}(\boldsymbol{t})(\dot{\boldsymbol{y}}_{\boldsymbol{d}} - \boldsymbol{K}\boldsymbol{y} - \boldsymbol{B}(\boldsymbol{B}^{-\mathbf{1}}(\dot{\boldsymbol{y}}_{\boldsymbol{d}} - \boldsymbol{K}\boldsymbol{y} + \boldsymbol{\alpha}\boldsymbol{\mu}\boldsymbol{D}^{\boldsymbol{\mu}+\mathbf{1}}\boldsymbol{e}(\boldsymbol{t}))) \quad (4.25)$$

$$- \boldsymbol{B}\boldsymbol{u}_{\boldsymbol{r}}(\boldsymbol{t}) + \boldsymbol{\alpha}\boldsymbol{\mu}\boldsymbol{D}^{\boldsymbol{\mu}+\mathbf{1}}\boldsymbol{e}(\boldsymbol{t}))$$

Simplifying the equation (4.25) produces

$$\dot{\boldsymbol{V}}(\boldsymbol{t}) = \boldsymbol{s}^{\boldsymbol{T}}(\boldsymbol{t})(-\boldsymbol{B}\boldsymbol{u}_{\boldsymbol{r}}(\boldsymbol{t})) \quad (4.26)$$

Substituting equation (4.19) into equation (4.26) provides

$$\dot{\boldsymbol{V}}(\boldsymbol{t}) = \boldsymbol{s}^{\boldsymbol{T}}(\boldsymbol{t})(-\boldsymbol{B}\boldsymbol{K}_{\boldsymbol{r}}\boldsymbol{s}(\boldsymbol{t})) \quad (4.27)$$

The $\dot{\boldsymbol{V}}(\boldsymbol{t}) < \mathbf{0}$ according to the equation (4.27). The suggested controller is hence stable.

4.4 New proposed control method

Most of the controllers have some disadvantages. The Koopman-FOSMC controller provides robustness and FOPID has high tracking performance. By combining

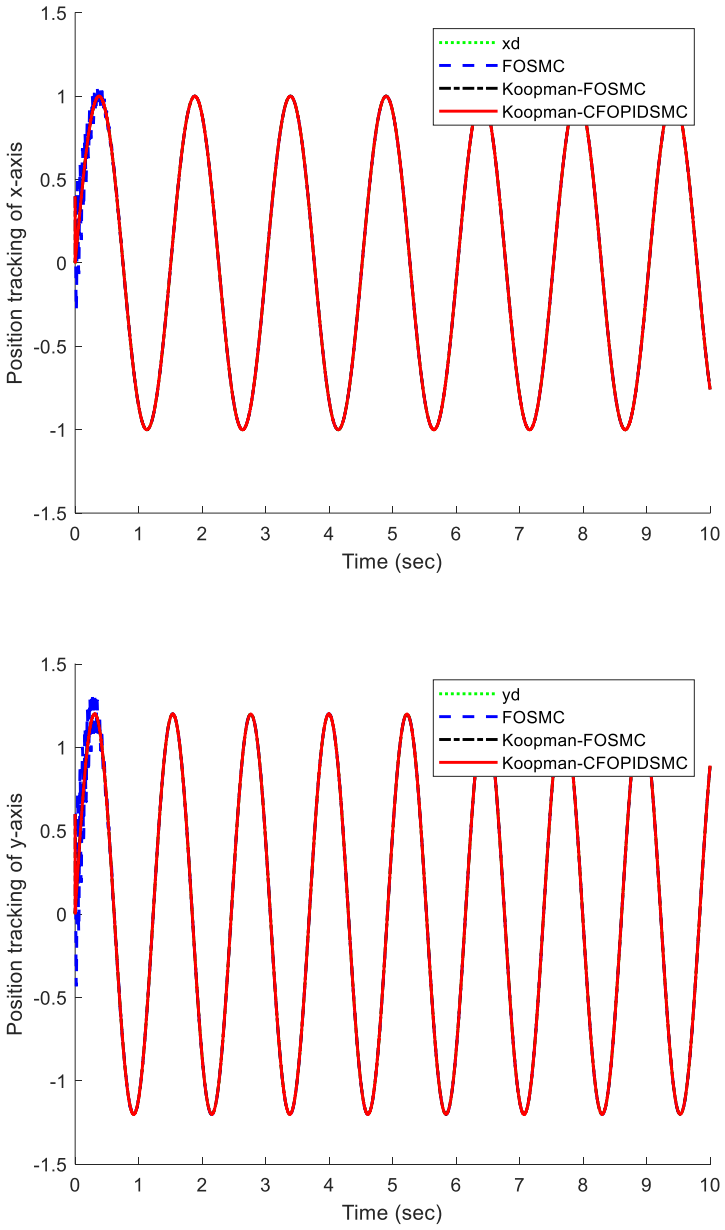

Figure 4.2: The position tracking of x and y directions under the proposed controllers.

the Koopman-FOSMC and FOPID controllers, the new compound controller will be obtained which benefits the advantages of both controllers. The new proposed control method defines as:

$$\boldsymbol{u_{Koopman-CFOPIDSMC}(t) = u_{Koopman-FOSMC}(t) - u_{FOPID}(t)} \quad (4.28)$$

where $\boldsymbol{u_{FOPID}(t)}$ can be defined as:

$$\boldsymbol{u_{FOPID}(t) = K_p e(t) + K_i D^{-\mu} e(t) + K_d D^{\mu} e(t)} \quad (4.29)$$

where are the $\boldsymbol{K_p}$, $\boldsymbol{K_i}$ and $\boldsymbol{K_d}$ are the FOPID controller's gains.

4.5 Simulation results

This research applies a new compound control method to control nonlinear MEMS gyroscope dynamics. The simulations are done in MATLAB software. The proposed controller parameters are as follows:

$\boldsymbol{\alpha = diag\{10, 10\}}$	$\boldsymbol{\mu = 0.75}$	$\boldsymbol{K_r = diag\{10, 10\}}$
$\boldsymbol{K_p = diag\{100, 100\}}$	$\boldsymbol{K_i = diag\{40, 40\}}$	$\boldsymbol{K_d = diag\{70, 70\}}$

The initial values of position are $\boldsymbol{q_{0x} = 0.4}$ and $\boldsymbol{q_{0y} = 0.6}$. Also, the initial velocity values are as $\boldsymbol{\dot{q}_{0x} = 0}$ and $\boldsymbol{\dot{q}_{0y} = 0}$. The desired trajectory tracking for the x-axis is $\boldsymbol{q_{dx} = \sin(4.17t)}$ and the y-axis is $\boldsymbol{q_{dy} = 1.2\sin(5.11t)}$.

Figure 4.2 shows the position tracking of the x-axis and y-axis under FOSMC, Koopman-FOSMC and, Koopman-CFOPIDSMC. The conventional FOSMC controller has a low tracking trajectory in comparison with two other controllers such as the Koopman-FOSMC and, Koopman-CFOPIDSMC. It illustrates that the data-driven Koopman method affects highly improving tracking performance. Figure 4.3 illustrates the position tracking error of the x and y axis under FOSMC, Koopman-FOSMC and, Koopman- CFOPIDSMC. The proposed controller has a low tracking error in comparison with the FOSMC and, Koopman-FOSMC. Figure 4.4 shows the velocity of the x and y axis under the proposed controllers. Figure 4.5 shows the input control efforts under the FOSMC, Koopman- FOSMC and, Koopman-CFOPIDSMC controllers. The control input under conventional FOSMC reached 200 (N.m) in some cases. When the Koopman method was used, the control inputs were significantly reduced. Also, the main benefit of the compound controller (Koopman-CFOPIDSMC) is reducing the control input signals. A small part of the figures was magnified to show the reduction of the control input by implementing the Koopman-CFOPIDSMC controller.

4.6 Conclusions

This paper proposed a new compound controller based on the data-driven Koopman method. First, a conventional FOSMC is applied on a nonlinear MEMS gyroscope dynamic

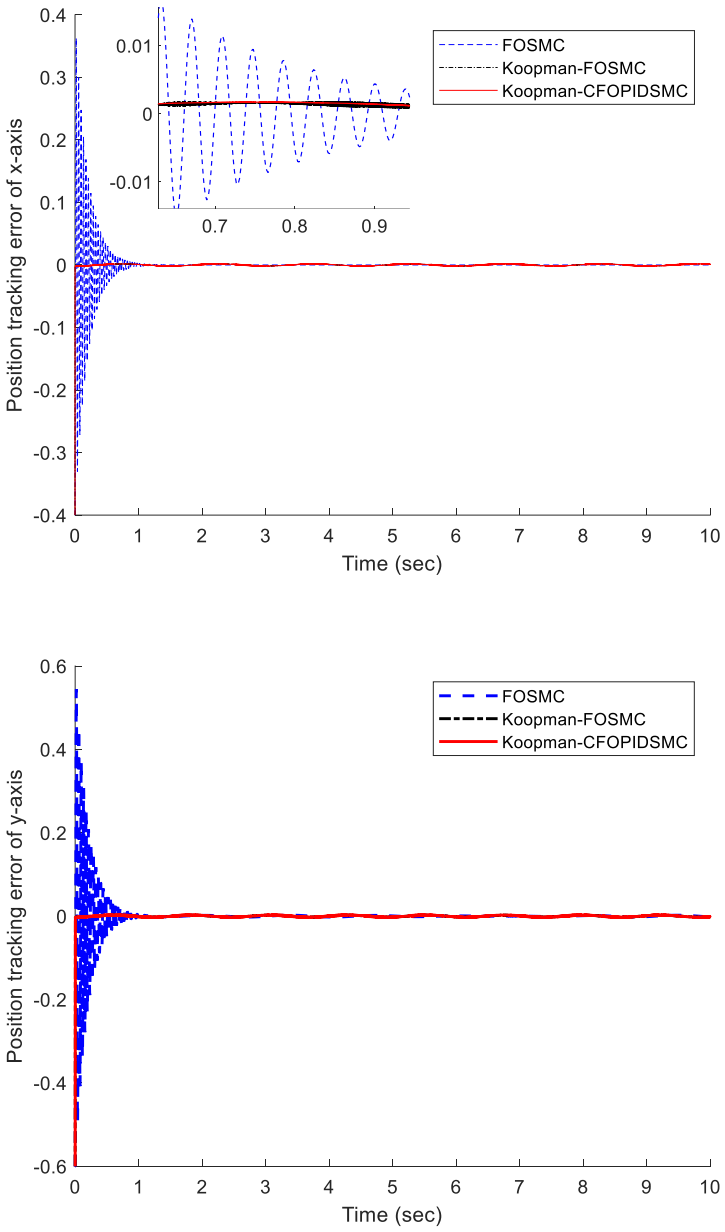

Figure 4.3: The position tracking error of x and y direction under the proposed controllers.

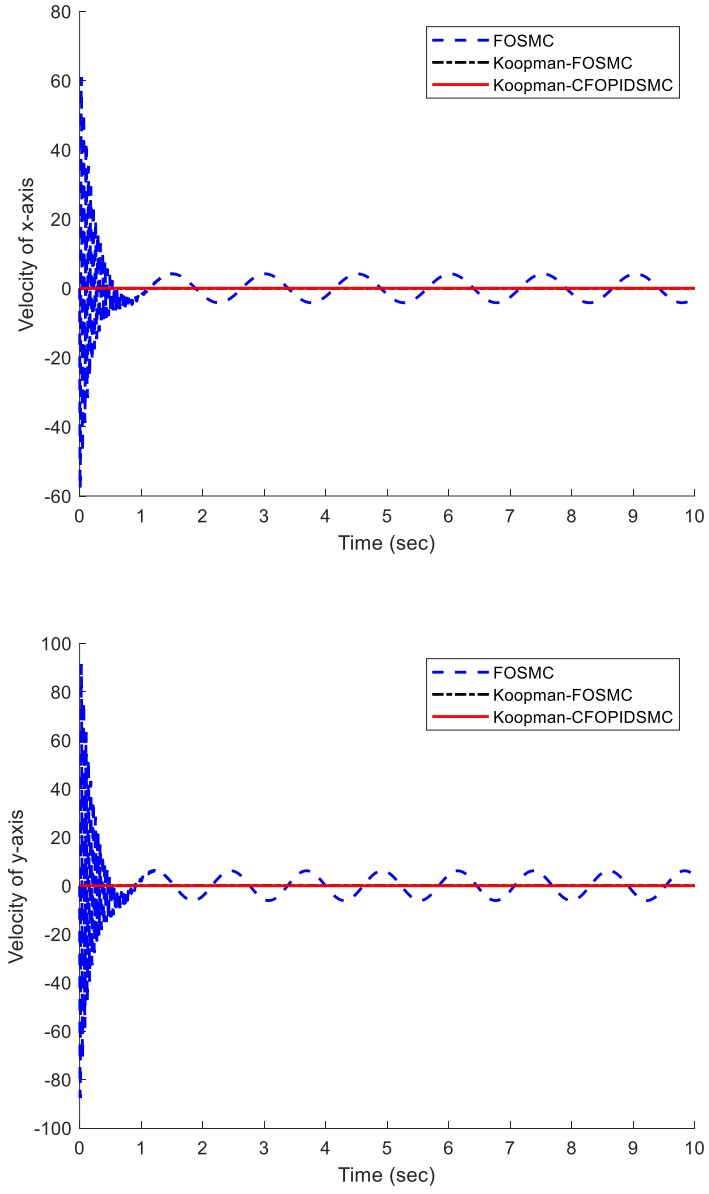

Figure 4.4: Velocity of x and y axis under the proposed controllers.

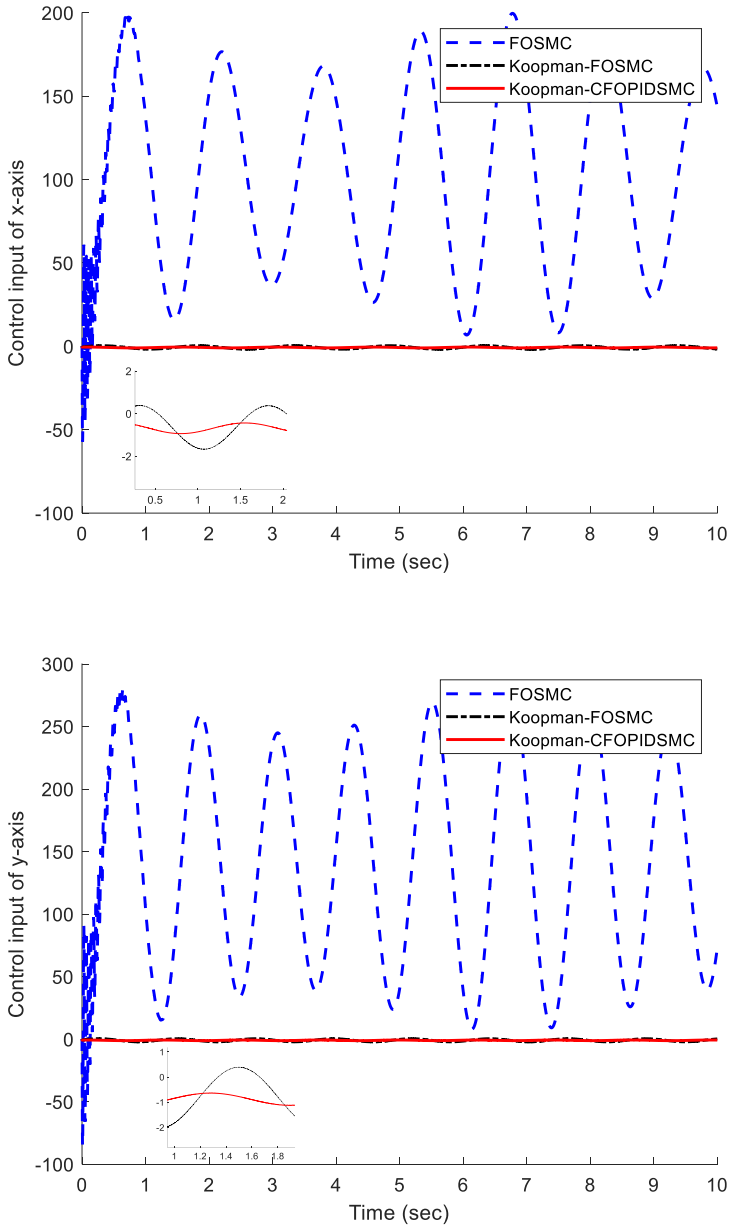

Figure 4.5: Control input of x and y direction under the proposed controllers.

model. Then, the Koopman theory is used to linearize the nonlinear dynamic model of the MEMS gyroscope. The main problem with using the Koopman theory is how to obtain the Koopman operator. The DMD method was used to obtain the Koopman operator. When the model was linearized by the Koopman method, the FOSMC was used to control the x and y-axis of the linearized model of the MEMS gyroscope. The results illustrated that using the Koopman method will significantly improve the controller performance. Finally, a new compound controller is proposed to improve trajectory tracking and reduce the control inputs. Simulation results verified the performance of the Koopman-CFOPIDSMC was better than the FOSMC and Koopman-FOSMC.

5 OPTIMAL CONTROL OF A MEMS GYROSCOPE BASED ON THE KOOPMAN THEORY

5.1 Literature review

MEMS gyroscopes are the small size device that can measure angular velocity by x and y motions (Cui & Zhao, (2021, January; Wang & Fei, (2021, January); Varghese & Priya, (2018, July)). The control of the MEMS gyroscopes is so important because they constantly encounter disturbances. Different control systems have been applied to control MEMS gyroscope eff. Rahmani in (Rahmani M. , 2018) proposed a new hybrid fractional sliding mode control to reduce the chattering phenomenon. The main drawback of conventional sliding mode control is creating a chattering phenomenon. A novel parallel control method is applied to reduce the chattering created by the sliding mode controller. The fractional controller continuously evaluated the error and corrected the error value. Zhou, et al. (2021) proposed an adaptive fuzzy proportional derivative integral (PID) controller to have the minimum value of the maximum overshoot problem. According to the input error and error change rate, the fuzzy controller online modifies the PID controller's settings. Response time of the gyroscope's closed-loop is decreased from 1.09 s to 0.54 s, and overshoot is decreased from 20% to 0.004%, with no deterioration of angle random walk or bias instability. Rahmani, Komijani, Ghanbari, & Ettefagh (2018)

introduced a compound PID sliding mode control method to control the x and y direction of the MEMS gyroscope. Then, a multi-objective bat algorithm is applied to tune the proposed controller parameters. The proposed control method reduced the chattering phenomenon, improved tracking performance, and reduced maximum overshoot. The mentioned controller methods and most of the other works (Luo, Yang, Li, & Ouakad, 2022; Zirkohi, 2022; Shi, Shao, & Zhang, 2020) are applied to the linear dynamic model of the MEMS gyroscope.

The Koopman operator is a strong tool for use in complex nonlinear dynamic systems. This theory will use the data-driven method to control nonlinear dynamic systems with high dimensional nonlinearity (Arbabi, Introduction to Koopman operator theory of dynamical systems, 2018). Abraham & Murphey (2019) proposed a Koopman-based controller that provides fast learning. They demonstrate the enhanced model-based control performance with an actuated Van der Pol system to linearize the nonlinear model by using the Koopman operator. The Koopman operator model of dynamical systems is then used in conjunction with information-theoretic approaches to design a controller for active learning of robot dynamics. It is demonstrated that the active learning controller accelerates the rate of information concerning the Koopman operator. The proposed method is applied on a real-time quadcopter. Korda & Mezić (2020) proposed a novel data-driven method predictor for generating the eigenfunction of the Koopman operator. The predictor thus

developed is a linear controlled dynamical system and is easily implementable in the Koopman model predictive control framework to control nonlinear dynamical systems using the linear control method. The numerical simulations verified the controller and predictor performance. Bruder et al. (2020) proposed a Koopman-based controller design to control a soft robot. To build explicit dynamical models of soft robotics and control them using model-based control techniques, the Koopman operator theory offers a solution. This method is data-driven, but it produces a control-oriented model that is explicit rather than merely a "black-box" input-output mapping. The control design for soft robotics is discussed in this article along with the Koopman-based system identification methodology used to identify the system. The Koopman-based technique is used to create three controllers for a pneumatic soft robot arm, and their performance is assessed in relation to several practical trajectory-following tasks. These Koopman-based controllers have an average tracking error that is more than three times lower than a benchmark controller built on a linear state-space model of the same system, proving the effectiveness of the Koopman technique in soft robot control. Folkestad & Burdick, (2021, May) proposed a nonlinear controller based on Koopman's theory to improve computational efficiency for a planar quadrotor. Using the Koopman operator on the systems will improve the controller in the data-driven form (Mamakoukas, Castano, Tan, & Murphey, (2019, June)) to have high tracking performance and less maximum overshoot (Son, Narasingam, & Kwon, (2021,

May); Goswami & Paley, 2021). The Koopman operator can be used for the linearization of the nonlinear dynamic model.

LQR is an optimal control method that can be used to control the linearized dynamic model (Brunton, Brunton, Proctor, & Kutz, 2016). A data-driven paradigm for the linear embedding of nonlinear systems is presented in (Mamakoukas, Castano, Tan, & Murphey, (2019, June)). The authors provide a systematic, data-driven strategy for developing a linear representation in terms of higher-order derivatives of the underlying nonlinear dynamics by utilizing structural knowledge of generic nonlinear dynamics and the Koopman operator. The nonlinear system is then regulated using an LQR feedback strategy, whose gains only need to be calculated once, using the linear representation. The proposed control method is compared with backstepping control by implementing it on the fish robot. The results verified the proposed control method.

In this method, an optimal Koopman control method is implemented on a MEMS gyroscope. The contribution of this paper will be described as:

1- Discussion of nonlinear MEMS gyroscope dynamic models.

2- Eigenfunctions obtained by using the DMD method.

3- Koopman operator generated by using eigenfunctions obtained from the DMD method.

4- A LQR controller used to control created linear dynamics by Koopman theory.

5- The performance of the proposed method compares with conventional integral sliding mode control, in which the proposed controller has better performance.

5.2 Integral sliding mode control

A popular and reliable control technique is sliding mode control. Sliding Mode Control's primary benefits are strong tracking performance and robustness against external perturbations. In most works, sliding mode control has been used with a linear dynamic models of MEMS gyroscopes (Zhang, Shao, Zhao, Li, & Xu, 2018; Luo, Yang, Li, & Ouakad, 2022). We apply the Sliding Mode Control on the nonlinear MEMS gyroscope dynamic model. The main part of the sliding mode control design is how to select the sliding mode surfaces. The sliding mode surface defines as:

$$\boldsymbol{\eta} = \dot{\boldsymbol{e}} + \boldsymbol{\lambda} \int_{\mathbf{0}}^{\boldsymbol{t}} \boldsymbol{e}^{\frac{\boldsymbol{m}}{\boldsymbol{n}}} (\boldsymbol{\tau}) \boldsymbol{d\tau} \tag{5.1}$$

where $e=q$, m, n and $\boldsymbol{\lambda}$ is a positive constant. The equivalent control strategy is obtained when $\dot{\boldsymbol{\eta}} = \mathbf{0}$.

$$\dot{\boldsymbol{\eta}} = \ddot{\boldsymbol{e}} + \boldsymbol{\lambda} \boldsymbol{e}^{\frac{\boldsymbol{m}}{\boldsymbol{n}}} = \mathbf{0} \tag{5.2}$$

In equation (5.1), substituting the first and second derivatives from the error will result in the following.

$$\ddot{\boldsymbol{q}} + \boldsymbol{\lambda} \boldsymbol{q}^{\frac{\boldsymbol{m}}{\boldsymbol{n}}} = \mathbf{0} \tag{5.3}$$

Equation (3.10) is substituted with equation (5.2) to generate

$$-\boldsymbol{Y\dot{q} - Pq - \beta q^3 + u(t) + D(t) + \lambda q^{\frac{m}{n}} = 0} \tag{5.4}$$

The right side of the equation is introduced by moving all elements except *u(t)*.

$$\boldsymbol{u_{eq}(t) = Y\dot{q} + Pq + \beta q^3 - D(t) - \lambda q^{\frac{m}{n}}} \tag{5.6}$$

Equation (5.6) shows the equivalent controller. Uncertainties in the model and external disruptions cannot be compensated for by the equivalent control. To overcome these problems, a reaching control approach is introduced. The reaching control defines as:

$$\boldsymbol{u_r(t) = -K_r\eta} \tag{5.7}$$

where $\boldsymbol{K_r}$is the positive constant.

The control input defines:

$$\boldsymbol{u(t) = u_{eq}(t) + u_r(t)} \tag{5.8}$$

Sliding mode control is shown to be stable using the Lyapunov theory.

$$\boldsymbol{L(t) = \frac{1}{2}\,\eta\eta^T} \tag{5.9}$$

When the controller is stable, the following conditions are met:

$$\boldsymbol{\dot{L} = \eta^T\dot{\eta} < 0, \qquad \eta \neq 0} \tag{5.10}$$

Derivative from equation (5.9) yields

$$\boldsymbol{\dot{L} = \eta^T\dot{\eta}} \tag{5.11}$$

Substituting equation (5.11) with a derivative of the equation **(**5.9**)** results in

$$\dot{\boldsymbol{L}} = \boldsymbol{\eta}^{\boldsymbol{T}} \left(\ddot{\boldsymbol{e}} + \boldsymbol{\lambda} \boldsymbol{e}^{\frac{\boldsymbol{m}}{\boldsymbol{n}}} \right) \tag{5.12}$$

Equation **(**5.12**)** gave an illustration that

$$\dot{\boldsymbol{L}} = \boldsymbol{\eta}^{\boldsymbol{T}} \left(\ddot{\boldsymbol{q}} + \boldsymbol{\lambda} \boldsymbol{q}^{\frac{\boldsymbol{m}}{\boldsymbol{n}}} \right) \tag{5.13}$$

Equation **(**3.10**)** is substituted for equation **(**5.13**)** to introduce

$$\dot{\boldsymbol{L}} = \boldsymbol{\eta}^{\boldsymbol{T}} \left(-\boldsymbol{Y}\dot{\boldsymbol{q}} - \boldsymbol{P}\boldsymbol{q} - \boldsymbol{\beta}\boldsymbol{q}^{\boldsymbol{3}} + \boldsymbol{u}(\boldsymbol{t}) + \boldsymbol{D}(\boldsymbol{t}) + \boldsymbol{\lambda} \boldsymbol{q}^{\frac{\boldsymbol{m}}{\boldsymbol{n}}} \right) \tag{5.14}$$

Substitute equation **(**5.8**)** in the equation **(**5.14**)** produces

$$\dot{\boldsymbol{L}} = \boldsymbol{\eta}^{\boldsymbol{T}} \left(-\boldsymbol{Y}\dot{\boldsymbol{q}} - \boldsymbol{P}\boldsymbol{q} - \boldsymbol{\beta}\boldsymbol{q}^{\boldsymbol{3}} + \boldsymbol{u}_{\boldsymbol{eq}}(\boldsymbol{t}) + \boldsymbol{u}_{\boldsymbol{r}}(\boldsymbol{t}) + \boldsymbol{D}(\boldsymbol{t}) + \boldsymbol{\lambda} \boldsymbol{q}^{\frac{\boldsymbol{m}}{\boldsymbol{n}}} \right) \tag{5.15}$$

Using equation **(**5.6**)** in equation **(**5.15**)** shows

$$\dot{\boldsymbol{L}} = \boldsymbol{\eta}^{\boldsymbol{T}} \left(-\boldsymbol{Y}\dot{\boldsymbol{q}} - \boldsymbol{P}\boldsymbol{q} - \boldsymbol{\beta}\boldsymbol{q}^{\boldsymbol{3}} + \boldsymbol{Y}\dot{\boldsymbol{q}} + \boldsymbol{P}\boldsymbol{q} + \boldsymbol{\beta}\boldsymbol{q}^{\boldsymbol{3}} - \boldsymbol{D}(\boldsymbol{t}) - \boldsymbol{\lambda} \boldsymbol{q}^{\frac{\boldsymbol{m}}{\boldsymbol{n}}} \right. \tag{5.16}$$

$$\left. + \boldsymbol{u}_{\boldsymbol{r}}(\boldsymbol{t}) + \boldsymbol{D}(\boldsymbol{t}) + \boldsymbol{\lambda} \boldsymbol{q}^{\frac{\boldsymbol{m}}{\boldsymbol{n}}} \right)$$

Simplifying equation **(**5.16**)** results in

$$\dot{\boldsymbol{L}} = \boldsymbol{\eta}^{\boldsymbol{T}} \left(\boldsymbol{u}_{\boldsymbol{r}}(\boldsymbol{t}) \right) \tag{5.17}$$

Substitute equation (5.7) in equation (5.17) demonstrates

$$\dot{\boldsymbol{L}} = \boldsymbol{\eta}^{\boldsymbol{T}} (-\boldsymbol{K}_{\boldsymbol{r}} \boldsymbol{\eta}) = -\boldsymbol{K}_{\boldsymbol{r}} \boldsymbol{\eta}^{\boldsymbol{2}} \tag{5.18}$$

Equation (5.8) shows that $\dot{\boldsymbol{L}} < \mathbf{0}$. Therefore, the condition in equation (5.10) is satisfied and the controller is stable.

5.3 Koopman LQR control

One strategy for making the best control decisions is the LQR, which considers the states of the dynamical system and the control input (Prasad, Tyagi, & Gupta, 2014). The goal of the LQR design challenge is to create a state feedback controller that minimizes the objective function. Having a cost function that is based on equation (3.28) as

$$\boldsymbol{J} = \int_{\mathbf{0}}^{\infty} (\boldsymbol{y}^{\boldsymbol{T}}\boldsymbol{Q}\boldsymbol{y} + \boldsymbol{u}^{\boldsymbol{T}}\boldsymbol{R}\boldsymbol{u})\boldsymbol{dt} \tag{5.19}$$

where Q and R are the weight matrices (Anjali, Vivek, & Nandagopal, 2016). Following is the feedback control law that minimizes the cost function's value:

$$\boldsymbol{u} = -\boldsymbol{C}\boldsymbol{y} \tag{5.20}$$

where C defines as:

$$\boldsymbol{C} = \boldsymbol{R}^{-\mathbf{1}}\boldsymbol{B}^{\boldsymbol{T}}\boldsymbol{P} \tag{5.21}$$

By resolving the continuous time Riccati algebraic equation, P is obtained.

$$\boldsymbol{K}^{\boldsymbol{T}}\boldsymbol{P} + \boldsymbol{P}\boldsymbol{K} + \boldsymbol{Q} - \boldsymbol{P}\boldsymbol{B}\boldsymbol{R}^{-\mathbf{1}}\boldsymbol{B}^{\boldsymbol{T}}\boldsymbol{P} = \mathbf{0} \tag{5.22}$$

5.4 Simulation results

Simulation is done using the Matlab program. The fourth-order Runge-Kutta technique, known as the ode45 order in Matlab, is used. The integral terminal sliding mode (ITSMC) parameters are chosen as:

$\lambda=10$, $m=1.25$, $n=1.5$, and $K_r=11$.

The initial conditions for ITSMC selected as: $\boldsymbol{q_{0x}} = \mathbf{0.4}$, $\boldsymbol{q_{0y}} = \mathbf{0.6}$, $\dot{\boldsymbol{q}}_{\boldsymbol{0x}} = \mathbf{0}$, and $\dot{\boldsymbol{q}}_{\boldsymbol{0y}} = \mathbf{0}$.

The LQR control items are selected as:

$\boldsymbol{A} = \boldsymbol{K}$, $\boldsymbol{B} = \begin{bmatrix} \mathbf{0} & \mathbf{1} \\ \mathbf{1} & \mathbf{0} \end{bmatrix}$, $\boldsymbol{Q} = \begin{bmatrix} \mathbf{1} & \mathbf{0} \\ \mathbf{0} & \mathbf{1} \end{bmatrix}$, and $R=1$.

The nonlinear model of MEMS gyroscope is controlled by two control methods such as ITSMC and LQR controller linearized by Koopman theory (Koopman-LQR). Figure 5.1 shows the position tracking of x and y under Koopman-LQR and ITSMC. The Koopman-LQR controller has better performance in comparison with ITSMC in terms of high tracking performance and low settling time. The Koopman-LQR controller doesn't have any oscillation in comparison with ITSMC. It demonstrates that the proposed Koopman-LQR has better performance. Figure 5.2 shows the velocity of the x and the y axis under Koopman-LQR and ITSMC.

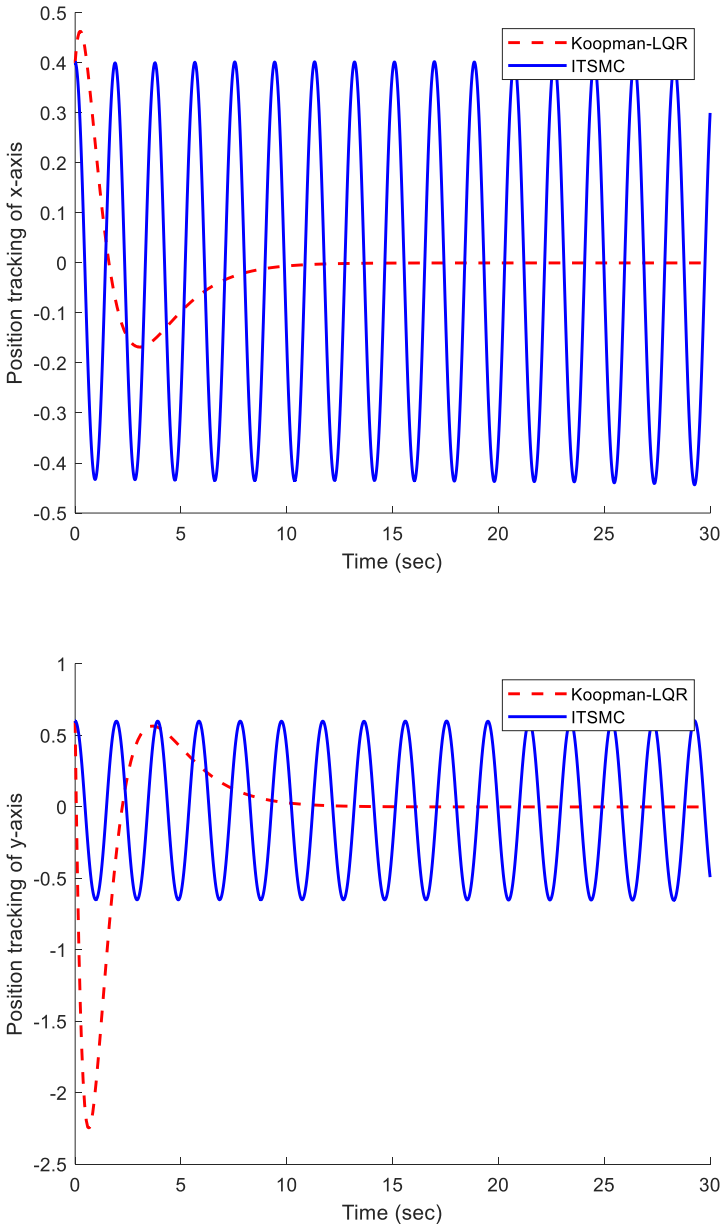

Figure 5.1: Position tracking of x and y axis under ITSMC and Koopman-LQR controllers.

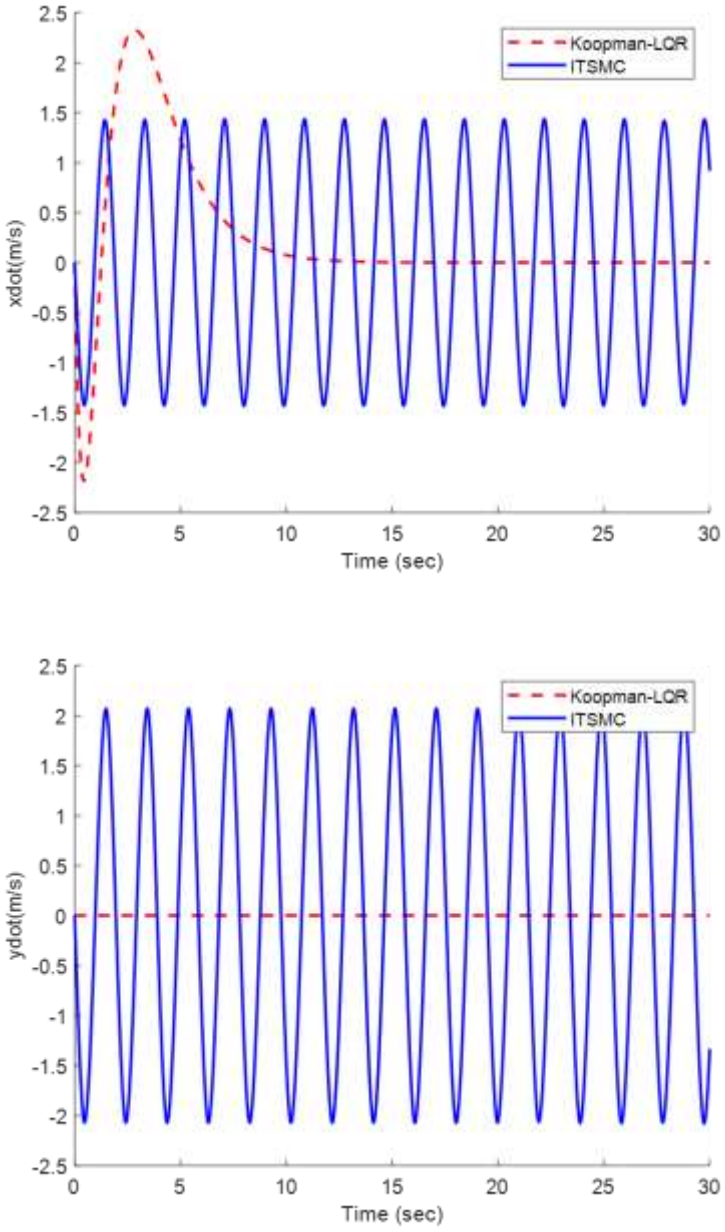

Figure 5.2: Velocity of x and y axis under ITSMC and Koopman-LQR controllers.

5.5 Conclusion

This research introduces Koopman-LQR and ITSMC for controlling a nonlinear dynamics of a MEMS gyroscope. First, a nonlinear dynamic model of MEMS gyroscope was introduced. Then, Koopman's theory was used to linearize the nonlinear dynamic of the MEMS gyroscope. The most important part was to calculate the Koopman operator. DMD method applied to estimate eigenfunction. An LQR controller is used to control the MEMS gyroscope system. The proposed Koopman-LQR method compared with ITSMC had better performance in terms of high tracking, low settling time, and zero oscillation. The effectiveness of the proposed Koopman-LQR method was verified by numerical simulation.

6 OPTIMAL DATA DRIVEN CONTROL OF A WORM ROBOT

6.1 Literature review

Bio-inspired robots are robots that inspired the animal's motion and structure in nature. The scholar detects the animals that are available in nature and changes their motion characteristics to a mechanism that is used as a robot. The worm robot is one of these structures in which its motion mimics the worm in nature. This robot has many applications such as medicine and rescue plans (Henson & Marais, (2012, November); Zarrouk, Sharf, & Shoham, 2012; Liu, et al., 2022; Ortiz, Gravish, & Tolley, 2019; Onal, Wood, & Rus, 2012). The worm robot passes through harsh environments. Control of that type of robot is a challenging task.

Several control methods are used to control the worm robot in the desired trajectory. A robust adaptive controller is proposed in (Rahmani, Ghanbari, & Ettefagh, Robust adaptive control of a bio-inspired robot manipulator using bat algorithm, 2016). The proposed control method contained compound control methods. First, the sliding mode control is used for the robustness of the control method against external disturbances. Then, a compound fractional proportional integral derivative controller is used to improve tracking performance. A bat algorithm is used to tune the proposed controller parameters. A control method demonstrates that friction is essential to the creation and control of

locomotion in this sort of robot by using the concept of controlled subspace (Joey, Calderón, Chang, & Pérez-Arancibia, 2019). They present a simulation-based technique for generating and executing feedback control schemes that let the robot produce forward and backward locomotion based on this analysis. The other types of controllers used to control a worm robot such as hybrid neural network integral sliding mode control (Rahmani, Ghanbari, & Ettefagh, Hybrid neural network fraction integral terminal sliding mode control of an Inchworm robot manipulator, 2016) and neural central pattern generator (Wang, Zhang, Zhang, & Wang, (2018, May)). However, the mentioned controllers worked on model-based control methods or used artificial intelligence to control worm robots, but they didn't use data-driven controllers. The Koopman theory is a strong data-driven method to control the robot. In complicated nonlinear dynamic systems, the Koopman operator is a powerful tool. This theory will control nonlinear dynamic systems with high dimensional nonlinearity using a data-driven approach (Abraham & Murphey, 2019). In (Bruder, Fu, Gillespie, Remy, & Vasudevan, 2020), a Koopman-based system identification technique is described along with how it may be used to create model predictive controls for soft robots. Through the use of the Koopman-based methodology, three model predictive controllers are created for a pneumatic soft robot arm, and their performance is evaluated on several actual trajectory-following tasks. These Koopman-based controllers have an average tracking error that is more than three times lower than a

benchmark model predictive controller built on a linear state-space model of the same system, proving the effectiveness of the Koopman technique in soft robot control.

The LQR control method is a strong optimal control method that can improve trajectory tracking and provide more stability. The dynamics of the system are considered to be unknown in this study of the finite-horizon linear quadratic regulation issue (Rotulo, De Persis, & Tesi, 2020). A limited number of input-state variables can provide information about the system, provided that the input is continually stimulating and of a high enough order. The best control law is then discovered by solving an appropriate semidefinite program using data. The neural network is used to generate the Koopman operator (Shi & Meng, 2022). Then, the Koopman theory was used in developing a linear dynamic model of the 7 degrees of freedom (DoF) of robot manipulators. An LQR controller was applied to reduce the tracking error.

How the Koopman operator is designed is the most critical aspect of employing the Koopman operator. To get the Koopman operator, other techniques may be utilized, including the neural networks (Shi & Meng, 2022) (Schulze, Doncevic, & Mitsos, 2022) and DMD approach (Mansour, Benosman, & Huroyan, (2017, July)).

The contributions of this research are categorized as:

1- An optimal data-driven controller is applied to control a worm robot.

2- The nonlinear dynamics of a worm robot are introduced.

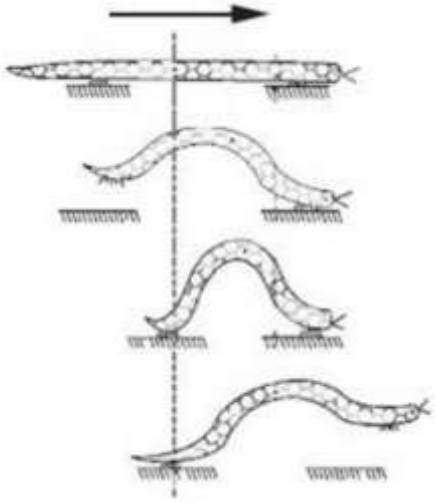

Figure 6.1: Worm robot motion in nature.

3- The Koopman theory is used to linearize the nonlinear dynamic model of the worm robot.

4- The DMD method is used to generate the Koopman operator.

5- An LQR controller is used to control the linearized dynamic model of the worm robot.

6.2 Worm robot structure

The worm robot is inspired by the motion of the worm in nature. Figure 6.1 shows a worm motion in nature. Therefore, if the motion changes to a mechanism, the robot will be created. The motion of the worm can be demonstrated as a mechanism in Figure 6.2.

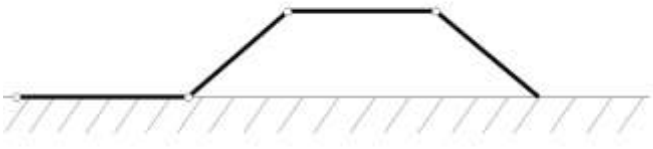

Figure 6.2: Worm robot mechanism.

The Scholars obtained the nonlinear dynamics equations of the mechanism in Figure 6.2 (Ghanbari & Noorani, 2011):

$$\boldsymbol{M(\theta)\ddot{\theta} + V(\theta)\dot{\theta}^2 + G(\theta) = K\tau + \lambda F_R} \tag{6.1}$$

where $\boldsymbol{M(\theta) \in R^{4\times4}}$, $\boldsymbol{V(\theta) \in R^{4\times4}}$, $\boldsymbol{G(\theta) \in R^{4\times1}}$, and $\boldsymbol{K \in R^{4\times1}}$are mass matrix, centrifugal coefficient matrix, gravity vector, and subtraction matrix. Also, the $\boldsymbol{F_R}$is forces that apply from the ground. The detailed process of obtaining the equation (6.1) can be observed in

$$\boldsymbol{M(\theta) = \frac{ml^2}{6}\begin{bmatrix} 20 & 15c_{12} & 9c_{13} & 3c_{14} \\ 15c_{12} & 14 & 9c_{23} & 3c_{24} \\ 9c_{13} & 9c_{23} & 8 & 3c_{34} \\ 3c_{14} & 3c_{24} & 3c_{34} & 2 \end{bmatrix}}$$

$$\boldsymbol{V(\theta)} = \frac{\boldsymbol{ml^2}}{\boldsymbol{6}}\begin{bmatrix} \boldsymbol{0} & \boldsymbol{15s_{12}} & \boldsymbol{9s_{13}} & \boldsymbol{3s_{14}} \\ \boldsymbol{-15s_{12}} & \boldsymbol{0} & \boldsymbol{9s_{23}} & \boldsymbol{3s_{24}} \\ \boldsymbol{-9s_{13}} & \boldsymbol{-9s_{23}} & \boldsymbol{0} & \boldsymbol{3s_{34}} \\ \boldsymbol{-3s_{14}} & \boldsymbol{-3s_{24}} & \boldsymbol{-3s_{34}} & \boldsymbol{0} \end{bmatrix}$$

$$\boldsymbol{G(\theta)} = \frac{\boldsymbol{mgl}}{\boldsymbol{2}}\begin{bmatrix} \boldsymbol{7cos\theta_1} \\ \boldsymbol{5cos\theta_2} \\ \boldsymbol{3cos\theta_3} \\ \boldsymbol{cos\theta_4} \end{bmatrix}$$

$$\boldsymbol{\lambda} = \begin{bmatrix} \boldsymbol{1} & \boldsymbol{-1} & \boldsymbol{0} & \boldsymbol{0} \\ \boldsymbol{0} & \boldsymbol{1} & \boldsymbol{-1} & \boldsymbol{0} \\ \boldsymbol{0} & \boldsymbol{0} & \boldsymbol{1} & \boldsymbol{-1} \\ \boldsymbol{0} & \boldsymbol{0} & \boldsymbol{0} & \boldsymbol{1} \end{bmatrix}$$

where $\boldsymbol{\theta_i}$ is the angle of i^{th} joint. Also, $\boldsymbol{c_{ij}} = \boldsymbol{\cos}\left(\boldsymbol{\theta_i} - \boldsymbol{\theta_j}\right)$ and $\boldsymbol{s_{ij}} = \boldsymbol{\sin}\ (\boldsymbol{\theta_i} - \boldsymbol{\theta_j})$. The *m* is mass of each link and *l* is length of each link.

6.3 Koopman Theory

The Koopman operator theory states that in order to successfully solve a nonlinear dynamical system, the nonlinear system's initial form must be converted into an infinite dimensional state space, resulting in a linear system (Ping, Yin, Li, Liu, & Yang, 2021).

The dynamic in discrete time defines as (Kaiser, Kutz, & Brunton, 2021):

$$\boldsymbol{z_{k+1}} = \boldsymbol{F(z_k)} \tag{6.2}$$

where F is defined as

$$\boldsymbol{F}\big(\boldsymbol{z}(\boldsymbol{t_0})\big) = \boldsymbol{z}(\boldsymbol{t_0}) + \int_{\boldsymbol{t_0}}^{\boldsymbol{t_0+t}} \boldsymbol{f}\big(\boldsymbol{z}(\boldsymbol{\tau})\big)\boldsymbol{d\tau} \tag{6.3}$$

The Koopman operator theoretic technique transforms a finite-dimensional nonlinear system's dynamics into linearity when applied to infinite-dimensional function space. In an infinite-dimensional Hilbert space, g is an observable and a real-valued scalar measurement function. Based on this observable, the Koopman operator generates as follows:

$$\boldsymbol{Kg} = \boldsymbol{g} \circ \boldsymbol{F} \tag{6.4}$$

A continuous system can be utilized to implement smooth dynamics.

$$\frac{\boldsymbol{d}}{\boldsymbol{dt}}\boldsymbol{g}(\boldsymbol{z}) = \boldsymbol{Kg}(\boldsymbol{z}) = \boldsymbol{\nabla g}(\boldsymbol{z}).\boldsymbol{f}(\boldsymbol{z}) \tag{6.5}$$

where *K* is Koopman's operator. Due to the Koopman operator's infinite dimensions, which is important yet troublesome for operation and representation. Applied Koopman analysis approximates the evolution of a subspace covered by a few measurement functions as opposed to describing the growth of all measurement functions in a Hilbert space. By limiting the Koopman operator to an invariant subspace, one may obtain a representation of the operator in a finite-dimensional matrix. Any combination of the Koopman operator's eigenfunctions covers a Koopman invariant subspace. When

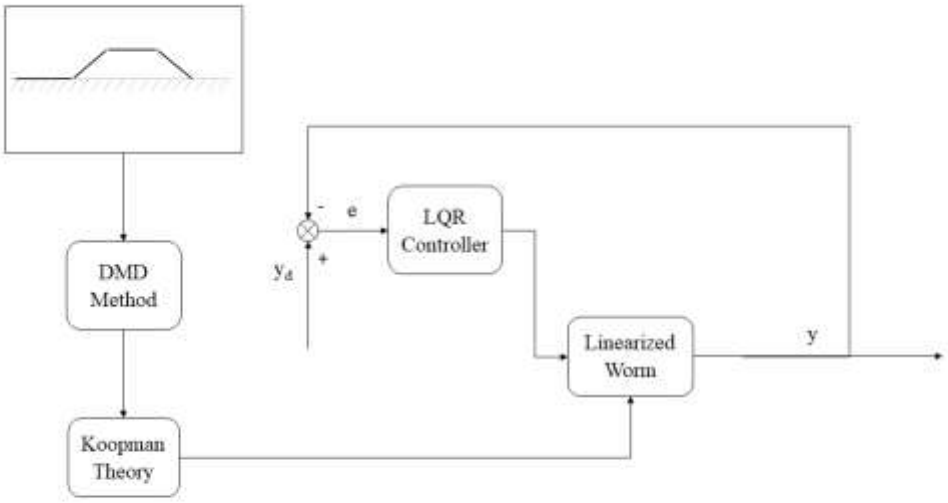

Figure 6.3: The proposed control method diagram.

eigenfunction $\boldsymbol{\varphi(z)}$ of the Koopman model meets eigenvalue λ (Kaiser, Kutz, & Brunton, 2021). The proposed control method block diagram is shown in Figure 6.3.

$$\boldsymbol{\lambda\varphi(z) = \varphi\big(F(z)\big)} \tag{6.6}$$

A Koopman eigenfunction (z) is satisfied in continuous time.

$$\boldsymbol{\frac{d}{dt}\varphi(z) = \lambda\varphi(z)} \tag{6.7}$$

To approximate the Koopman operator, an application-side finite-dimensional approximation is needed. One method for estimating the Koopman operator is the DMD method.

6.4 DMD method

The DMD method is a strong approach that is used to approximate the Koopman operator.

$$\boldsymbol{Z'} \approx \boldsymbol{AZ} \tag{6.8}$$

where $\boldsymbol{Z'}$ is time shift of matrix Z as

$$\boldsymbol{Z} = [\boldsymbol{z_1} \quad \boldsymbol{z_2} \quad \dots\dots]$$

The A may be determined as follows using equation (6.8):

$$\boldsymbol{A} = \boldsymbol{Z'Z^{+}} \tag{6.9}$$

where + represents the Moore-Penrose pseudoinverse. In order to find the dominant characteristics of the pseudoinverse of *Z*, we may utilize Singular Value Decomposition (SVD) on the snapshots. This is because a conventional calculation utilizing A would need a substantial amount of computation because of the large *n* (Snyder & Song, 2021).

$$\boldsymbol{Z} \approx \boldsymbol{U\Sigma V^{*}} \tag{6.10}$$

where $\boldsymbol{U} \in \boldsymbol{R}^{\boldsymbol{n}\times\boldsymbol{r}}$, $\boldsymbol{\Sigma} \in \boldsymbol{R}^{\boldsymbol{r}\times\boldsymbol{r}}$, $\boldsymbol{V} \in \boldsymbol{R}^{\boldsymbol{n}\times\boldsymbol{r}}$, and $*$ demonstrates the conjugate transpose. SVD's reduced rank for approximating Z is r. The eigenvectors can be defined as:

$$\Phi = \boldsymbol{Z'V\Sigma^{-1}}\mathrm{W} \tag{6.11}$$

where W denotes the eigenvectors of the dynamic complete rank system.

$$\Phi = \boldsymbol{Z'V\Sigma^{-1}}\mathrm{W} \tag{6.12}$$

If we assume that λ is the eigenfunction, then we get:

$$\boldsymbol{KW} = \boldsymbol{\lambda W} \tag{6.13}$$

where K is the Koopman operator.

The demonstration of the linearized dynamic model is as follows:

$$\frac{\boldsymbol{d}}{\boldsymbol{dt}}\boldsymbol{y} = \boldsymbol{Ky} + \boldsymbol{Bu} \tag{6.14}$$

6.5 LQR control method

The LQR, which takes into account the states of the dynamical system and the control input, is one method for determining the optimum control decisions (Prasad, Tyagi, & Gupta, 2014).

Making a state feedback controller that minimizes the target function is the aim of the LQR design challenge. The cost function is defined as:

$$\boldsymbol{J = \int_0^{\infty} (y^T Q y + u^T R u) dt} \tag{6.15}$$

where Q and R are the weight matrices. The feedback control law that reduces the value of the cost function is as follows.

$$\boldsymbol{u = -Cy} \tag{6.16}$$

where C denotes as:

$$\boldsymbol{C = R^{-1} B^T P} \tag{6.17}$$

P is found by solving the continuous time Riccati algebraic problem.

$$\boldsymbol{K^T P + PK + Q - PBR^{-1} B^T P = 0} \tag{6.18}$$

6.6 Simulation results

The simulation is done in MATLAB software. Some data was generated from the nonlinear dynamic model of the worm robot. Then, the data were categorized by the DMD method to obtain the Koopman operator. The Koopman operator was used to estimate the linear dynamic model of the worm robot. Finally, the LQR controller is applied to the worm robot to control it suitably.

The initial values of angular velocity are all zeros. The initial position of the joints is as follows

$$\boldsymbol{\theta_0 = \left\{\frac{\pi}{4}, \frac{\pi}{2}, 0, 0\right\}}$$

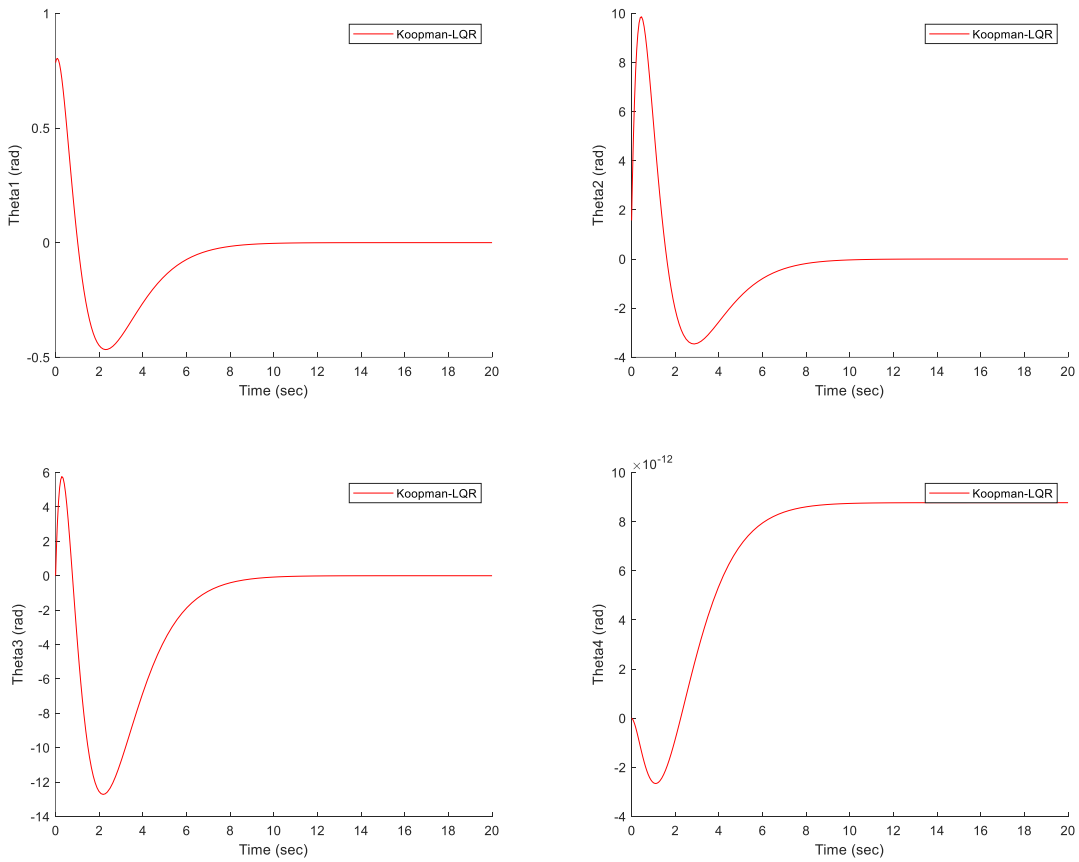

Figure 6.4: The position tracking of the worm robot joints under the proposed controller.

The mass of each link is equal to 1 and the length is equal to 1 too.

Figure 6.4 shows the position tracking of joints under the LQR controller linearized by the Koopman theory (Koopman-LQR). It shows that the proposed control method has suitable tracking performance.

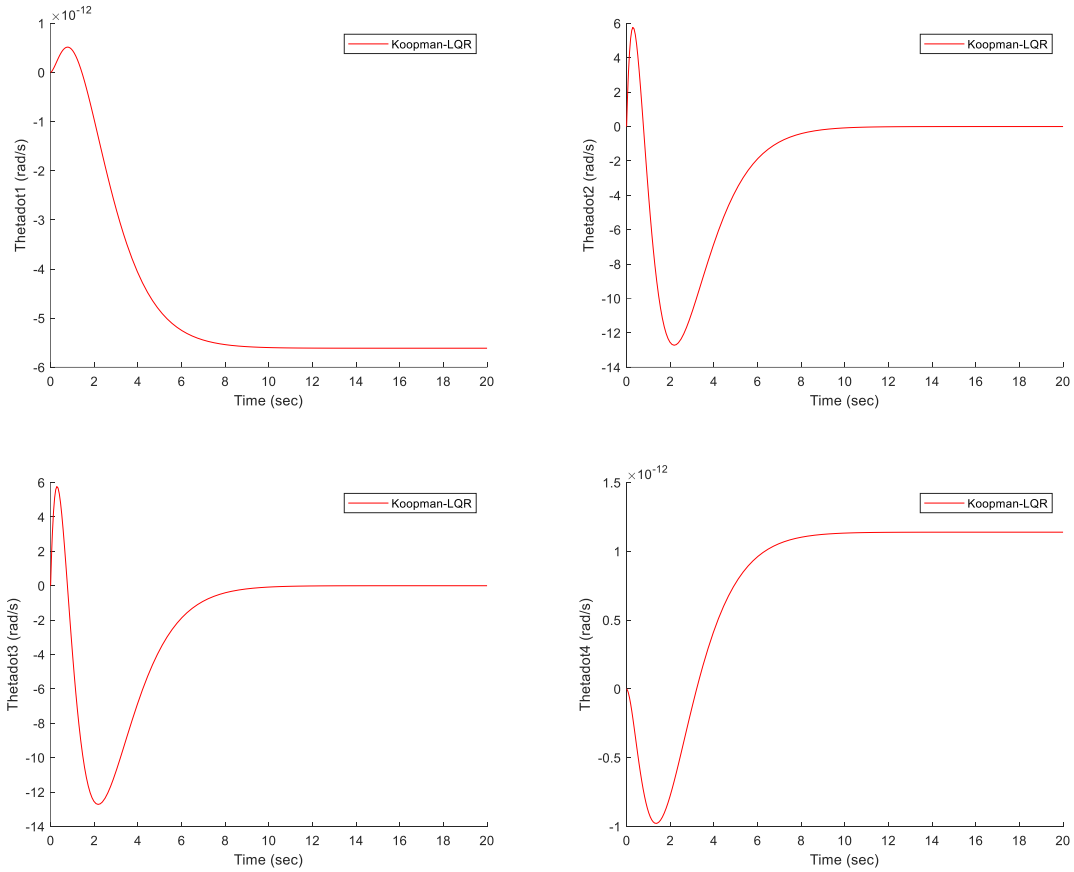

Figure 6.5: The velocity of the worm robot joints under the proposed controller

The maximum overshoot for the Theta1 is around 46 percent which illustrates that the design is good.

Figure 6.5 shows the velocity of the robot joints under the Koopman-LQR controller.

6.7 Conclusion

This research proposed an optimal data-driven control of a worm robot. The nonlinear dynamic model of a worm robot is discussed in this research. The Koopman theory was applied to linearize the nonlinear dynamics of the worm robot. The DMD method was used to estimate the Koopman operator. An LQR controller is used to control the worm robot joints. The simulation results verified the performance of the proposed controller under the Koopman-LQR controller.

7 ROBOT MANIPULATOR CONTROL USING A ROBUST DATA-DRIVEN METHOD

7.1 Literature review

Robotic manipulators are highly used in different industries such as the automotive and medical industries. These highly demanded robots were implemented in some conditions where they encountered external disturbances. Therefore, designing a suitable control method is the most important part of the robotics design process. There are many control methods applied to robot manipulators to control them in the desired trajectory such as PID controller (Cervantes & Alvarez-Ramirez, 2001) (Su, Müller, & Zheng, Global asymptotic saturated PID control for robot manipulators, 2009) (Kelly, 1995) (Kumar & Amutha, (2014, December)), sliding mode control (Ahmad & Osman, (2003, August).) (Piltan & Sulaiman, 2012) (Islam & Liu, 2010), fuzzy PID control (Anavatti, Salman, & Choi, (2006, December)) (Sharma, Rana, & Kumar, 2014) (Ravari & Taghirad, (2009, February)), etc. The mentioned control methods depended on the dynamic model of the robot manipulator. However, designing the mentioned control methods mostly requires an accurate dynamic model, which will not provide the accurate performance of the proposed control method. The data-driven methods are some strong approaches that can approximate the dynamic model to generate accurate model characteristics.

Carron et al. (2019) provide a model-based control method that uses information acquired from actual operations to enhance the model of the robotic arm and the tracking performance. Inverse dynamics feedback linearization and a data-driven error model are the foundations of the suggested approach, which is incorporated into a formulation for model predictive control. Also, they demonstrated how adding a Gaussian process to a nominal model can enable offset-free tracking. To achieve trajectory tracking control of the manipulator, the Gauss process feedback linearization approach based on the updating of the event-triggered model is used in a manipulator system with three degrees of freedom (Wang Y. , Data-driven trajectory tracking of manipulator with event-triggered model updating, (2020, August)). And to address the issue of extensive Gaussian process regression computation under big data samples, sparse Gaussian process regression is utilized for real-time manipulator trajectory tracking.

The Koopman theory is a strong method for data-driven-based control methods. It can linearize the complex nonlinear dynamic model. Several researchers use the Koopman theory in their research to provide better control performance (Goswami & Paley, Bilinearization, reachability, and optimal control of control-affine nonlinear systems: A Koopman spectral approach, 2021) (Shi & Meng, 2022) (Calderón, Schulz, Oehlschlägel, & Werner, (2021, June)) (Husham, Kamwa, Abido, & Suprême, 2022) (Narasingam, Son, & Kwon, 2022). However, the most important part of the Koopman theory application is

how to design the Koopman operator. The DMD method is one of the useful techniques that can be used to generate the Koopman operator. Extended Dynamic Mode Decomposition (EDMD), a technique invented in (Junker, Timmermann, & Trächtler, (2022, May)), approximates a nonlinear dynamical system as a linear model. Due to the common usage of a linear system description in control engineering applications, this technique is excellent for these applications. They simulatively analyze the prediction performance of the learned EDMD models using academic examples, demonstrating how important system properties like stability, controllability, and observability are reflected by the EDMD model, which is a crucial prerequisite for a successful control design process. They then display the experimental findings on a mechatronic test bench and assess how well they apply to the control engineering design procedure. For a variety of data-driven Koopman operator-based nonlinear robotic systems, Shi and Karydis (2021) suggest ACD-EDMD, a novel approach for the Analytical Construction of Dictionaries of Appropriate Lifting Functions. The main finding of this study is that Hermite polynomial-based lifting functions may be constructed by using knowledge of the basic topological spaces of the nonlinear system. When observables are weighted bounded, they demonstrate that the suggested approach produces dictionaries with proven completeness and convergence guarantees that are easy to implement. Various nonlinear robotic systems from both simulated and real hardware experiments are used to assess ACD-EDMD. To get over this

restriction and retrieve the leading Koopman eigenvalues, eigenfunctions, and modes of the unforced system, Williams et al. (2016) describe a version of EDMD. This modification accounts for the effects of actuation. The Duffing oscillator and a lattice Boltzmann code that approximates the FitzHugh-Nagumo partial differential equation and displays Koopman mode and eigenvalue computation, respectively, are used as two examples with (quasi)-periodic forcing to illustrate the effectiveness of this method.

The contributions of this research are as follows:

1- The Koopman theory is applied to linearize the nonlinear dynamics of the 2 DoF robot manipulator.

2- The DMD method is applied to obtain the Koopman operator.

3- A fractional sliding mode control is proposed to control the linearized dynamics model by Koopman's theory.

4- The conventional PID and FOSMC are implemented to verify the performance of the proposed control method.

7.2 Dynamic model of 2 DoF robot manipulator

Robots can boost output, effectiveness, product uniformity, and quality in a variety of circumstances: Robots, unlike people, never get bored. They may keep doing the same thing repeatedly until they wear out. The robot manipulator can be used in many applications such as exoskeletons robot (Rahmani & Rahman, Adaptive neural network

fast fractional sliding mode control of a 7-DOF exoskeleton robot, 2020) and refueling robots (Sun, Yin, Wang, & Xu, 2018).

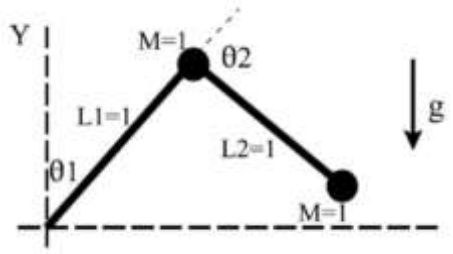

Figure 7.1: Two degrees of freedom robot manipulator structure.

The following is an example of a 2-DOF robot manipulator's dynamic modeling (Jin, Lee, Chang, & Choi, 2009):

$$\boldsymbol{M}(\boldsymbol{q})\ddot{\boldsymbol{q}} + \boldsymbol{N}(\boldsymbol{q}, \dot{\boldsymbol{q}})\dot{\boldsymbol{q}} + \boldsymbol{G}(\boldsymbol{q}) = \boldsymbol{\tau} \tag{7.1}$$

where $\boldsymbol{q}, \dot{\boldsymbol{q}}, \ddot{\boldsymbol{q}} \in \boldsymbol{R^2}$ represent the position, velocity, and acceleration of the joints, respectively, and $\boldsymbol{M}(\boldsymbol{q}) \in \boldsymbol{R^{2\times2}}$ known as the generalized inertia matrix, $\boldsymbol{N}(\boldsymbol{q}, \dot{\boldsymbol{q}}) \in \boldsymbol{R^{2\times2}}$ is the vector of Coriolis and centrifugal forces, $\boldsymbol{G}(\boldsymbol{q}) \in \boldsymbol{R^{2\times1}}$ the gravitational vector, and $\boldsymbol{\tau} \in \boldsymbol{R^{2\times1}}$ the joint torques. $\boldsymbol{M}(\boldsymbol{q})$, $\boldsymbol{N}(\boldsymbol{q}, \dot{\boldsymbol{q}})$ and $\boldsymbol{G}(\boldsymbol{q})$ are given as

$$\boldsymbol{q} = \begin{bmatrix} \boldsymbol{\theta_1} \\ \boldsymbol{\theta_2} \end{bmatrix}$$

$$\boldsymbol{M}(\boldsymbol{q}) = \begin{bmatrix} (\boldsymbol{M_1} + \boldsymbol{M_2})\boldsymbol{L_1^2} + \boldsymbol{M_2 L_2^2} + \boldsymbol{2M_2 L_1 L_2 cos\theta_2} & \boldsymbol{M_2 L_2^2} + \boldsymbol{M_2 L_1 L_2 cos\theta_2} \\ \boldsymbol{M_2 L_2^2} + \boldsymbol{M_2 L_1 L_2 cos\theta_2} & \boldsymbol{M_2 L_2^2} \end{bmatrix}$$

$$\boldsymbol{N(q)} = \begin{bmatrix} \boldsymbol{-M_2 L_1 L_2 sin\theta_2 (2\dot{\theta}_1 \dot{\theta}_2 + \dot{\theta}_2^2)} \\ \boldsymbol{-M_2 L_1 L_2 sin\theta_2 \dot{\theta}_1 \dot{\theta}_2} \end{bmatrix}$$

$$\boldsymbol{G(q)} = \begin{bmatrix} \boldsymbol{-(M_1 + M_2) g L_1 sin\theta_1 - M_2 g L_2 \sin(\theta_1 + \theta_2)} \\ \boldsymbol{-M_2 g L_2 \sin(\theta_1 + \theta_2)} \end{bmatrix}$$

$$\boldsymbol{\tau} = \begin{bmatrix} \boldsymbol{\tau_1} \\ \boldsymbol{\tau_2} \end{bmatrix}$$

Equation (7.1) can be defined as:

$$\boldsymbol{\ddot{q}} = \boldsymbol{-M^{-1}(q) N(q, \dot{q}) \dot{q} - M^{-1}(q) G(q)} + M^{-1}(q)\tau \tag{7.2}$$

The 2DoF robot manipulator structure is shown in Figure 7.1. It is possible to rearrange the dynamic equation for a 2-DOF robot manipulator as follows:

$$\boldsymbol{\ddot{q} = -B\dot{q} - CG(q) + u} \tag{7.3}$$

where $\boldsymbol{B = M^{-1}(q) N(q, \dot{q})}$, $\boldsymbol{C = M^{-1}(q)}$, and $\boldsymbol{u = M^{-1}(q)\tau}$. The definition of equation (7.4) where $\boldsymbol{\Delta B}$ and $\boldsymbol{\Delta C}$ are uncertainty symbols is

$$\boldsymbol{\ddot{q} = -(B + \Delta B)\dot{q} - (C + \Delta C) G(q) + u} \tag{7.4}$$

The equation (7.4) can be introduced as:

$$\boldsymbol{\ddot{q} = -B\dot{q} - CG(q) + u + d(t)} \tag{7.5}$$

where $\boldsymbol{d(t) = -\Delta B\dot{q} - CG(q)}$.

7.3 PID control method

The PID controller has been highly used in industrial companies due to its ease of implementation and low cost. The PID controller can be defined as:

$$\boldsymbol{u_{PID} = K_p e(t) + K_i \int_0^t e(\tau) d\tau + K_d \frac{de(t)}{dt}} \quad (7.6)$$

where $\boldsymbol{K_p, K_i, K_d}$ are proportional, integral, and derivative parameters. Also, the tracking error can be defined as:

$$\boldsymbol{e(t) = q_d - q} \quad (7.7)$$

where $\boldsymbol{q_d}$ is desired trajectory tracking. The main drawbacks of the PID controller are that it is not robust against external disturbances and has low trajectory tracking.

7.4 Fractional order sliding mode control

The FOSMC is a robust control method against external perturbations and has high tracking performance. The main advantage of this control method in comparison with conventional sliding mode control is that we can have a fraction derivative or integral of the error. The main part of FOSMC design is choosing the fractional sliding mode surface as:

$$\boldsymbol{s(t) = \dot{e}(t) + \alpha D^{\mu} e(t) + \beta D^{-\mu} e(t)} \quad (7.8)$$

Where $\boldsymbol{\alpha}$ and $\boldsymbol{\beta}$ are positive constants and D is the Grunwald-Letnikov fractional operator.

The FOSMC contains two control sections: equivalent control and reaching control law. The equivalent control method can be obtained by equaling the derivative of the sliding mode surface to zero. Take the derivative from equation (7.8) results:

$$\dot{\boldsymbol{s}}(\boldsymbol{t}) = \ddot{\boldsymbol{e}}(\boldsymbol{t}) + \boldsymbol{\alpha\mu D^{\mu+1}e(t)} - \boldsymbol{\beta\mu D^{-\mu+1}e(t)} \quad (7.9)$$

Take the double derivative from equation (7.7) and substitute it into equation (7.9) produces

$$\dot{\boldsymbol{s}}(\boldsymbol{t}) = \ddot{\boldsymbol{q}}_{\boldsymbol{d}} - \ddot{\boldsymbol{q}} + \boldsymbol{\alpha\mu D^{\mu+1}e(t)} - \boldsymbol{\beta\mu D^{-\mu+1}e(t)} \quad (7.10)$$

Substitute equation (7.5) into equation (7.10) generates

$$\dot{\boldsymbol{s}}(\boldsymbol{t}) = \ddot{\boldsymbol{q}}_{\boldsymbol{d}} + \boldsymbol{B\dot{q}} + \boldsymbol{CG(q)} - \boldsymbol{u} - \boldsymbol{d(t)} + \boldsymbol{\alpha\mu D^{\mu+1}e(t)} - \boldsymbol{\beta\mu D^{-\mu+1}e(t)} \quad (7.11)$$

By equaling the equation (7.11) and *d(t)* to zero, the equivalent control can be obtained as:

$$\boldsymbol{u_{eq}} = \ddot{\boldsymbol{q}}_{\boldsymbol{d}} + \boldsymbol{B\dot{q}} + \boldsymbol{CG(q)} + \boldsymbol{\alpha\mu D^{\mu+1}e(t)} - \boldsymbol{\beta\mu D^{-\mu+1}e(t)} \quad (7.12)$$

The equivalent control solely is not able to suppress the external disturbances. Therefore, a reaching control law will be implemented to solve that problem. The reaching control law introduces as:

$$\boldsymbol{u_r} = \boldsymbol{K_r s(t)} \quad (7.13)$$

Therefore, the FOSMC defines as:

$$\boldsymbol{u_{FOSMC}(t)} = \boldsymbol{u_{eq}(t)} + \boldsymbol{u_r(t)} \quad (7.14)$$

The proposed control method's stability can be proved by using the Lyapunov theory as

$$\boldsymbol{V(t)} = \frac{\boldsymbol{1}}{\boldsymbol{2}}\boldsymbol{s^T(t)s(t)} \quad (7.15)$$

The condition for stability satisfaction is as follows:

$$\dot{\boldsymbol{V}}(\boldsymbol{t}) = \boldsymbol{s}^{\boldsymbol{T}}(\boldsymbol{t})\dot{\boldsymbol{s}}(\boldsymbol{t}) < \boldsymbol{0} \tag{7.16}$$

Substitute equation (7.11) into equation (7.16) produces

$$\dot{\boldsymbol{V}}(\boldsymbol{t}) = \boldsymbol{s}^{\boldsymbol{T}}(\boldsymbol{t})(\ddot{\boldsymbol{q}}_{\boldsymbol{d}} + \boldsymbol{B}\dot{\boldsymbol{q}} + \boldsymbol{CG}(\boldsymbol{q}) - \boldsymbol{u} + \boldsymbol{\alpha\mu D}^{\boldsymbol{\mu+1}}\boldsymbol{e}(\boldsymbol{t}) - \boldsymbol{\beta\mu D}^{-\boldsymbol{\mu+1}}\boldsymbol{e}(\boldsymbol{t})) \tag{7.17}$$

Substitute equation (7.14) into equation (7.17) introduces

$$\dot{\boldsymbol{V}}(\boldsymbol{t}) = \boldsymbol{s}^{\boldsymbol{T}}(\boldsymbol{t})(\ddot{\boldsymbol{q}}_{\boldsymbol{d}} + \boldsymbol{B}\dot{\boldsymbol{q}} + \boldsymbol{CG}(\boldsymbol{q}) - \boldsymbol{u}_{\boldsymbol{eq}}(\boldsymbol{t}) - \boldsymbol{u}_{\boldsymbol{r}}(\boldsymbol{t}) + \boldsymbol{\alpha\mu D}^{\boldsymbol{\mu+1}}\boldsymbol{e}(\boldsymbol{t}) - \boldsymbol{\beta\mu D}^{-\boldsymbol{\mu+1}}\boldsymbol{e}(\boldsymbol{t})) \tag{7.18}$$

Substitute equation (7.12) into equation (7.18) results

$$\dot{\boldsymbol{V}}(\boldsymbol{t}) = \boldsymbol{s}^{\boldsymbol{T}}(\boldsymbol{t})(\ddot{\boldsymbol{q}}_{\boldsymbol{d}} + \boldsymbol{B}\dot{\boldsymbol{q}} + \boldsymbol{CG}(\boldsymbol{q}) - \ddot{\boldsymbol{q}}_{\boldsymbol{d}} - \boldsymbol{B}\dot{\boldsymbol{q}} - \boldsymbol{CG}(\boldsymbol{q}) - \boldsymbol{\alpha\mu D}^{\boldsymbol{\mu+1}}\boldsymbol{e}(\boldsymbol{t}) + \boldsymbol{\beta\mu D}^{-\boldsymbol{\mu+1}}\boldsymbol{e}(\boldsymbol{t}) - \boldsymbol{u}_{\boldsymbol{r}}(\boldsymbol{t}) + \boldsymbol{\alpha\mu D}^{\boldsymbol{\mu+1}}\boldsymbol{e}(\boldsymbol{t}) - \boldsymbol{\beta\mu D}^{-\boldsymbol{\mu+1}}\boldsymbol{e}(\boldsymbol{t})) \tag{7.19}$$

Simplify equation (7.19) demonstrates

$$\dot{\boldsymbol{V}}(\boldsymbol{t}) = \boldsymbol{s}^{\boldsymbol{T}}(\boldsymbol{t})(-\boldsymbol{u}_{\boldsymbol{r}}(\boldsymbol{t})) \tag{7.20}$$

Substitute equation (7.13) into equation (7.20) produces

$$\dot{\boldsymbol{V}}(\boldsymbol{t}) = \boldsymbol{s}^{\boldsymbol{T}}(\boldsymbol{t})(-\boldsymbol{K}_{\boldsymbol{r}}\boldsymbol{s}(\boldsymbol{t})) \tag{7.21}$$

Equation (7.21) satisfies the condition in equation (7.16). Therefore, the proposed controller is stable.

7.5 Koopman theory

The key to successfully solving a nonlinear dynamical system, according to the Koopman operator theory, is to convert the nonlinear system's original form into an infinite dimensional state space, resulting in a linear system (Ping, Yin, Li, Liu, & Yang, 2021).

The discrete-time definition of the dynamic is (Kaiser, Kutz, & Brunton, 2021):

$$\boldsymbol{x_{k+1} = F(x_k)} \tag{7.22}$$

where F is characterized by

$$\boldsymbol{F\big(x(t_0)\big) = x(t_0) + \int_{t_0}^{t_0+t} f\big(x(\tau)\big)d\tau} \tag{7.23}$$

The dynamics of the original system become linear when the dynamics of a finite-dimensional nonlinear system are transferred to infinite-dimensional function space. In an infinite-dimensional Hilbert space, g is an observable and a real-valued scalar measurement function. Based on this observable, the Koopman operator generates as follows:

$$\boldsymbol{Kg = g \circ F} \tag{7.24}$$

A continuous system can be utilized to implement smooth dynamics.

$$\boldsymbol{\frac{d}{dt} g(x) = Kg(x) = \nabla g(x).f(x)} \tag{7.25}$$

in which K is the Koopman operator. due to the Koopman operator's unlimited dimensions, which is important yet troublesome for operation and representation. Applied Koopman analysis roughly approximates the evolution of a subspace covered by a limited number of measurement functions rather than detailing the development of all measurement functions in a Hilbert space. By constraining the operator to an invariant subspace, the Koopman operator may be represented as a matrix with limited dimensions.

Any combination of the Koopman operator's eigenfunctions can cover a Koopman invariant subspace (Kaiser, Kutz, & Brunton, 2021). when the Koopman model's eigenfunction $\boldsymbol{\varphi}(\boldsymbol{x})$ satisfies eigenvalue λ.

$$\boldsymbol{\lambda\varphi}(\boldsymbol{x}) = \boldsymbol{\varphi}\big(\boldsymbol{F}(\boldsymbol{x})\big) \tag{7.26}$$

A Koopman eigenfunction $\boldsymbol{\varphi}(\boldsymbol{x})$ is satisfied in continuous time.

$$\frac{\boldsymbol{d}}{\boldsymbol{dt}}\boldsymbol{\varphi}(\boldsymbol{x}) = \boldsymbol{\lambda\varphi}(\boldsymbol{x}) \tag{7.27}$$

To approximate the Koopman operator, a finite-dimensional approximation is needed on the application side. The DMD technique is one way that can estimate the Koopman operator (Kaiser, Kutz, & Brunton, 2021).

7.6 DMD method

DMD uses a robust numerical technique to approximate the Koopman operator.

$$\boldsymbol{X'} \approx \boldsymbol{AX} \tag{7.28}$$

where $\boldsymbol{X'}$is time-shifted of matrix *X* as:

$\boldsymbol{X} = [\boldsymbol{x_1} \quad \boldsymbol{x_2} \quad \ldots\ldots]$

The equation (28) may be used to determine the A as follows:

$$\boldsymbol{A} = \boldsymbol{X'X^{+}} \tag{7.29}$$

where the Moore-Penrose pseudoinverse is represented by +. Because a normal calculation utilizing A would need a substantial amount of processing because of its

enormous n, we may utilize Singular Value Decomposition (SVD) on the snapshots to identify the dominant characteristics of the pseudoinverse of X (Snyder & Song, 2021).

$$\boldsymbol{X} \approx \boldsymbol{U\Sigma V}^{*} \tag{7.30}$$

where $\boldsymbol{U} \in \boldsymbol{R}^{\boldsymbol{n}\times\boldsymbol{r}}$, $\boldsymbol{\Sigma} \in \boldsymbol{R}^{\boldsymbol{r}\times\boldsymbol{r}}$, $\boldsymbol{V} \in \boldsymbol{R}^{\boldsymbol{n}\times\boldsymbol{r}}$, and $*$ demonstrates the conjugate transpose. SVD's reduced rank for approximating *Z* is *r*. The eigenvectors can be defined as:

$$\Phi = \boldsymbol{X'V\Sigma^{-1}}\mathrm{W} \tag{7.31}$$

where W is the eigenvectors of full-rank system dynamic systems.

$$\Phi = \boldsymbol{X'V\Sigma^{-1}}\mathrm{W} \tag{7.32}$$

Let λ be eigenfunction, then we will have:

$$\boldsymbol{KW} = \boldsymbol{\lambda W} \tag{7.33}$$

where *K* is the Koopman operator.

The demonstration of the linearized dynamic model is as follows:

$$\frac{\boldsymbol{d}}{\boldsymbol{dt}}\boldsymbol{y} = \boldsymbol{Ky} + \boldsymbol{u} \tag{7.34}$$

7.7 Koopman fractional sliding mode control

The proposed control method block diagram is shown in Figure 7.2. The fractional sliding mode surface for the linearized dynamic model by Koopman theory can be defined as:

$$\boldsymbol{s_k(t) = e_k(t) + \alpha D^{\mu} e_k(t) + \beta D^{-\mu} e_k(t)} \quad (7.35)$$

where the e_k is the tracking error as:

$$\boldsymbol{e_k(t) = y_d - y} \quad (7.36)$$

where $\boldsymbol{y_d}$ is desired trajectory tracking.

Take the derivative of fractional sliding mode surface results

$$\boldsymbol{\dot{s}_k(t) = \dot{e}_k(t) + \alpha\mu D^{\mu+1} e_k(t) - \beta\mu D^{-\mu+1} e_k(t)} \quad (7.37)$$

Take derivative from equation (7.36) and substitute it into equation (7.37) produces

$$\boldsymbol{\dot{s}_k(t) = \dot{y}_d - \dot{y} + \alpha\mu D^{\mu+1} e_k(t) - \beta\mu D^{-\mu+1} e_k(t)} \quad (7.38)$$

Substitute equation (7.34) into equation (7.38) introduces

$$\boldsymbol{\dot{s}_k(t) = \dot{y}_d - Ky - u + \alpha\mu D^{\mu+1} e_k(t) - \beta\mu D^{-\mu+1} e_k(t)} \quad (7.39)$$

Equal equation (7.39) to zero and simplify it produces

$$\boldsymbol{u_{eq}(t) = \dot{y}_d - Ky + \alpha\mu D^{\mu+1} e_k(t) - \beta\mu D^{-\mu+1} e_k(t)} \quad (7.40)$$

The equivalent control is not able to suppress external disturbances. The reaching control can be defined as:

$$\boldsymbol{u_{rk}(t) = K_{rk} s_k(t)} \quad (7.41)$$

where $\boldsymbol{K_{rk}}$ is the reaching control gain is positive constant.

The KFOSMC is defined as:

$$\boldsymbol{u_{KFOSMC}(t) = u_{rk}(t) + u_{eq}(t)} \tag{7.42}$$

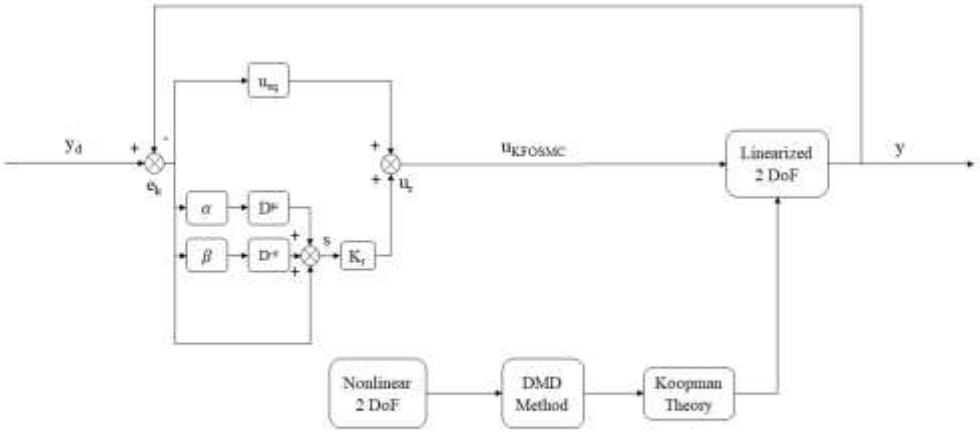

Figure 7.2: The proposed control method block diagram.

The stability of the proposed control method can be proved by using the Lyapunov theory:

$$\boldsymbol{V(t) = \frac{1}{2} s_k^T(t) s_k(t)} \tag{7.43}$$

Take the derivative from equation (7.43) produces

$$\boldsymbol{\dot{V}(t) = s_k^T(t) \dot{s}_k(t)} \tag{7.44}$$

Substitute equation (7.39) into equation (7.44) produces

$$\dot{\boldsymbol{V}}(\boldsymbol{t}) = \boldsymbol{s}_{\boldsymbol{k}}^{\boldsymbol{T}}(\boldsymbol{t})(\dot{\boldsymbol{y}}_{\boldsymbol{d}} - \boldsymbol{K}\boldsymbol{y} - \boldsymbol{u} + \boldsymbol{\alpha}\boldsymbol{\mu}\boldsymbol{D}^{\boldsymbol{\mu}+\boldsymbol{1}}\boldsymbol{e}_{\boldsymbol{k}}(\boldsymbol{t}) - \boldsymbol{\beta}\boldsymbol{\mu}\boldsymbol{D}^{-\boldsymbol{\mu}+\boldsymbol{1}}\boldsymbol{e}_{\boldsymbol{k}}(\boldsymbol{t})) \quad (7.45)$$

Substitute equation (7.42) in equation (7.45) results

$$\dot{V}(t) = s_k^T(t)(\dot{y}_d - Ky - u_{rk}(t) - u_{eq}(t) + \alpha\mu D^{\mu+1}e_k(t) - \beta\mu D^{-\mu+1}e_k(t)) \quad (7.46)$$

Substitute equation (7.40) in equation (7.46) introduces

$$\dot{V}(t) = s_k^T(t)(\dot{y}_d - Ky - u_{rk}(t) - \dot{y}_d + Ky - \alpha\mu D^{\mu+1}e_k(t) + \beta\mu D^{-\mu+1}e_k(t) + \alpha\mu D^{\mu+1}e_k(t) - \beta\mu D^{-\mu+1}e_k(t)) \quad (7.47)$$

Simplify equation (7.47) results

$$\dot{V}(t) = s_k^T(t)(-u_{rk}(t)) \quad (7.48)$$

Substitute equation (7.41) in equation (7.48) produces

$$\dot{V}(t) = s_k^T(t)(-K_{rk}s_k(t)) \quad (7.49)$$

Equation (7.4) demonstrates that the proposed control method is stable.

7.8 Simulation results

We simulate three controllers to show the performance of the proposed control method. The robot's specifications are as $M_1 = M_2 = L_1 = L_2 = 1$ and $g = 9.81\, m/s$. The PID controller parameters are selected as $K_p = diag\{40,40\}, K_i = diag\{10,10\}$, and

$K_d = diag\{20,20\}$. The FOSMC controller parameters are chosen as $K_r = 10, \alpha = 10, \beta = 5$, and $\mu = 0.75$, which the KFOSMC parameters are the same with FOSMC. The

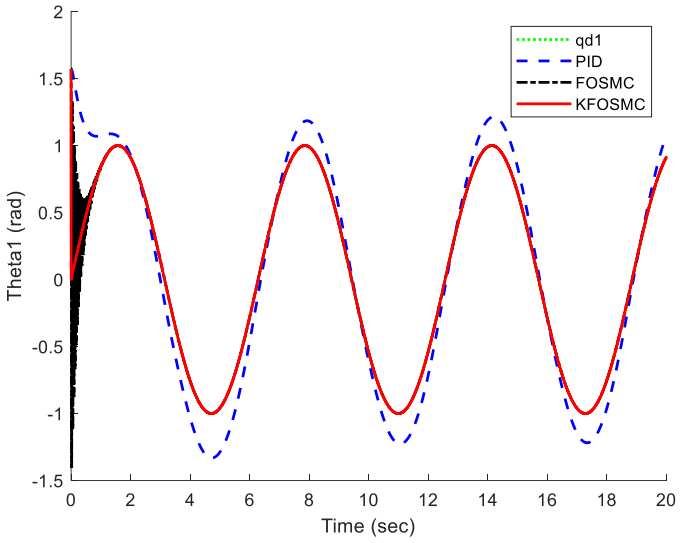

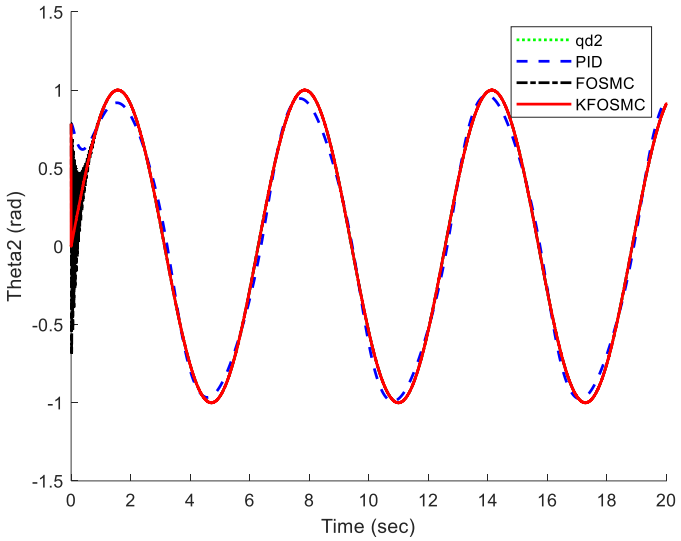

Figure 7.3: Tracking trajectory under PID, FOSMC, and KFOSMC controllers.

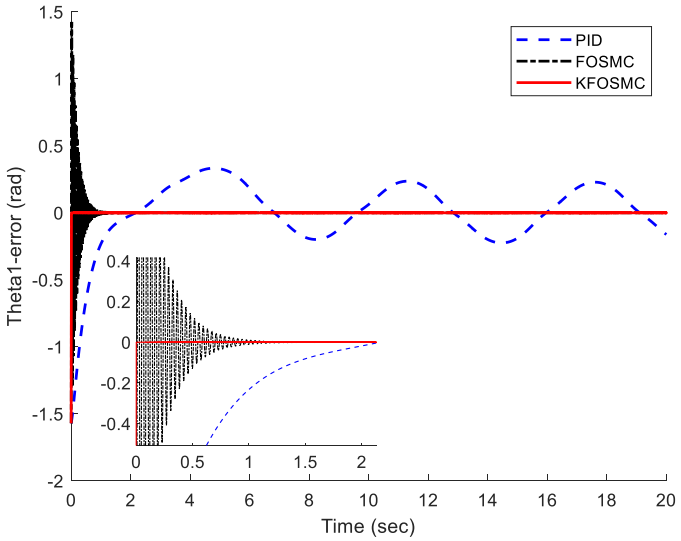

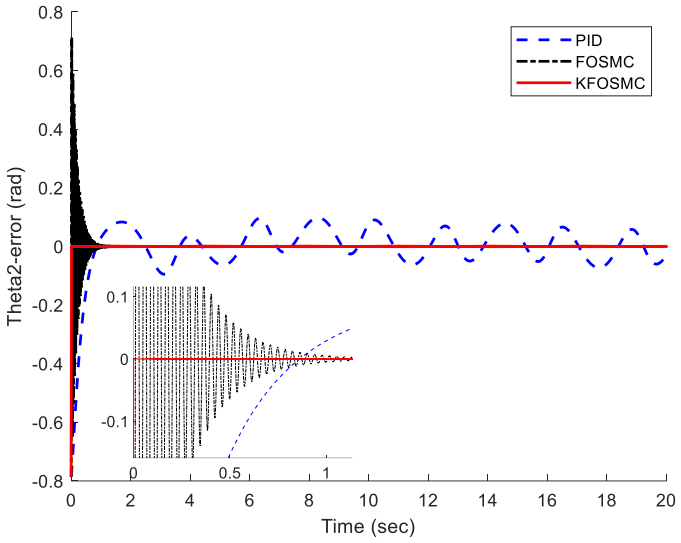

Figure 7.4: Trajectory tracking error under PID, FOSMC, and KFOSMC controllers.

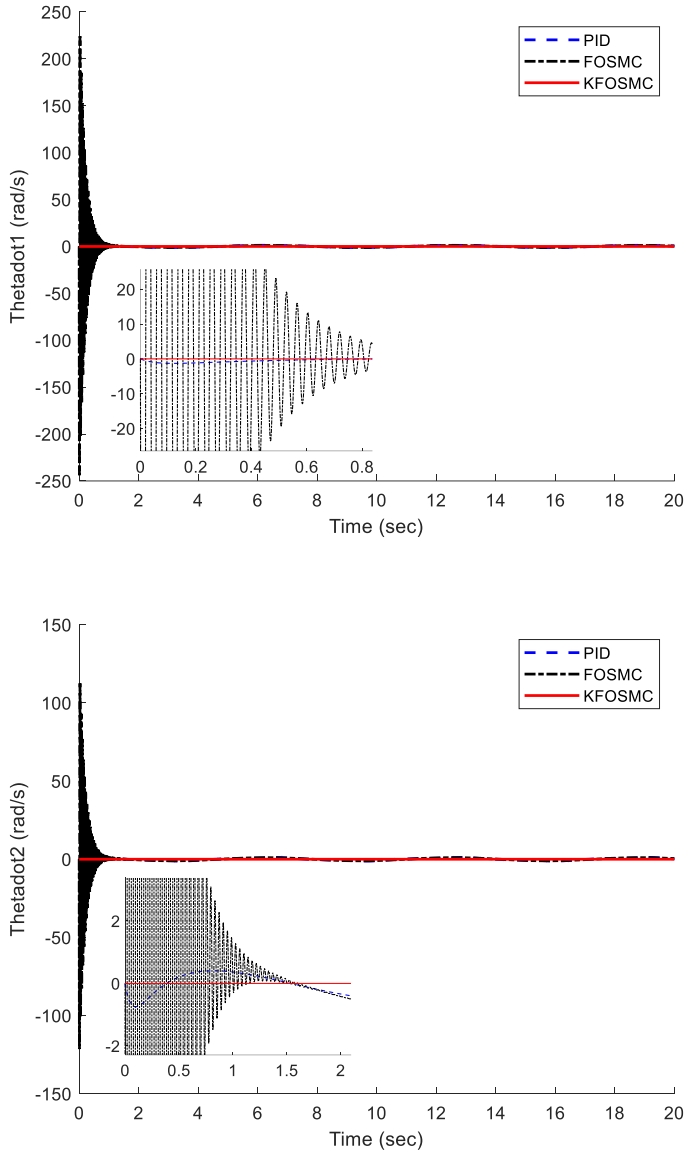

Figure 7.5: Velocity of each joints under PID, FOSMC, and KFOSMC controllers.

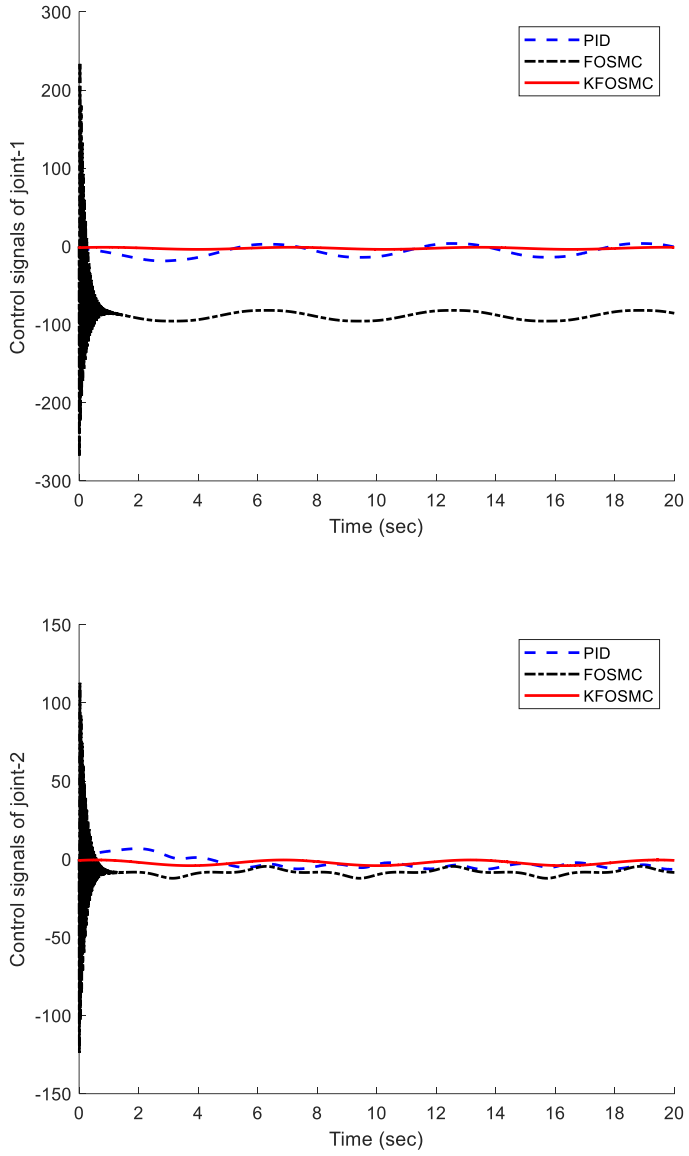

Figure 7.6: Control signals under PID, FOSMC, and KFOSMC controllers.

desired trajectory tracking is as $q_d = y_d = \sin(t)$. The initial conditions of joints are as $q_1 = \frac{\pi}{2}, q_2 = \frac{\pi}{4}$

Figure 7.3 shows the trajectory tracking of joints 1 and 2 under PID, FOSMC, and KFOSMC. It demonstrated that the KFOSMC has better trajectory tracking performance in comparison with PID and FOSMC controllers. Figure 7.4 shows the trajectory tracking error of joints 1 and 2 under PID, FOSMC, and KFOSMC controllers. For example, the tracking error in joint 1 in time of 4 sec under PID controller is around 0.5, but under KFOSMC is equal to zero. Also, for that joint FOSMC creates oscillation, but by applying KFOSMC, there are no tracking errors. Therefore, the tracking error under KFOSMC is zero in comparison to the two other controllers. Figure 3.5 shows the velocity of joints 1 and 2 under PID, FOSMC, and KFOSMC controllers. Figure 7.6 shows the control signals under PID, FOSMC, and KFOSMC controllers. The control signals using KFOSMC reduced significantly in comparison with the two other controllers.

7.9 Conclusion

This research proposed a new data-driven control method to control a 2 DoF robot manipulator. The robot manipulator is highly nonlinear. The Koopman theory is used to linearize the nonlinear dynamic model of a 2 DoF robot manipulator. The DMD method was applied to obtain the Koopman operator. Then, PID and FOSMC are used to show the

controller performance before using the Koopman theory. The simulation results demonstrated that the proposed control method has better performance in terms of high tracking performance, low tracking error, and low control signals in comparison with PID and FOSMC controllers.

REFERENCES

Abdelouahab, M. S., & Hamri, N. E. (2016). The Grünwald–Letnikov fractional-order derivative with fixed memory length. *Mediterranean Journal of Mathematics*, 13(2), 557-572.

Abraham, I., & Murphey, T. D. (2019). Active learning of dynamics for data-driven control using Koopman operators. *IEEE Transactions on Robotics*, 35(5), 1071-1083.

Aghababa, M. P. (2014). Design of hierarchical terminal sliding mode control scheme for fractional-order systems. *IET Science, Measurement & Technology*, 9(1), 122-133.

Ahmad, M. N., & Osman, J. H. ((2003, August).). Robust sliding mode control for robot manipulator tracking problem using a proportional-integral switching surface. *In Proceedings. Student Conference on* Research *and Development, 2003. SCORED 2003* (pp. (pp. 29-35)). IEEE.

Anavatti, S. G., Salman, S. A., & Choi, J. Y. ((2006, December)). Fuzzy+ PID controller for robot manipulator. *In 2006 International Conference on Computational* Inteligence *for Modelling Control and Automation and International Conference on Intelligent Age Web Technologies and International Commerce (CIMCA'06)* (pp. (pp. 75-75)). IEEE.

Anjali, B. S., Vivek, A., & Nandagopal, J. L. (2016). Simulation and analysis of integral LQR controller for inner control loop design of a fixed wing micro aerial vehicle (MAV). Procedia *Technology*, 25, 76-83.

Arbabi, H. (2018). Introduction to Koopman operator theory of dynamical systems. *Introduction to Koopman operator theory of dynamical systems*.

Arbabi, H., Korda, M., & Mezić, I. ((2018, December)). A data-driven koopman model predictive control framework for nonlinear partial differential equations. *In 2018 IEEE Conference on Decision and Control (CDC)* (pp. (pp. 6409-6414)). Miami, FL: IEEE.

Ardjal, A., Mansouri, R., & Bettayeb, M. (2018). Fractional sliding mode control of wind turbine for maximum power point tracking. *Transactions of the Institute of Measurement and* Control, 0142331218764569.

Balochian, S. (2013). Sliding mode control of fractional order nonlinear differential inclusion systems. *Evolving Systems*, 4(3), 145-152.

Becerra, H. M., Hayet, J. B., & Sagüés, C. (2014). A single visual-servo controller of mobile robots with super-twisting control. *Robotics and Autonomous Systems*, 62(11), 1623-1635.

Bruder, D., Fu, X., Gillespie, R. B., Remy, C. D., & Vasudevan, R. (2020). Data-driven control of soft robots using koopman operator theory. *IEEE Transactions on Robotics*, 37(3), 948-961.

Brunton, S. L., Brunton, B. W., Proctor, J. L., & Kutz, J. N. (2016). Koopman invariant subspaces and finite linear representations of nonlinear dynamical systems for control. *PloS one*, 11(2), e0150171.

Calderón, H. M., Schulz, E., Oehlschlägel, T., & Werner, H. ((2021, June)). Koopman Operator-based Model Predictive Control with Recursive Online Update. *In 2021 European Control Conference (ECC)* (pp. (pp. 1543-1549)). Delft, Netherlands: IEEE.

Carron, A., Arcari, E., Wermelinger, M., Hewing, L., Hutter, M., & Zeilinger, M. N. (2019). Data-driven model predictive control for trajectory tracking with a robotic arm. *IEEE Robotics and Automation Letters*, 4(4), 3758-3765.

Cervantes, I., & Alvarez-Ramirez, J. (2001). On the PID tracking control of robot manipulators. *Systems & control letters*, 42(1), 37-46.

Chaib, L., Choucha, A., & Arif, S. (2017). Optimal design and tuning of novel fractional order PID power system stabilizer using a new metaheuristic Bat algorithm. *Ain Shams* Engineering *Journal*, 8(2), 113-125.

Chen, J., Dang, Y., & Han, J. (2022). Offset-free model predictive control of a soft manipulator using the Koopman operator. *Mechatronics*, 86, 102871.

Chen, W. H., & You, F. (2021). Semiclosed greenhouse climate control under uncertainty via machine learning and data-driven robust model predictive control. *IEEE Transactions on Control Systems Technology*, 30(3), 1186-1197.

Chuei, R., Cao, Z., & Man, Z. (2017). Super twisting observer based repetitive control for aperiodic disturbance rejection in a brushless DC servo motor. *International Journal of Control, Automation and Systems*, 15(5), 2063-2071.

Classen, J., Frey, J., Kuhlmann, B., Ernst, P., & Bosch, R. (2007). *MEMS gyroscopes for automotive applications.* Berlin, Germany: Springer.

Cui, J., & Zhao, Q. ((2021, January)). A Tactical-Grade Monolithic Horizontal Dual-Axis Mems Gyroscope Based On Off-Plane Quadrature Coupling Suppression Silicon Gratings. *In 2021 IEEE 34th International Conference on Micro Electro Mechanical Systems (MEMS).* IEEE.

Devanshu, A., Singh, M., & Kumar, N. (2020). Sliding mode control of induction motor drive based on *feedback* linearization. *IETE Journal of Research*, 66(2), 256-269.

Erol, H. (2021). Stability analysis of pitch angle control of large wind turbines with fractional order PID controller. *Sustainable Energy, Grids and Networks*, 26, *100430*.

Evangelista, C., Puleston, P., Valenciaga, F., & Fridman, L. M. (2012). Lyapunov-designed super-twisting sliding mode control for wind energy conversion optimization. IEEE *Transactions on industrial electronics*, 60(2), 538-545.

Fang, Y., Fu, W., Ding, H., & Fei, J. (2022). Modeling and neural sliding mode control of mems triaxial gyroscope. *Advances in Mechanical Engineering*, 14(3), 16878132221085876.

Fazeli Asl, S. B., & Moosapour, S. S. (2021). Fractional order fuzzy dynamic backstepping sliding mode controller design for triaxial MEMS gyroscope based on high-gain and disturbance observers. *IETE Journal of Research*, 67(6), 799-816.

Fei, J., & Chu, Y. ((2016, August)). Dynamic global PID sliding mode control for MEMS gyroscope using adaptive neural controller. *In 2016 Joint 8th International* Conference *on Soft Computing and Intelligent Systems (SCIS) and 17th International Symposium on Advanced Intelligent Systems (ISIS)* (pp. 16-21). Sapporo, Japan: IEEE.

Fei, J., & Feng, Z. (2020). Fractional-order finite-time super-twisting sliding mode control of micro gyroscope based on double-loop fuzzy neural network. *IEEE Transactions on Systems, Man, and Cybernetics: Systems*, 51(12), 7692-7706.

Folkestad, C., & Burdick, J. W. ((2021, May)). Koopman NMPC: Koopman-based learning and nonlinear model predictive control of control-affine systems. *In 2021 IEEE International Conference on Robotics and Automation (ICRA)* (pp. (pp. 7350-7356)). IEEE.

Gao, P., Zhang, G., Ouyang, H., & Mei, L. (2020). An adaptive super twisting nonlinear *fractional* order PID sliding mode control of permanent magnet synchronous motor speed regulation system based on extended state observer. *IEEE access*, 8, 53498-53510.

Gao, S., Liu, L., Wang, H., & Wang, A. (2022). Data-driven model-free resilient speed control of an Autonomous Surface Vehicle in the presence of actuator anomalies. *ISA Transactions*.

Gao, Z., & Liao, X. (2013). Integral sliding mode control for fractional-order systems with mismatched uncertainties. *Nonlinear Dynamics*, 72(1-2), 27-35.

Ghanbari, A., & Noorani, S. M. (2011). Optimal trajectory planning for design of a crawling gait in a robot using genetic algorithm. *International Journal of Advanced Robotic Systems*, 8(1), 6.

Gibson, A., Yee, X., & Calvisi, M. (2021). Application of Koopman LQR to the control of nonlinear bubble dynamics. *In APS Division of Fluid Dynamics Meeting Abstracts* , (pp. P21-003).

Goswami, D., & Paley, D. A. (2021). Bilinearization, reachability, and optimal control of control-affine nonlinear systems: A Koopman spectral approach. *IEEE Transactions on Automatic Control.*

Goswami, D., & Paley, D. A. (2021). Bilinearization, reachability, and optimal control of control-affine nonlinear systems: A Koopman spectral approach. *IEEE Transactions on Automatic Control.*

Guo, T. Y., Lu, L. S., Lin, S. Y., & Hwang, C. (2022). Design of maximum-stability PID controllers for LTI systems based on a stabilizing-set construction method. *Journal of the Taiwan Institute of Chemical Engineers,*, 135, 104366.

Guo, Y., Xu, B., & Zhang, R. (2020). Terminal sliding mode control of mems gyroscopes with finite-time learning. *IEEE Transactions on Neural Networks and Learning Systems*, 32(10), 4490-4498.

Guruganesh, R., Bandyopadhyay, B., Arya, H., & Singh, G. K. (2018). Design and Hardware Implementation of Autopilot Control Laws for MAV Using Super Twisting Control. *Journal of Intelligent & Robotic Systems*, 1-17.

Hadian, M., Ramezani, A., & Zhang, W. (2021). Robust Model Predictive Controller Using Recurrent Neural Networks for Input–Output Linear Parameter Varying Systems. *Electronics*, 10(13), 1557.

Hadian, M., Ramezani, A., & Zhang, W. (2022). An interpolation-based model predictive controller for input–output linear parameter varying systems. *International Journal of* Dynamics *and Control*, 1-14.

Henson, P., & Marais, S. ((2012, November)). The utilization of duplex worm gears in robot manipulator arms: A design, build and test approach. *In 2012 5th Robotics and Mechatronics Conference of South Africa* (pp. (pp. 1-4)). IEEE.

Huimin, W., Liang, H., Yunxiang, G., Hailong, C., & Cheng, L. ((2019, June)). Adaptive neural Sliding Mode Control for MEMS gyroscope using fractional calculus. *In 2019 34th Youth Academic Annual Conference* of *Chinese Association of Automation (YAC)* (pp. (pp. 602-606)). Jinzhou, China: IEEE.

Husham, A., Kamwa, I., Abido, M. A., & Suprême, H. (2022). Decentralized Stability Enhancement of DFIG-Based Wind Farms in Large Power Systems: Koopman Theoretic Approach. *IEEE Access*, 10, 27684-27697.

Islam, S., & Liu, X. P. (2010). Robust sliding mode control for robot manipulators. *IEEE Transactions on industrial electronics*, 58(6), 2444-2453.

Jeong, C. S., Kim, J. S., & Han, S. I. (2018). Tracking Error Constrained Super-twisting Sliding Mode Control for Robotic Systems. *International Journal of Control, Automation and Systems*, 16(2), 804-814.

Jiang, L., & Liu, N. (2022). Correcting noisy dynamic mode decomposition with Kalman filters. *Journal* of *Computational Physics*, 461, 111175.

Jin, M., Lee, J., Chang, P. H., & Choi, C. (2009). Practical nonsingular terminal sliding-mode control of robot manipulators for high-accuracy tracking control. *IEEE Transactions on Industrial Electronics*, 56(9), 3593-3601.

Joey, Z. G., Calderón, A. A., Chang, L., & Pérez-Arancibia, N. O. (2019). An earthworm-inspired friction-controlled soft robot capable of bidirectional locomotion. Bioinspiration & *biomimetics*, 14(3), 036004.

Junker, A., Timmermann, J., & Trächtler, A. ((2022, May)). Data-driven models for control engineering applications using the Koopman operator. *In 2022 3rd International Conference on Artificial Intelligence, Robotics and Control (AIRC)* (pp. (pp. 1-9)). IEEE.

Kaiser, E., Kutz, J. N., & Brunton, S. L. (2021). Data-driven discovery of Koopman eigenfunctions for control. *Machine Learning: Science and Technology,*, 2(3), 035023.

Kaur, S., & Narayan, S. (2018). Fractional order uncertainty estimator-based hierarchical sliding mode design for a class of fractional order non-holonomic chained system. *ISA transactions*, 77, 58-70.

Kelly, R. (1995). A tuning procedure for stable PID control of robot manipulators. *Robotica*, 13(2), 141-148.

Khan, A., & Tyagi, A. (2017). Fractional order disturbance observer based adaptive sliding mode synchronization of commensurate fractional order Genesio-Tesi system. *AEU-International Journal of Electronics and Communications*, 82, 346-357.

Korda, M., & Mezić, I. (2020). Optimal construction of Koopman eigenfunctions for prediction and control. *IEEE Transactions on Automatic Control*, 65(12), 5114-5129.

Kou, J., Le Clainche, S., & Ferrer, E. (2022). Data-driven eigensolution analysis based on a spatio-temporal Koopman decomposition, with applications to high-order methods. *Journal of Computational Physics,*, 449, 110798.

Kumar, J. S., & Amutha, E. K. ((2014, December)). Control and tracking of robotic manipulator using PID controller and hardware in Loop Simulation. *In 2014 International Conference on Communication and Network Technologies* (pp. (pp. 1-3).). IEEE.

Lakshmanaprabu, S. K., Elhoseny, M., & Shankar, K. (2019). Optimal tuning of decentralized fractional order PID controllers for TITO process using equivalent transfer function. *Cognitive Systems Research*, 58, 292-303.

Li, J. W., Chen, X. B., & Zhang, W. J. (2010). Axiomatic-design-theory-based approach to modeling linear high order system dynamics. *IEEE/ASME Transactions on Mechatronics*, 16(2), 341-350.

Ling, E., Zheng, L., Ratliff, L. J., & Coogan, S. (2020). Koopman operator applications in signalized traffic systems. *IEEE Transactions on Intelligent Transportation Systems*.

Liu, H., Cheng, Q., Xiao, J., & Hao, L. (2022). Data-driven adaptive integral terminal sliding mode control for uncertain SMA actuators with input saturation and prescribed performance. *ISA transactions*, 128, 624-632.

Liu, L., Zhang, L., Pan, G., & Zhang, S. (2022). Robust yaw control of autonomous underwater vehicle based on fractional-order PID controller. *Ocean Engineering, ,* 257, 111493.

Liu, Y., Chen, Y., Feng, B., Wang, D., Liu, T., Zhou, H., . . . Yang, W. (2022). S2worm: A Fast-moving Untethered Insect-scale Robot with 2-DoF Transmission Mechanism. *IEEE Robotics and Automation Letters*.

Lu, C., & Fei, J. ((2016, June)). Adaptive sliding mode control of MEMS gyroscope with prescribed performance. *In 2016 14th International Workshop on Variable Structure* Systems *(VSS)* (pp. pp. 65-70). Nanjing: IEEE.

Lu, K., & Xia, Y. (2014). Finite-time attitude control for rigid spacecraft-based on adaptive super-twisting algorithm. *IET Control Theory & Applications*, 8(15), 1465-1477.

Luo, S., Yang, G., Li, J., & Ouakad, H. M. (2022). Dynamic analysis, circuit realization and accelerated adaptive backstepping control of the FO MEMS gyroscope. . *Chaos, Solitons & Fractals*, 155, 111735.

Lusch, B., Kutz, J. N., & Brunton, S. L. (2018). Deep learning for universal linear embeddings of nonlinear dynamics. *Nature communications*, 9(1), 1-10.

Malarvili, S., & Mageshwari, S. (2022). Nonlinear PID (N-PID) Controller for SSSP Grid Connected Inverter Control of Photovoltaic Systems. *Electric Power Systems Research*, 211, 108175.

Mamakoukas, G., Castano, M., Tan, X., & Murphey, T. ((2019, June)). Local Koopman operators for data-driven control of robotic systems. *In Robotics: science and systems.*

Mansour, H., Benosman, M., & Huroyan, V. ((2017, July)). Crowd flow completion from partial spatial observations using kernel DMD. *In 2017 International Conference on* Sampling *Theory and Applications (SampTA)* (pp. (pp. 451-455)). IEEE.

Marino, R., Scalzi, S., & Netto, M. (2011). Nested PID steering control for lane keeping in autonomous vehicles. *Control Engineering Practice*, 19(12), 1459-1467.

Mitić, M., & Miljković, Z. (2015). Bio-inspired approach to learning robot motion trajectories and visual control commands. *Expert Systems with Applications*, 42(5), 2624-2637.

Mujumdar, A., Tamhane, B., & Kurode, S. (2015). Observer-based sliding mode control for a class of noncommensurate fractional-order systems. *IEEE/ASME Transactions on Mechatronics*, 20(5), 2504-2512.

Narasingam, A., Son, S. H., & Kwon, J. S. (2022). Data-driven feedback stabilisation of nonlinear systems: Koopman-based model predictive control. *International Journal of Control*, 1-12.

Nathan Kutz, J., Proctor, J. L., & Brunton, S. L. (2018). Applied Koopman theory for partial differential equations and data-driven modeling of spatio-temporal systems. *Complexity*.

Onal, C. D., Wood, R. J., & Rus, D. (2012). An origami-inspired approach to worm robots. *IEEE/ASME Transactions on Mechatronics*, 18(2), 430-438.

Ortiz, D., Gravish, N., & Tolley, M. T. (2019). Soft robot actuation strategies for *locomotion* in granular substrates. *IEEE Robotics and Automation Letters*, 4(3), 2630-2636.

Perwaiz, U., Younas, I., & Anwar, A. A. (2020). Many-objective BAT algorithm. *Plos one*, 15(6), *e0234625*.

Piltan, F., & *Sulaiman*, N. B. (2012). Review of sliding mode control of robotic manipulator. *World Applied Sciences Journal*, 18(12), 1855-1869.

Ping, Z., Yin, Z., Li, X., Liu, Y., & Yang, T. (2021). Deep Koopman model predictive *control* for enhancing transient stability in power grids. *International Journal of Robust and Nonlinear Control*, 31(6), 1964-1978.

Prasad, L. B., Tyagi, B., & Gupta, H. O. (2014). Optimal control of nonlinear inverted pendulum system using PID controller and LQR: performance analysis without and with disturbance input. *International Journal of Automation and Computing*, 11(6), 661-670.

Qian, S., & Chou, C. A. (2021). A Koopman-operator-theoretical approach for anomaly recognition and detection of multi-variate EEG system. *Biomedical Signal Processing and Control*, 69, 102911.

Rabah, K., Ladaci, S., & Lashab, M. (2017). A novel fractional sliding mode control configuration for synchronizing disturbed fractional-order chaotic systems. *Pramana*, 89(3), 46.

Rahmani, M. (2018). MEMS gyroscope control using a novel compound robust control. *ISA* transactions, 72, 37-43.

Rahmani, M., & Rahman, M. H. (2019). A new adaptive fractional sliding mode control of a MEMS gyroscope. *Microsystem Technologies*, 25(9), 3409-3416.

Rahmani, M., & Rahman, M. H. (2019). A novel compound fast fractional integral sliding mode control and adaptive PI control of a MEMS gyroscope. *Microsystem Technologies*, 25(10), 3683-3689.

Rahmani, M., & Rahman, M. H. (2020). Adaptive neural network fast fractional sliding mode control of a 7-DOF exoskeleton robot. *International Journal of Control, Automation and* Systems, 18(1), 124-133.

Rahmani, M., Ghanbari, A., & Ettefagh, M. M. (2016). Hybrid neural network fraction integral terminal sliding mode control of an Inchworm robot manipulator. *Mechanical Systems and Signal Processing*, 80, 117-136.

Rahmani, M., Ghanbari, A., & Ettefagh, M. M. (2016). Robust adaptive control of a bio-inspired robot manipulator using bat algorithm. *Expert Systems with Applications*, 56, 164-176.

Rahmani, M., Ghanbari, A., & Ettefagh, M. M. (2018). A novel adaptive neural network integral sliding-mode control of a biped robot using bat algorithm. *Journal of Vibration and Control*, 24(10), 2045-2060.

Rahmani, M., Komijani, H., Ghanbari, A., & Ettefagh, M. M. (2018). Optimal novel super-twisting PID sliding mode control of a MEMS gyroscope based on multi-objective bat algorithm. *Microsystem Technologies*, 24(6), 2835-2846.

Rahmani, M., Rahman, M. H., & Ghommam, J. (2020). *Compound Fractional Integral Terminal* Sliding *Mode Control and Fractional PD Control of a MEMS Gyroscope.* Springer.

Rahmani, M., Rahman, M. H., & Nosonovsky, M. (2020). A new hybrid robust control of MEMS gyroscope. *Microsystem Technologies*, 26(3), 853-860.

Ravari, A. N., & Taghirad, H. D. ((2009, February)). A novel hybrid Fuzzy-PID controller for *tracking* control of robot manipulators. *In 2008 IEEE international conference on robotics and biomimetics* (pp. (pp. 1625-1630)). IEEE.

Rotulo, M., De Persis, C., & Tesi, P. (2020). Data-driven linear quadratic regulation via semidefinite programming. *IFAC-PapersOnLine*, 53(2), 3995-4000.

Salgado, I., Kamal, S., Bandyopadhyay, B., Chairez, I., & Fridman, L. (2016). Control of discrete-time systems based on recurrent super-twisting-like algorithm. *ISA* transactions, 64, 47-55.

Sathya, M. R., & Ansari, M. M. (2015). Load frequency control using Bat inspired algorithm based dual mode gain scheduling of PI controllers for interconnected power system. International *Journal of Electrical Power & Energy Systems*,, 64, 365-374.

Schulze, J. C., Doncevic, D. T., & Mitsos, A. (2022). Identification of MIMO Wiener-type Koopman models for data-driven model reduction using deep learning. *Computers & Chemical Engineering*, 161, 107781.

Shah, D., & Mehta, A. (2017). Discrete-time sliding mode controller subject to real-time fractional delays and packet losses for networked control system. *International Journal of Control, Automation and Systems*, 15(6), 2690-2703.

Sharma, R., Rana, K. P., & Kumar, V. (2014). Performance analysis of fractional order fuzzy PID controllers applied to a robotic manipulator. *Expert systems with applications*, 41(9), 4274-4289.

Shi, H., & Meng, M. Q. (2022). Deep Koopman operator with control for nonlinear systems. *IEEE Robotics and Automation Letters*.

Shi, L., & Karydis, K. ((2021)). ACD-EDMD: Analytical Construction for Dictionaries of Lifting Functions in Koopman Operator-Based Nonlinear Robotic Systems. *IEEE Robotics and Automation Letters*, 7(2), 906-913.

Shi, Y., Shao, X., & Zhang, W. (2020). Neural observer-based quantized output feedback control for MEMS gyroscopes with guaranteed transient performance. *Aerospace Science and Technology*, 105, 106055.

Sinha, S., Nandanoori, S. P., & Yeung, E. (2020). Koopman operator methods for global phase space exploration of equivariant dynamical systems. *IFAC-PapersOnLine*, 53(2), 1150-1155.

Snyder, G., & Song, Z. (2021). Koopman Operator Theory for Nonlinear Dynamic Modeling using Dynamic Mode Decomposition. *arXiv preprint arXiv*, 2110.08442.

Solouk, M. R., Shojaeefard, M. H., & Dahmardeh, M. (2019). Parametric topology optimization of a MEMS gyroscope for automotive applications. *Mechanical Systems and Signal Processing*, 128, 389-404.

Son, S. H., Narasingam, A., & Kwon, J. S. ((2021, May)). Integration of offset-free control framework with Koopman Lyapunov-based model predictive control. *In 2021 American Control Conference (ACC)* (pp. (pp. 2818-2823)). IEEE.

Su, Y., Müller, P. C., & Zheng, C. (2009). Global asymptotic saturated PID control for robot manipulators. *IEEE Transactions on Control systems technology*, 18(6), 1280-1288.

Su, Y., Xu, P., Han, G., Si, C., Ning, J., & Yang, F. (2020). The characteristics and locking process of nonlinear MEMS gyroscopes. *Micromachines*, 11(2), 233.

Sun, C., Dominguez-Caballero, J., Ward, R., Ayvar-Soberanis, S., & Curtis, D. (2022). Machining cycle time prediction: Data-driven modelling of machine tool feedrate behavior with neural networks. *Robotics and Computer-Integrated Manufacturing*, 75, 102293.

Sun, G., & Ma, Z. (2017). Practical tracking control of linear motor with adaptive fractional order terminal sliding mode control. *IEEE/ASME Transactions on Mechatronics*, 22(6), 2643-2653.

Sun, S., Yin, Y., Wang, X., & Xu, D. (2018). Robust landmark detection and position measurement based on monocular vision for autonomous aerial refueling of UAVs. *IEEE Transactions on Cybernetics*, 49(12), 4167-4179.

Varghese, P. M., & Priya, P. L. ((2018, July).). Robust Control of a Dimensionless Dual Axis MEMS Vibratory Gyroscope-A Sliding Mode Approach. *In 2018 International CET Conference on Control, Communication, and Computing (IC4)* (pp. (pp. 57-62).). IEEE.

Wang, H. P., Mustafa, G. I., & Tian, Y. (2018). Model-free fractional-order sliding mode control for an active vehicle suspension system. *Advances in Engineering Software*, 115, 452-461.

Wang, X., Zhang, Q., Zhang, Y., & Wang, S. ((2018, May)). Rhythmic control method of a worm robot based on neural CPG. *In 2018 13th IEEE Conference on Industrial Electronics and Applications (ICIEA)* (pp. (pp. 1108-1112)). IEEE.

Wang, Y. ((2020, August)). Data-driven trajectory tracking of manipulator with event-triggered model updating. *In Journal of Physics: Conference Series*, (Vol. 1601, No. 6, p. 062013).

Wang, Y., Gu, L., Xu, Y., & Cao, X. (2016). Practical tracking control of robot manipulators with continuous fractional-order nonsingular terminal sliding mode. *IEEE Transactions on Industrial Electronics*, 63(10), 6194-6204.

Wang, Z., & Fei, J. ((2021, January)). Double Loop Neural Fractional-Order Terminal Sliding Mode Control of MEMS Gyroscope. *In 2021 Second International Symposium on Instrumentation, Control, Artificial Intelligence, and Robotics (ICA-SYMP)* (pp. (pp. 1-4).). IEEE.

Wang, Z., & Fei, J. (2021). Fractional-order terminal sliding mode control using self-evolving recurrent Chebyshev fuzzy neural network for MEMS gyroscope. *IEEE Transactions on Fuzzy Systems*.

Wilches-Bernal, F., Reno, M. J., & Hernandez-Alvidrez, J. (2021). A Dynamic Mode Decomposition Scheme to Analyze Power Quality Events. *IEEE Access*, 9, 70775-70788.

Williams, M. O., Hemati, M. S., Dawson, S. T., Kevrekidis, I. G., & Rowley, C. W. (2016). Extending data-driven Koopman analysis to actuated systems. *IFAC-PapersOnLine*, 49(18), 704-709.

Xian, B., Gu, X., & Pan, X. (2022). Data driven adaptive robust attitude control for a small size unmanned helicopter. *Mechanical Systems and Signal Processing*, 177, 109205.

Yan, L., Webber, J. L., Mehbodniya, A., Moorthy, B., Sivamani, S., Nazir, S., & Shabaz, M. (2022). Distributed optimization of heterogeneous UAV cluster PID controller based on machine learning. *Computers and Electrical Engineering*, 101, 108059.

Yan, W., Hou, S., Fang, Y., & Fei, J. (2017). Robust adaptive nonsingular terminal sliding mode control of MEMS gyroscope using fuzzy-neural-network compensator. *International Journal of Machine Learning And Cybernetics*, 8(4), 1287-1299.

Yang, N., & Liu, C. (2013). A novel fractional-order hyperchaotic system stabilization via fractional sliding-mode control. *Nonlinear Dynamics*, 74(3), 721-732.

Yang, X. S. (2010). A new metaheuristic bat-inspired algorithm. *In Nature inspired cooperative strategies for optimization (NICSO 2010)* (pp. pp. 65-74). Berlin, Heidelberg.: Springer.

Yang, X. S. (2012). Bat algorithm for multi-objective optimisation. *arXiv preprint arXiv:*, 1203.6571.

Yoon, J., & Doh, J. (2022). Optimal PID control for hovering stabilization of quadcopter using long short term memory. *Advanced Engineering Informatics*, 53, 101679.

Zanini, F., & Chiuso, A. (2021). Estimating Koopman operators for nonlinear dynamical systems: a nonparametric approach. *IFAC-PapersOnLine*, (pp. 54(7), 691-696.).

Zargham, F., & Mazinan, A. H. (2018). Super-twisting sliding mode control approach with its application to wind turbine systems. *Energy Systems*, 1-19.

Zarrouk, D., Sharf, I., & Shoham, M. (2012). Conditions for worm-robot locomotion in a flexible environment: theory and experiments. *IEEE transactions on biomedical engineering*, 59(4), 1057-1067.

Zhang, R., Shao, T., Zhao, W., Li, A., & Xu, B. (2018). Sliding mode control of MEMS gyroscopes using composite learning. *Neurocomputing*, 275, 2555-2564.

Zhang, W. J., & Lin, Y. (2010). On the principle of design of resilient systems–application to enterprise information systems. *Enterprise Information System*, 4(2), 99-110.

Zhang, X., Pan, W., Scattolini, R., Yu, S., & Xu, X. (2022). Robust tube-based model predictive control with Koopman operators. *Automatica*, 137, 110114.

Zhao, Z., Gu, H., Zhang, J., & Ding, G. (2017). Terminal sliding mode control based on a super-twisting algorithm. *Journal of Systems Engineering and Electronics*, 28(1), 145-150.

Zhou, Y., Fan, Q., Liu, M., Ren, J., Zhou, T., & Su, Y. (2021). Design of Force-to-Rebalanced System With Adaptive Fuzzy-PID Controller for N= 3 MEMS Disk Gyroscope. *IEEE Sensors Journal*, 21(12), 13384-13393.

Zirkohi, M. M. (2022). Adaptive backstepping control design for MEMS gyroscope based on function approximation techniques with input saturation and output constraints. *Computers & Electrical Engineering*, 97, 107547.